Hybrid Plasmonic Waveguides: Theory and Applications

by

Muhammad Zulfiker Alam

A thesis submitted in conformity with the requirements
for the degree of Doctor of Philosophy
Graduate Department of Electrical Engineering
University of Toronto

Hybrid Plasmonic Waveguides: Theory and Applications

Muhammad Zulfiker Alam

Doctor of Philosophy

Graduate Department of Electrical Engineering
University of Toronto

2012

Abstract

The study and applications of surface plasmon polaritons (SP) – also known as plasmonics – has attracted the interest of a wide range of researchers in various fields such as biology, physics, and engineering. Unfortunately, the large propagation losses of the SP severely limit the usefulness of plasmonics for many practical applications. In this dissertation a new wave guiding mechanism is proposed in order to address the large propagation losses of the plasmonic guides. Possible applications of this guiding scheme are also investigated.

The proposed hybrid plasmonic waveguide (HPWG) consists of a metal layer separated from a high index slab by a low index spacer. A detailed analysis is carried out to clarify the wave guiding mechanism and it is established that the mode guided by the HPWG results from the coupling of a SP mode and a dielectric waveguide mode.

A two dimensional HPWG is proposed and the effects of various parameters on the HPWG performance are analyzed in detail. This structure offers the possibility of integrating plasmonic devices on a silicon platform.

The proposed waveguide supports two different modes: a hybrid TM mode and a conventional TE mode. The hybrid TM mode is concentrated in the low index layer, whereas the conventional TE mode is concentrated in the high index region. This polarization diversity is used to design a TM- and a TE-pass polarizer and a polarization

independent coupler on a silicon-on-insulator (SOI) platform. Moreover, the performance of a HPWG bend is investigated and is compared with plasmonic waveguide bends. The proposed devices are very compact and outperform previously reported designs.

The application of HPWG for biosensing is also explored. By utilizing the polarization diversity, the HPWG biosensor can overcome some of the limitations of plasmonic sensors. For example, unlike plasmonic sensors, the HPWG biosensor can remove the interfering bulk and surface effects.

Acknowledgements

First and foremost, I want to express my sincere appreciation to my supervisors Prof. Mojahedi and Prof. Aitchison for their support and guidance. They have given me a lot of freedom in pursuing various new ideas and their support was unwavering throughout my research work under their guidance.

I would also like to thank Prof. John Sipe, Prof. Amr Helmy, Prof. Ted Sargent, Prof Henry van Driel and Prof. Li Qian for being on my thesis progress and thesis defence committees and Prof. Pierre Berini for serving as the external member for my thesis defence committee. Their suggestions have greatly improved the quality of the thesis.

Many people have helped me in different ways throughout my PhD work and deserve due appreciation. I would like to thank the current and former members of the Photonics group of the University of Toronto, especially Joachim Maier, Xiao Sun, Jan Niklas Casper, Arnab Dewanjee, Farshid Bahrami and Sean Wagner for their friendship and technical support. I should thank my many other friends, especially Michael Selvanagam, Alex Wong, Francis Elek, Pulin Mondal, Masum Hossain and Mahmud Hasan. In addition to being a true friend, Pulin also deserves gratitude for helping me with the editing of the thesis.

My relatives Yeasmin Begum, Bakul Hossain, Masudur Rahman and Romana Parvin let me feel at home in Toronto. My cousins Tamim, Sakib, Tasnia and Samiha have provided the much needed relief from the complexities of research work.

I was blessed to have a wonderful family and have their constant support throughout my life and especially during the years of my PhD study. My mother Nurjahan Begum and my father Mahbubul Mustafa deserve special acknowledgment for their years of unlimited support, love and understanding. I am also grateful to my two brothers Mazharul Alam and Iftekher Alam for their support.

Finally I would like to express my sincere appreciation for my wife Nusrat Jahan Surovy for being a constant source of inspiration during this journey. She has shown unlimited patience during the stressful time of my thesis writing.

Dedication

To my Parents

Who gave me the strength to complete this journey.

Table of Contents

List of Tables

List of Figures

List of Appendices

Chapter 1

Introduction

Recent progress in nanofabrication technology has enabled researchers to achieve an unprecedented control of material properties. A combination of this progress and the availability of high performance computational facilities has revolutionized many branches of science and technology, notable among them photonics. The ability to control light matter interaction at the scale of a fraction of a wavelength of light has given rise to the area of photonics commonly known as nanophotonics. One very promising branch of nanophotonics is nanoplasmonics which deals with the study and application of surface plasmon (SP).

SP is a surface wave which results from the coupling of an electromagnetic wave with the collective electronic oscillations at a metal-dielectric interface. SP has a number of unique features, and can be of great importance for practical applications. Unlike dielectric waveguides where light confinement is limited by diffraction, plasmonic waveguides can "squeeze" light to a subwavelength scale. This offers the possibility of scaling down photonic devices to the size of transistors which may result in successful integration of photonics and electronics [Zia 2006]. In addition SP-based sensing is already a commercially successful technology [Homola 2006]. Plasmonics can be useful for many other applications: integrated optics [Atwater 2007], nanolithography [Srituravanich 2004], near field scanning microscopy [Kim 2007], cancer diagnosis and treatment [Bardhan 2011] are a few examples.

Though the field of plasmonics holds great promise, and has been called the next big thing in nanotechnology, a number of challenges need to be addressed before these promises are fulfilled. In the optical regime metals have a complex permittivity and as a result SPs suffer from a large propagation loss. This is a major limitation that has prevented plasmonics from becoming a more useful technology. Several ways to mitigate the issue of propagation loss, e.g., use of gain medium or thin metal film have been suggested. However, the loss reduction using these schemes is accompanied by either a significant increase of system complexity or increase of device size. Another problem stems from the lack of maturity of plasmonics as a research area. Though the concept of SP has been known for more than half a century [Rictchie 1957], nanoplasmonics is still in its nascent state. More work is necessary on the design of new types of plasmonic devices before it becomes clear which applications will really benefit from plasmonics.

1.1. Objectives and Contributions

The objectives of this dissertation are two fold: to find some mechanism to address the issue of propagation loss of SP without use of gain medium, and also to design new plasmonic devices which can be useful for practical applications. We accomplished the followings in this work.

1) We proposed a new guiding mechanism that is a combination of dielectric and plasmonic wave guiding. The proposed hybrid plasmonic waveguide (HPWG) provides a better compromise between loss and confinement compared to previously proposed plasmonic waveguides, and has been recognized by the plasmonics research community as one of the most promising plasmonic wave guiding scheme designed to date.

2) We carried out a detailed analysis to clarify the physical nature of the modes supported by the HPWG. The analysis dispels the doubt raised by some researchers about the origin of the modes supported by HPWG and confirms that it is a coupled mode.

3) We proposed a number of HPWG device designs for integrated optical systems. The devices proposed are TM-pass polarizer, TE-pass polarizer, polarization independent directional coupler and waveguide bends. The proposed devices are very compact,

low loss and are fully compatible with silicon on insulator technology. These designs, illustrate that realization of very compact, low loss integrated optic plasmonic devices which outperform existing alternatives – one of the long sought goal of plasmonics is feasible. We have also fabricated and tested the TE-pass polarizer and have confirmed the validity of our simulation results.

4) We proposed a HPWG biosensing scheme and analyzed its performance in detail. The proposed device is more sensitive than plasmonic sensors. Unlike purely plasmonic sensors, the HPWG sensor is also capable of differentiating between change of adlayer thickness and change of bulk index.

1.2. Organization

The organization of the dissertation is as follows. In Chapter 2 we present a brief introduction to plasmonics. We described the general state of plasmonic research, its current applications and potential for future applications. We identify a number of challenges which need to be addressed to fully utilize this potential. We also introduce the HPWG - the central theme of this dissertation.

In chapter 3 we explain the physical mechanism of mode formation in HPWG. To keep the problem analytically solvable we consider only the one dimensional case. We show that the characteristics of the hybrid mode for various waveguide dimensions are consistent with the notion that the hybrid mode is the result of coupling of SP mode and a dielectric waveguide mode.

For practical applications two dimensional HPWGs are more important. Therefore, in Chapter 4 we concentrate on the analysis of such structures. We review previously reported two dimensional HPWG and also present a detailed analysis of the effects of various parameters on hybrid mode characteristics.

In the next two chapters we describe the results of our investigation about the possibility of using the HPWG for optical communication and sensing applications. Unlike previous related works, where the compactness of hybrid mode has been the focus, we attempt to utilize the polarization diversity of the HPWG. In chapter 5 we present designs of compact HPWG devices for silicon on insulator based integrated optic communication systems. The devices we propose are TE- and TM-pass polarizers, polarization independent directional coupler and waveguide bend. We compare these designs with previously reported relevant works and show that the HPWG based devices can outperform previously reported designs. We also highlight the shortcomings of the HPWG and suggest some general guidelines regarding the application of HPWG. In addition to presenting the details of the HPWG based designs, we also presented the results of the first experimental demonstration of HPWG TE-pass polarizer in chapter 4.

In chapter 6 we present the results of our investigation about the possibility of using HPWG for biosensing. We optimize the one dimensional HWPG for single and dual polarization operations and suggest using the polarization diversity to overcome some limitations of plasmonic sensors. We also propose a two dimensional HPWG, which provides functionality similar to the one dimensional HPWG, but is easier to fabricate.

We present a summary of results and contribution in chapter 7. We also provided a number of suggestions for future research directions.

Chapter 2

Fundamentals of Plasmonics

This dissertation focuses on the various possible applications of surface plasmon waves (SP) - a research area commonly known as plasmonics. In this chapter we present a brief review of the present status of plasmonics. SPs belong to a special type of oscillations called polaritons, which result from the coupling of material vibrations with electromagnetic waves. Therefore, we start with a brief description of the polariton. This is followed by a general introduction to various aspects of SP including its dispersion relation, effects of material loss on SP characteristics and commonly used SP excitation schemes. Some of the major applications of SP are discussed next, and the challenges which need to be overcome for further progress of plasmonics are summarized. The review presented here is brief since it serves only to provide background information for placing the research work of this dissertation in the context of current state of the art and knowledge of plasmonics. We end the chapter with a brief introduction to hybrid plasmonic waveguide (HPWG), which is the central theme of this dissertation.

2.1. What is a Polariton and a Surface Plasmon Polariton?

When light interacts strongly with a dielectric medium, often the resulting wave to a good approximation can be considered a coupled mode forming from the interaction of light with the normal modes of the medium. The validity of this physical picture is supported by the presence of an avoided crossing between the light and elementary excitation dispersion lines and existence of a band gap. The term 'polariton' was first used to describe the quantized states of such excitations [Hopfield 1965, Kittel 1993]. As the resonance frequency is approached, the wave number increases and the propagation slows down. Far away from band gap the wave is mostly “Photon like” having mostly light like momentum and wavelength. However, even far away from resonance, much of the energy for such a wave is stored in the polarization induced in the medium as long as the relative permittivity or permeability is significantly different from unity. Therefore, more commonly the term polariton refers to the electromagnetic wave resulting from light-matter interaction over a broad frequency range [Mills 1974] and not the quantum-mechanical entity which results in the sharp absorption lines in dispersive materials as was suggested by Hopfield. In this work we use the word polariton in the broader sense as was done in [Mills 1974].

Since there are different kinds of elementary excitations in solids, there are also different kinds of polaritons. Electromagnetic waves can couple to spin waves in ferromagnetic materials, excitons in semiconductors, phonons in crystals, or electrons in metals - giving rise to magnon polaritons, exciton polaritons, phonon polaritons, and plasmon polaritons respectively. The oscillation may take place over the entire volume of the material or it can be confined only on the surface – resulting in bulk and surface polaritons respectively. In this dissertation we will concentrate on surface plasmon polariton, which results from the coupling of electrons on a metal surface with light.

2.2. Surface Plasmon at Metal-Dielectric Interface

Surface plasmon polariton, commonly known as surface plasmon (SP) is a type of surface wave that can exist at a metal-dielectric interface. Figure 2.1 illustrates the concept of SP. It shows a metal-dielectric interface where the material for $y > 0$ is a lossless dielectric having permittivity ε_1 and the material filling the space for $y < 0$ is a metal having permittivity ε_2. The SP mode supported by such an interface is transverse magnetic TM in nature. The electric field profile and surface charge distribution of SP propagating in the x direction are also shown in Fig. 2.1. Derivation of SP characteristics for a one dimensional structure has been reported in many previous works and will not be repeated here. Instead we will present a very brief summary of SP properties. More details can be found in many excellent review papers and books, for example [Maier 2007].

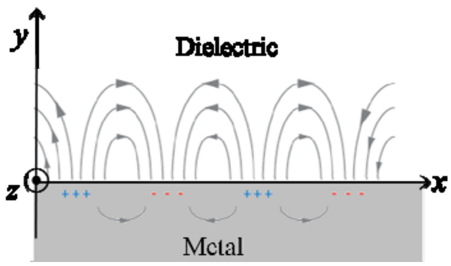

Fig. 2.1. Single metal-dielectric interface and field profile of SP mode.

The expression for the dispersion relation of the SP mode for the metal-dielectric interface shown in Fig. 2.1 is

$$\beta = k_0\sqrt{\frac{\varepsilon_1\varepsilon_2}{\varepsilon_1+\varepsilon_2}} \tag{2.1}$$

Here β is the propagation constant in the *x* direction and the free space wave number is given by $k_0=2\pi/\lambda_0$; λ_0 is wavelength in free space. The permittivity of a lossless metal in the optical regime can be expressed by the Drude model [Maier 2007].

$$\varepsilon_2 = 1-\frac{{\omega_p}^2}{\omega^2} \tag{2.2}$$

Here ω_p is the plasma frequency of the metal and ω is the angular frequency of light. Substituting the expression of (2.2) for ε_2 in (2.1), we get the dispersion relation of SP supported by a lossless Drude metal-dielectric interface.

$$\beta = k_0\sqrt{\frac{\varepsilon_1(1-\frac{\omega_p^2}{\omega^2})}{\varepsilon_1+1-\frac{\omega_p^2}{\omega^2}}} \tag{2.3}$$

Fig. 2.2 shows the dispersion relation described by (2.3). For small ω, β is very close to $k_0\sqrt{\varepsilon_1}$ and the plasmon dispersion curve follows the light line very closely. In this case the SP wave extends deep into the dielectric. As ω approaches the surface plasmon resonance frequency (ω_{SP}), β approaches infinity. ω_{SP} is given by

$$\omega_{SP} = \frac{\omega_p}{\sqrt{1+\varepsilon_1}} \tag{2.4}$$

This condition is known as surface plasmon resonance. Near the surface plasmon resonance frequency, the wave greatly slows down and the extent of the field on either side of the interface becomes vanishingly small.

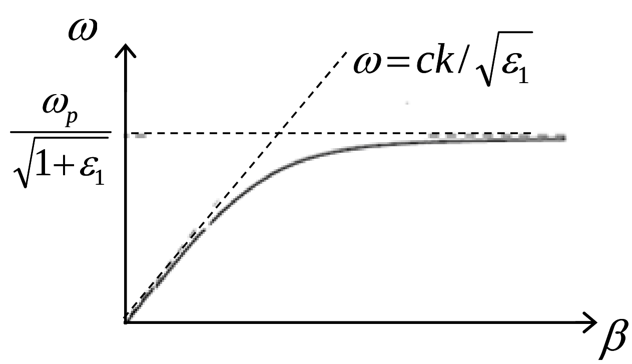

Fig. 2.2. Dispersion relation for surface plasmon between dielectric and Drude metal with no loss.

Real metals have a complex permittivity ($\varepsilon_2 = \varepsilon_2' + i\varepsilon_2''$) and the imaginary part of the permittivity is not negligible. For noble metals like gold and silver at optical frequency regime, however, $\varepsilon_2'' << \varepsilon_2'$. The expression of β in such cases is given by

$$\beta = \beta' + i\beta'' = \frac{\omega}{c}\left(\frac{\varepsilon_1\varepsilon_2'}{\varepsilon_1+\varepsilon_2'}\right) + \frac{\omega}{c}\left(\frac{\varepsilon_1\varepsilon_2'}{\varepsilon_1+\varepsilon_2'}\right)^{3/2}\frac{\varepsilon_2''}{2(\varepsilon_2')^2} \tag{2.5}$$

The propagation distance of the SP is defined as the distance over which the power drops to 1/e of its initial magnitude. It is given by

$$\delta_{SP} = \frac{1}{2\beta''} = \frac{c}{\omega}\left(\frac{\varepsilon_1 + \varepsilon_2''}{\varepsilon_1 \varepsilon_2'}\right)^{3/2} \frac{(\varepsilon_2')^2}{\varepsilon_2''} \tag{2.6}$$

To give an idea about the length scales, the mode size in both metal and dielectric for a silver/air interface is shown in Fig. 2.3. The mode size is defined here as the distance over which the electric field reduces to 1/e of the value at the surface. The permittivity values of silver are taken from a least square curve fitting of [Johnson 1972].

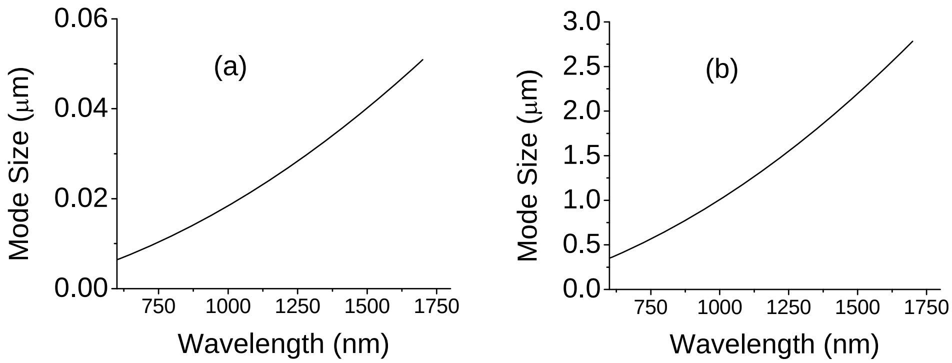

Fig. 2.3. Variation of propagation mode size with wavelength for SP at silver air interface (a) Inside the metal (b) Inside the dielectric.

Fig. 2.4 shows the propagation distance of the SP for a silver-air interface over the wavelength range 600 nm to 1800 nm. For short wavelengths the SP mode is confined closer to the surface and the propagation distance is small. As the wavelength is increased, the SP is less confined and hence the propagation distance is increased. More details of SP length scales can be found in [Barnes 2006].

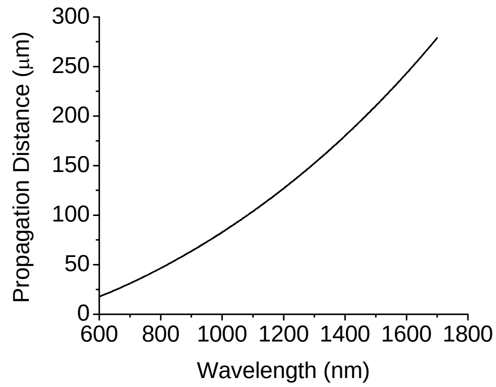

Fig. 2.4. Variation of propagation distance with wavelength for SP at silver air interface.

SP has several attractive features, for example high field intensity at the interface, resonant behavior, ability confine light at nanometer scale dimensions and slow group velocity. Some of these properties can open up the possibility of many useful applications but also can cause a number of challenges. We will review some of these in the next few sections.

2.3. SP Excitation Schemes

SP is a hybrid between light and electronic oscillations. Hence SP can be excited by two ways: excitation by electrons and excitation by light.

2.3.1. Electronic Excitation of SP

When a high energy electron beam hits a metal surface, electrons penetrate the metal and are scattered over a wide range of angles during the process. Some of the scattered electrons may have the correct momentum to excite the SP mode. This excitation method has been used extensively for studying the physics of SP [Raether 1988], [Ritchie 1957]. A more recent work investigated the possibility of implementation of a compact SP source using this phenomenon [Bashevoy 2006]. In this work 50 keV electrons were injected onto a unstructured gold surface to create a localized source of propagating SP. Though this approach may be useful for the study of the physics of SP, using such a SP source for nanophotonics will be challenging. Another very interesting structure was investigated by Takahara et. al [Takahara 2004]. In that structure a luminescent material was sandwiched between two metals and SP was excited directly by applying a voltage between the metal plates. Though electronic excitation of SP is useful for material characterization, for most practical applications optical excitation of SP is preferred.

2.3.2. Optical Excitation of SP

As can be seen from the SP dispersion relation (Fig. 2.2), SP has a larger wave vector than that of light in the same dielectric medium. Hence SP cannot be excited by simply shining a flat metal surface with a plane wave illumination, and there has to be some means for satisfying phase matching condition. The most common methods to excite SP are by prism coupling and grating coupling. These techniques are widely used for generation of SP over a large surface area. There are a number of other techniques available that are used for localized excitation of SP.

Prism coupling is the most popular method of optically exciting SP. Two common methods of SP excitation by prism are shown in Fig. 2.5 [Sambles 1991]. In the Otto configuration shown in Fig. 2.5(a) the prism is placed very near (a few hundred nm) the metal surface. The angle of the incident light is set to be above the critical angle between the prism and air, and as a result light is totally internally reflected from the prism-air interface. The resulting evanescent wave tunnels through the air gap and excites SP on the metal-air interface. This technique is used when it is important to leave the metal surface untouched; study of metal surface for example. In practice it is very difficult to maintain a very small gap between the metal and prism and this technique is seldom used for SP excitation. An easier alternative is the Kretschmann-Raether geometry shown in Fig. 2.5(b). In this configuration the metal is deposited directly on the prism, and the SP is exited at the metal air interface by the evanescent wave resulting from the total internal reflection at the metal-prism interface. This is the most common method of SP generation for practical applications.

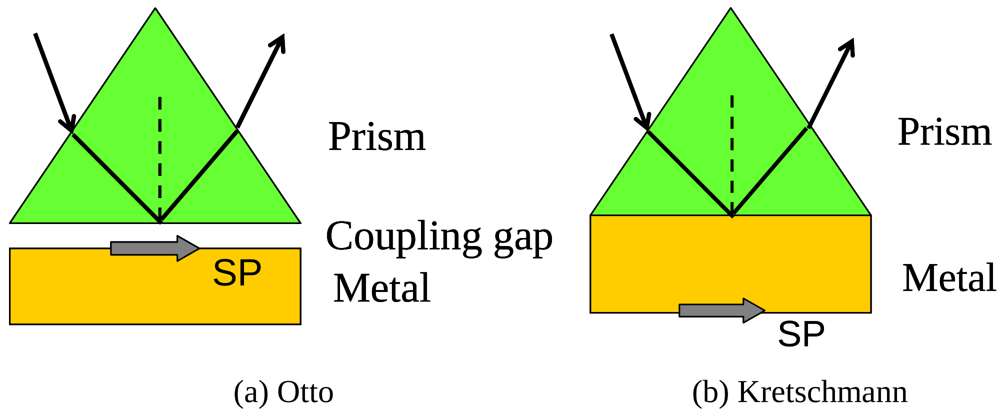

Fig. 2.5. Schematics of different ATR schemes to excite SP (a) Otto (b) Kretschmann.

Gratings can also be used to excite the SP. When light is incident on a grating of period Λ, as shown in Fig. 2.6, it is diffracted away from the surface as a propagating mode and also produces an evanescent field that exits only at the surface. If the light is incident at an angle θ_0, then the evanescent waves will have wave vectors $\omega / c \sin(\theta_0) \pm ng$. Here n is an integer and $g = 2\pi / \Lambda$. If this wave vector matches the SP wave vector along the surface, SP will be excited [Raether 1986].

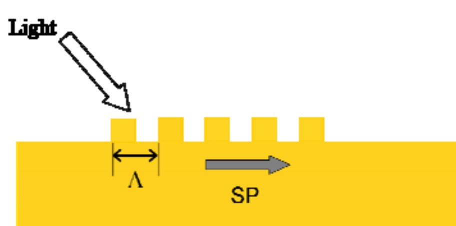

Fig. 2.6. Excitation of SP by grating illumination.

For nano-photonic applications, local excitation of SP is usually preferred. Prism and grating are not suitable means of SP excitation in such cases. Some excitation schemes for local excitation of SP are shown in Fig. 2.7. SP can be excited locally by scattering light from sub-wavelength dimension surface features [Ditlbacher 2002], by tightly focusing a laser beam on a metal surface [Kano 1998] or by backside illumination of metal by small aperture [Tejeira 2007]. The last scheme can prevent noise from the excitation source and has attracted considerable interest for nano-photonic applications in recent years.

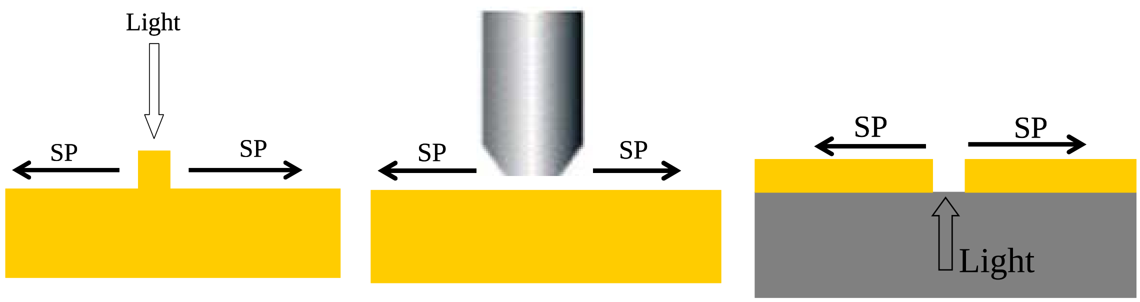

Fig. 2.7. Methods for local excitation of SP (a) Illumination of a surface defect (b) Focusing laser beam tightly on a surface (c) Illumination of nano-hole.

2.4. Applications of SP: Present Status and Future Promises

Plasmonics is one of the most active areas of nanophotonic research and it has been called ‘the next chip enabling technology’ and ‘the next big thing in nanotechnology’ because of its potential to be useful for many applications. Fig. 2.8 shows some areas where SP can be useful. We briefly describe some of the applications to highlight the remarkable diversity of plasmonics.

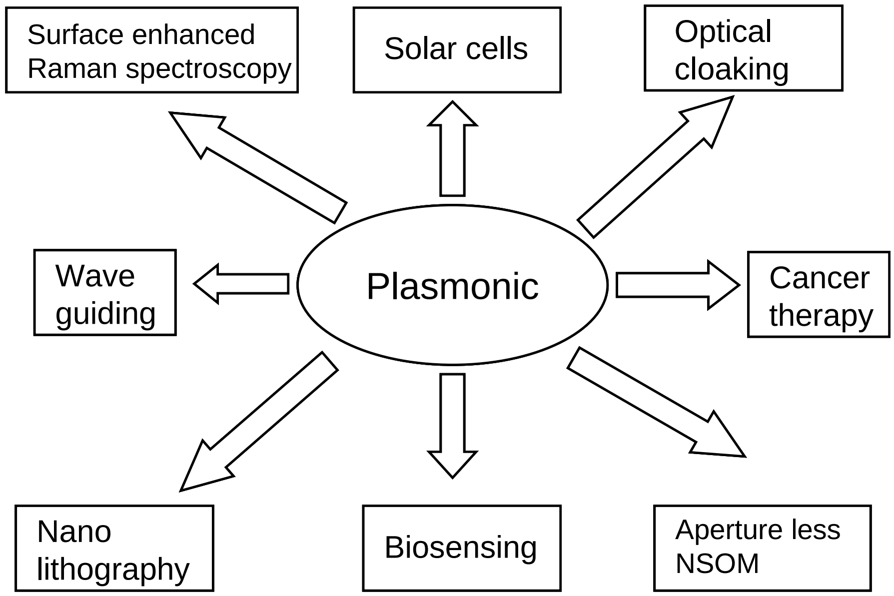

Fig. 2.8. Major areas of applications of plasmonics.

2.4.1. Wave Guiding

In recent years there has been a tremendous increase in demand for bandwidth, and because of their unparalleled data carrying capacity, optical fibers have largely replaced traditional coaxial wires in long haul communication systems. The scenario for bandwidth requirement for short distance communication is also similar. A typical modern microprocessor can contain more than a billion transistors. Traditional electronic interconnects are not capable of meeting the data carrying capacity requirement for such processors and a disruptive solution is necessary to continue increasing the processor performance in future [ITRS 2009]. Replacing the electronic interconnects by optical waveguides can be a solution to this challenge. While the size of electronic devices can be only tens of nanometers, the size of optical waveguides are limited by diffraction and the size mismatch of these two technologies is a major obstacle in their successful integration at chip level. Here we briefly review the origin of diffraction limit and how plasmonic wave guiding offers the possibility of overcoming this limit.

The concept of diffraction limit for waveguides can be conveniently explained by using the concept of a wave number surface [Takahara 2005, Feigenbaum 2007]]. The three constituents of momentum (k_x, k_y and k_z) for a plane wave in a dielectric medium with index n obey the relation

$$k_x^2 + k_y^2 + k_z^2 = n^2 k_0^2 \tag{2.7}$$

Since any optical beam can be decomposed into a combination of plane waves propagating in different directions, the k values in any direction must be within the limit $-nk_0 \le k_j \le nk_0$ (j=x,y,z). The wave number values therefore lie within a sphere of radius nk_0 as shown in Fig. 2.9 (a). The maximum uncertainty in momentum (Δk_{max}) is given by

$$\Delta k_{\max} = 2nk_0 \tag{2.8}$$

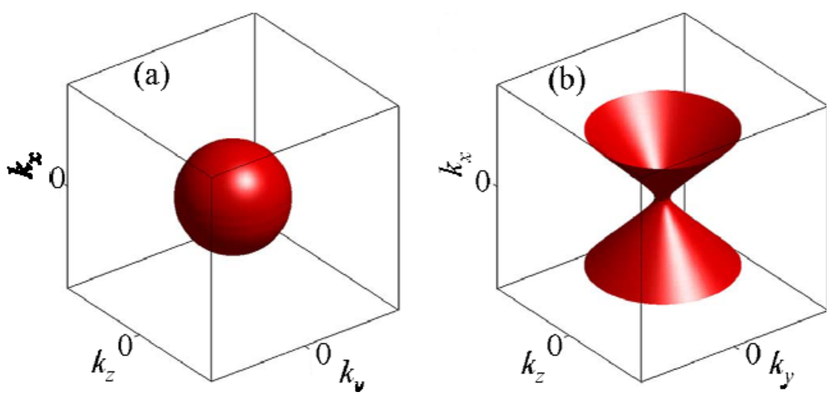

Fig. 2.9. Wave number surfaces in momentum space (a) Optical wave in dielectric (b) Optical wave limited by metal in x direction.

The uncertainty relation in Fourier transform imposes the following relation between uncertainty in momentum and spatial extent (Δk and Δr) [Appendix A].

$$\Delta k \Delta r \ge \pi \tag{2.9}$$

Therefore, Δr must obey the relation

$$\Delta r \geq \pi / \Delta k \qquad (2.10)$$

Δr will be minimized when Δk is maximum (Δk=Δk_{max}). Using the value of Δk_{max} from (2.8) into (2.10) we get the *diffraction limit* in a dielectric cavity or a waveguide.

$$\Delta r_{\min} = \frac{\pi}{\Delta k_{\max}} = \frac{\lambda_0}{4n} \qquad (2.11)$$

If the dielectric claddings in the x direction are replaced by metal, SPs are supported by the metal-dielectric interfaces. Since the SP is a surface wave and decays exponentially away from the surface, the wave numbers along the x direction become imaginary and the relation (2.7) in both metal and dielectric must be modified to

$$k_y^2 + k_z^2 - \left|k_x\right|^2 = nk_0^2 \qquad (2.12)$$

As shown in Fig. 2.9(b), the wave number surface now becomes hyperbolic and the wave vector in the x direction is unbounded. In addition the increase in $\left|k_x\right|$ also increases the momentum in the other directions. Therefore, there is no fundamental limit of the modal volume any more in either the direction parallel or normal to the metal surface. Integrating a subdiffration limited plasmonic waveguide with electronics may lead to new hybrid chips that can take full advantage of both electronics and photonics [Zia 2006].

Unfortunately the sub-diffraction limited guiding of SP is achieved only at the cost of very large propagation loss. For example in metal slot waveguide proposed by Veronis et. al., the mode size is 50 nm but the propagation distance is only 10 micron [Veronis 2005]. In an effort to design a plasmonic guide that will provide a good compromise between propagation loss and confinement, many different geometries have been investigated, some of which are shown in Fig. 2.10. The metal-insulator-metal and metal slot configurations can provide highest level of confinement but the high confinement is accompanied by very large propagation loss [Atwater 2006]. At the other extreme is the insulator-metal-insulator guide, whose propagation loss can be as low as 5 dB/cm but the mode size for this structure is comparable to those of optical fiber modes [Boltaseva 2005, Berini 2009]. Dielectric loaded

SP waveguides use a combination of SP and index guiding [Steinberger 2006]. The structure can be useful for a variety of applications, e.g., electro-optic modulation. However, the mode size is not very small for such a guide. Many other structures, such as channels in metal [Bozhevolnyi 2006], nanohole in metal, metal [Takahara 1997] , wedge [Piles 2005], metal ridge [Pan 2012] have been proposed. Each of these wave guiding schemes have their own advantages and limitations and the choice of plasmonic wave guiding scheme should be guided by the requirements of specific applications.

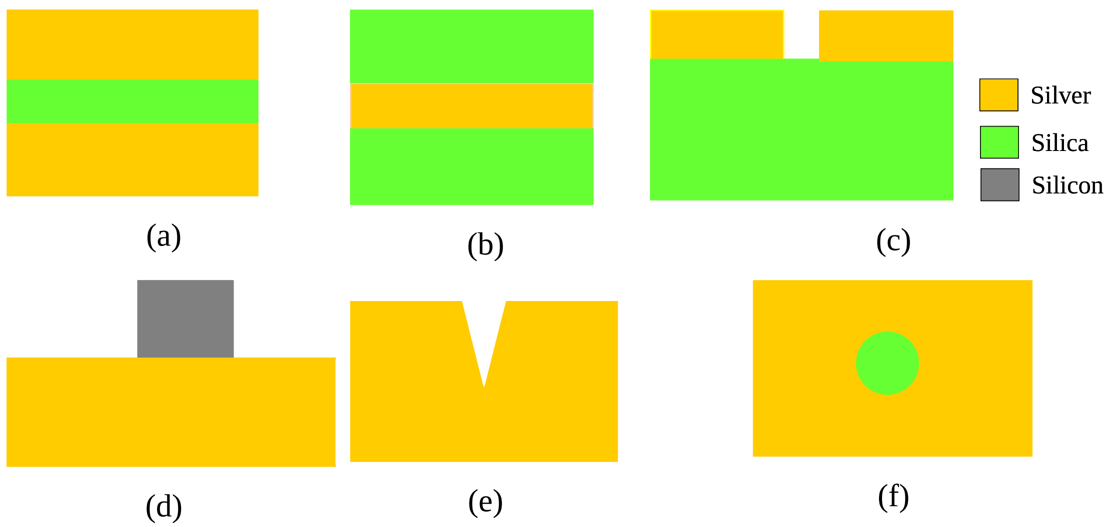

Fig. 2.10. Various types of plasmonic waveguides (a) Metal insulator metal (b) Insulator metal insulator (c) Metal slot (d) Dielectric loaded metal (d) Channel in metal (d) Nanohole in metal.

2.4.2. SP Based Biosensors

Since SP is highly localized to metal surface; its property is significantly affected by any change on the metal surface. This property can be used to implement highly sensitive biosensor. SP sensing schemes based on prism coupling have become one of the most successful optical biosensing schemes proposed to date. SP sensors will be reviewed in chapter 6.

2.4.3. Apertureless Near Field Scanning Optical Microscopy

Near field scanning optical microscopy (NSOM) is a very effective tool for investigating light-matter interaction at nanoscale. Conventional NSOM set up uses a metal coated tapered glass fiber as the tip, and work in either illumination mode or collection mode as shown in Fig. 2.11(a) and (b) respectively. An alternate way is to use a sharp metal tip as shown in Fig. 2.11(c). In this configuration the sample is illuminated from bottom and localized SP is excited on the tip, whose intensity can be 10 to 1000 times that of the incident illumination. When the tip is only few nanometers away, the evanescent field of the tip may convert to propagating mode. This scattered light can be collected by a detector. The resolution achievable by this method can be much higher than that achievable with an aperture NSOM [Kim 2007].

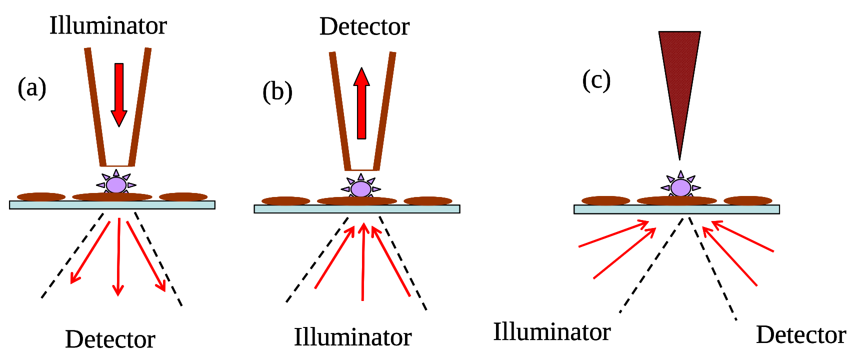

Fig. 2.11. Common operation modes of NSOM (a) Illumination mode (b) Collection mode (c) Apertureless NSOM.

2.5. Challenges Hindering Further Progress of Plasmonics

Though plasmonics shows great promise for many applications, there are a number of issues which need to be addressed before this promise is fulfilled. The biggest limitation of SP is its high propagation loss. A number of different approaches have been proposed to solve this challenge. These are listed below.

a) Use of gain medium: Like any other lossy waveguide mode, an optical gain medium can be used to reduce or eliminate the propagation loss of SP. Since SPs suffer significant propagation loss, the gain medium should provide large enough amplification to realize appreciable propagation [Nezhad 2004]. Our calculations have shown that complete compensation of SP propagation loss is possible with currently available technology [Alam Opt. Exp. 2007], a prediction that has been verified experimentally in recent years [Berini 2010], [Gather 2010]. Although gain assisted SPs have great potential, the requirement to integrate a gain medium and the pumping scheme with a plasmonic waveguide is not always simple, and this approach may not be the best solution for many applications.

b) Cryogenic cooling: The resistance of metal which is the source of SP propagation loss results from the random motion of electrons inside a metal. With a reduction of temperature, the random motion of electron and hence the propagation loss of SP is reduced. Oulton et. al., have demonstrated a SP laser at less than 10 Kelvin [Oulton 2009]. Maintaining very low temperature in a compact and cost effective manner is challenging and this approach for SP loss reduction is not very suitable for mainstream applications.

c) Use of thin metal film: For a very thin metal film (tens of nanometer thickness) the SP mode supported by the two opposite metal-dielectric interfaces can interact and form coupled modes. The even mode resulting from such coupling has most of the power in the surrounding dielectric medium and hence the propagation loss is significantly reduced. This mode, commonly known as long range surface plasmon (LRSP) mode can be useful for a variety of applications including biosensing and implementation of integrated optic devices [Boltaseva 2005, Berini 2009]. However, the mode size of LRSP is comparable to dielectric waveguide modes and is not suitable for nanophotonic applications.

d) Improved plasmonic waveguide design: There is a compromise between loss and confinement for all plasmonic guides. Increase in confinement is always accompanied by increase in propagation loss. However the level of this compromise is not same for all types of plasmonic guides. Many different types of plasmonic guides have been designed to achieve a good compromise between loss and confinement, some of which has been mentioned in section 2.4.1. The research work for this dissertation also followed this approach and proposed a new type of plasmonic waveguide.

In addition to the issue of large propagation loss, another challenge for plasmonics stems from the lack of maturity of plasmonics as a research area. Though plasmonics has a history of more than half a century [Ritchie 1957], the recent interest in plasmonics has been spurred by progress in nanofabrication technology. Although different types of plasmonic devices have been proposed, and some of them show great promise, other devices need to be developed before they can be useful. For example, no suitable, low power electronic SP generation scheme has yet been reported, and unless this is done, plasmonic waveguides cannot be successfully used as optical interconnects. More work is necessary to develop a design suite so that one can exploit the benefit of plasmonics to the fullest extent.

2.6. Hybrid Plasmonic Waveguide: A Combination of Dielectric and Plasmonic Wave Guiding

As a solution to the issue of propagation loss of SP, we have proposed a new waveguide, which we designate as a hybrid plasmonic waveguide (HPWG). Fig. 2.12(a) shows the cross section of a two dimensional HPWG. It consists of a high index region (silicon) separated from a silver surface by a low index spacer (silica). The close vicinity of the silver-silica interface and the silicon slab results in coupling of the SP mode and dielectric waveguide mode supported by these two structures. Fig. 2.12(b) shows the resulting hybrid mode. The guide also supports a conventional TE mode which is shown in Fig. 2.12(c). The mode sizes for both TE and TM modes are comparable in this case and are very similar to mode size achievable in case of silicon waveguide. For a thinner spacer layer the mode size for the TM mode is significantly smaller. For example, as shown in Fig. 2.12 (d), almost all power is confined in a 45 nm spacer layer of a HPWG. TE mode is not supported by the HPWG in this case.

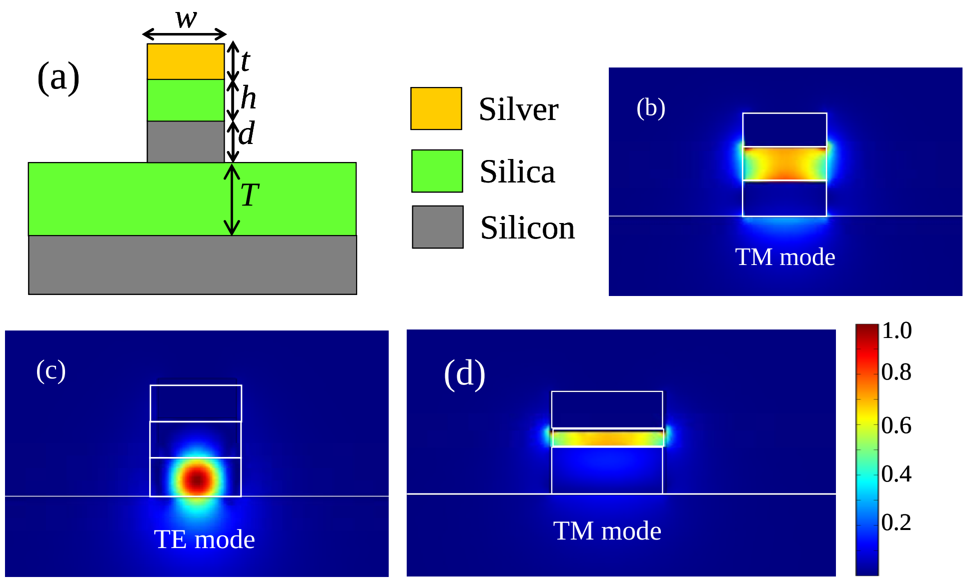

Fig. 2.12. (a) Schematic of the hybrid waveguide. (b) and (c) Power density profile for the TM and TE modes respectively for waveguide dimensions are w = 350 nm, t = 200 nm, h = 150 nm, d = 150 nm and T = 2 µm. (d) Power density profile for the TM mode for w = 350 nm, t = 200 nm, h = 150 nm, d = 45 nm and T = 2 µm. Wavelength of light is 1550 nm.

HPWG offers a number of advantages: it offers a better compromise between loss and confinement compared to purely plasmonic waveguides, and is compatible with silicon on insulator technology. Since power for the TE and TM modes in such a guide are concentrated in two different layers, their properties can be controlled in different manners by changing the material properties and waveguide dimensions of the layers- a property that can be used to design new kind of photonic components. Because of these attractive features the proposed guide has attracted a lot of interest in recent years. Many different variations of HPWG have been investigated by different groups, and many different applications have been suggested.

Our work has played a key role in the progress of HPWG research. In addition to being the first group proposing the concept of hybrid plasmonic wave guiding, we have also carried out detailed analysis to clarify the physical picture of mode formation in HPWG. We have also proposed a number of HPWG devices for integrated optic communication and biosensing applications. The rest of this dissertation will describe our work on various aspects of the theory and applications of HPWG.

Chapter 3

Theoretical Analysis of Hybrid Plasmonic Waveguides

The advantages and limitations of plasmonic and dielectric waveguides are in some ways complementary. Dielectric waveguides can be practically lossless but the mode size in such guides is limited by diffraction. Plasmonic guides on the other hand, can squeeze light far below diffraction limit but at the cost of large propagation loss. An interesting question to ask is: what happens if one attempts to combine both guiding mechanisms? The answer is the hybrid plasmonic waveguide (HPWG), which will be the topic of investigation in this dissertation. This chapter serves as an introduction to HPWG and explores the physical mechanism behind the formation of hybrid mode. The rest of the chapter is organized as follows. In section 3.1 we introduce the HPWG and with an example illustrate the fact that it can provide a better compromise between loss and confinement compared to purely plasmonic guide. The methods of analysis followed in this chapter are also discussed. In section 3.2 we investigate the variations of effective mode indices and field profiles for the guided modes with variations of waveguide dimensions. To keep the problem analytically solvable we consider only one dimensional structure. In section 3.3 we summarize the modal characteristics and show that these characteristics can be explained from the assumption that the modes supported by the HPWG result from the coupling of the SP and dielectric waveguide modes. Section 3.4 concludes the chapter with some remarks.

3.1. Description of Structure and Method of Analysis

As has been explained in the previous chapter, a metal-dielectric interface, for example the silver-silica interface shown in Fig. 3.1(a) can support a SP mode. A silicon slab surrounded by silica also shown in Fig. 3.1(a) can support a dielectric waveguide mode. When the two guides are brought close to each other, the SP mode supported by Guide 1 couples with the TM type dielectric waveguide mode supported by Guide 2, and forms a hybrid mode. As shown in Fig. 3.1(b), power for the hybrid mode is highly confined in the low index medium between the metal and the dielectric slab (an area which is designated as *spacer* throughout this work). Since the SP mode is TM in nature, the hybrid mode is also a TM mode. We consider only the TM modes in this chapter.

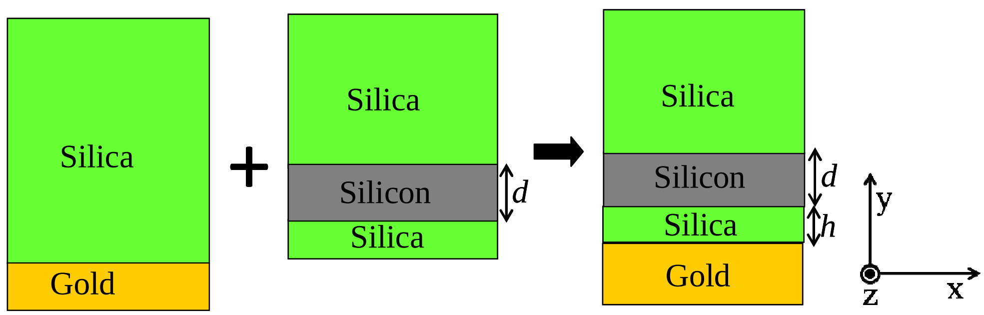

(a)

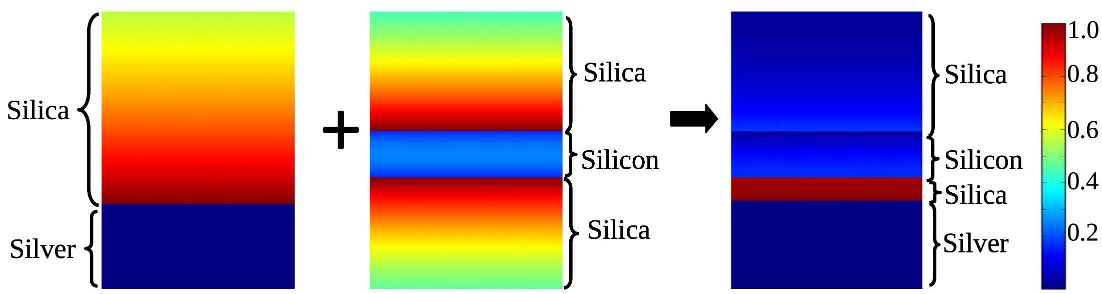

(b)

Fig. 3.1. Formation of hybrid mode from coupling of dielectric and SP mode (a) Waveguide structure (b) Normalized power density. The coordinate system used is also shown. The xz plane coincides with the gold-silica interface for the HPWG. The dimensions are h=50 nm, d=100 nm. Wavelength of operation is 1.55 μm.

Fig. 3.2 shows the guided power density profile of the hybrid mode. For comparison, guided power density for a single metal-dielectric interface SP mode is also plotted. Similar to HPWG, the metal is silver in this case and the permittivity of the dielectric medium is chosen to be 7.1 to make the propagation loss of the SP mode same as that of the hybrid mode. The hybrid mode is much better confined than the SP mode and hence the HPWG can provide a better compromise between loss and confinement than pure plasmonic mode. This is the key motivation behind our exploration of the usefulness of HPWG for various applications - results of which will be presented in later chapters. In this chapter we will concentrate on the physics of the hybrid mode formation and hybrid mode characteristics under various conditions.

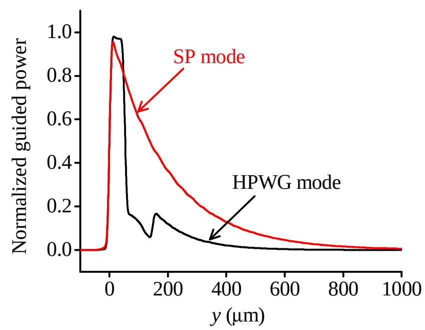

Fig. 3.2. Comparison of guided power density profile for the SP mode and the hybrid mode for the same propagation loss. The dimensions of the HPWG are are h = 50 nm, d = 100 nm. Wavelength of operation is 1.55 µm.

The modes supported by the one dimensional HPWG structure shown in Fig. 3.1 can be analyzed by using transfer matrix method. The method works by constructing the transfer matrix from enforcing boundary conditions between the adjacent layers as explained in detail in [Breukelaar 2004]. Assuming propagation in the z-direction, the expressions for the magnetic field and electric fields for the intermediate layer j (j = 1, 2) can be written as

$$\vec{\mathrm{H}}_j = \hat{x} H_{xj}(y) \exp[i(\gamma z - \omega t)] \tag{3.1}$$

$$\vec{E}_j = [\hat{y} E_{yj}(y) + \hat{z} E_{zj}(y)] \exp[i(\gamma z - \omega t)] \tag{3.2}$$

Here $\gamma = k_0(N_{eff} + iK_{eff})$ is the complex propagation constant, $k_0 = (2\pi)/\lambda_0$ is the free space wave number, λ_0 is the free space wavelength, N_{eff} and K_{eff} are the normalized phase and attenuation constants. The electric and magnetic fields are related by Maxwell's curl equations.

$$\nabla \times \vec{E} = i\omega\mu_0 \vec{H} \quad (3.3)$$

$$\nabla \times \vec{H} = -i\omega\varepsilon_0\varepsilon_r \vec{E} \quad (3.4)$$

Inserting expressions (3.1) and (3.2) into (3.3) and (3.4), the following equation can be derived for magnetic field in the intermediate layers.

$$\frac{d^2 H_{xj}(y)}{dy^2} + k_j H_{xj}(y) = 0 \quad (3.5)$$

Here k_j s are the transverse wave numbers for layer j (j=1,2) and are given by $k_1 = \sqrt{\varepsilon_{Silica} k_0^2 - \gamma^2}$ and $k_2 = \sqrt{\varepsilon_{Silicon} k_0^2 - \gamma^2}$; ε_{Silica} and $\varepsilon_{Silicon}$ are permittivity of silica and silicon respectively. The corresponding electric field components are

$$E_{zj}(y) = -\frac{i}{\omega\varepsilon_0\varepsilon_{rj}} \frac{dH_{xj}(y)}{dy} \quad (3.6)$$

$$E_{yj}(y) = -\frac{\gamma}{\omega\varepsilon_0\varepsilon_{rj}} H_{xj}(y) \quad (3.7)$$

Here $\varepsilon_{r1} = \varepsilon_{Silica}$ and $\varepsilon_{r2} = \varepsilon_{Silicon}$. For a bound TM mode propagating in the z direction, the magnetic field in the substrate (H_{xs}(y)) and cladding (H_{xc}(y)) are exponentially decaying and hence can be written as

$$H_{xs}(y) = A_s e^{k_s y} \qquad y<0 \tag{3.8}$$

$$H_{xc}(y) = A_c e^{-k_c(y-(h+d))} \quad \text{for } y>h+d \tag{3.9}$$

Here k_s and k_c are transverse wave numbers in substrate (silver) and cladding (silica) and are given by $k_s = \sqrt{\gamma^2 - \varepsilon_{Ag} k_0^2}$ and $k_c = \sqrt{\gamma^2 - \varepsilon_{Silica} k_0^2}$. A_s and A_c are constants and only one of them is independent. A_s and A_c can be shown to be related by [Breukelaar 2004].

$$\begin{bmatrix} A_s \\ \dfrac{A_s k_s}{\varepsilon_{Ag}} \end{bmatrix} = \begin{bmatrix} m_{11} & m_{12} \\ m_{21} & m_{22} \end{bmatrix} \begin{bmatrix} A_c \\ -\dfrac{A_c k_c}{\varepsilon_{Silica}} \end{bmatrix} \tag{3.10}$$

where

$$\begin{bmatrix} m_{11} & m_{12} \\ m_{21} & m_{22} \end{bmatrix} = \begin{bmatrix} \cos(k_1 h) & -\dfrac{\varepsilon_{Silica}}{k_1}\sin(k_1 h) \\ \dfrac{k_1}{\varepsilon_{Silica}}\sin(k_1 h) & \cos(k_1 h) \end{bmatrix} \begin{bmatrix} \cos(k_2 d) & -\dfrac{\varepsilon_{Si}}{k_2}\sin(k_2 d) \\ \dfrac{k_2}{\varepsilon_{Si}}\sin(k_2 d) & \cos(k_2 d) \end{bmatrix} \tag{3.11}$$

Eliminating A_s and A_c from (3.10) the dispersion relation for the multilayer structure can be obtained.

$$\frac{k_s}{\varepsilon_{Ag}} m_{11} + \frac{k_c}{\varepsilon_{Silica}} m_{22} - m_{21} - \frac{k_s k_c}{\varepsilon_{Ag}\varepsilon_{Silica}} m_{12} = 0 \tag{3.12}$$

Solutions of (3.12) provide accurate information about the guided modes for any combinations of waveguide dimensions and material properties. However, *getting a physical picture* of the mode formation from this approach is not straight forward.

An alternate, approximate approach that can provide a better insight is based on the concept of coupled modes. As explained at the beginning of this section, the HPWG can be thought of a combination of two waveguides. However, results obtained from the *conventional* Coupled Mode Theory (CMT) are valid only for weakly coupled structures [Hardy 1985]. On the other hand, non-orthogonal CMT can provide satisfactory results in the case of strong coupling but only for low index contrast guides [Snyder 1987]. In the case of HPWG, Guide

2 (Fig. 3.1(a)) is a high index contrast waveguide, and because of the small spacer thickness the coupling is very strong. Therefore, straight forward application of CMT or non-orthogonal CMT may not provide accurate information about the mode characteristics of the HPWG [Cooper 2009]. However, this does not mean that the coupled mode as a concept is incorrect or coupled modes are not formed in the structure shown in Fig. 3.1(a). As long as the difference in *effective indices* of the modes supported by the Guide 1 and 2 is small and the guides are in close vicinity, coupled modes will be formed. In this work we use the dispersion relation [Eq. (3.12)] to *find the exact solutions* for the guided modes but rely on the concept of coupling among the modes to provide a physical picture of the modes formation. We examine the properties of the modes supported by the hybrid structure for various silicon and spacer layer thicknesses at 1.55 μm wavelength. The permittivity of silica, silver, and silicon are taken from [Palik 1985], [Johnson 1972], and [Palik 1985], respectively. Equation (3.12) is solved by simplex search algorithm to find the allowed modes. The method is simple and does not require the computation of numerical or analytical gradients; however, it can find only local solutions. To ensure that we are indeed calculating the effective mode indices properly, we compared the values obtained by solving equation (3.12) with those obtained from the finite element code, Comsol Multiphysics. The effective indices predicted by the two methods matched well and the difference was less than 0.05% in the worst case.

3.2. Properties of the Modes Supported by the Hybrid Plasmonic Guide

In case of coupling between two identical waveguides, one of the coupled modes exhibits even symmetry and the other one exhibits odd symmetry with respect to the midpoint of the gap region (spacer) separating the two guides. In case of coupling between two dissimilar waveguides (the case discussed in this work), the coupled modes lack complete symmetry but as shown later in this section, one of the modes is still “quasi- even” (does not become zero anywhere in the spacer region) and the other mode is “quasi-odd” (becomes zero somewhere in the spacer region).

Behavior of the modes supported by the HPWG shown in Fig. 3.1(a) depends strongly on the properties of the modes supported by Guides 1 and 2. Therefore, a short discussion and classification of the modes supported by Guide 1 and 2 are needed before we proceed further. Guide 1 supports only one mode: SP at the silver-silica interface, while the number of modes supported by Guide 2 and their behavior depend on silicon thickness (d). For d<250 nm, Guide 2 supports only TM_0 mode. We use the following notations.

Table 3.1. Notations used in this work and their meanings

Symbol	**Meaning**
N_{SP}^{G1}	Real part of effective mode index of the SP mode supported by Guide 1
N_{TM0}^{G2}	Real part of effective mode index of the TM_0 mode supported by Guide 2
N_{TM1}^{G2}	Real part of effective mode index of the TM_1 mode supported by Guide 2
N_{Even}^{HG}	Real part of the effective index of the quasi-even supported by the hybrid guide
N_{Odd}^{HG}	Real part of the effective index of the quasi-odd supported by the hybrid guide
$\Delta_0 = N_{TM0}^{G2} - N_{SP}^{G1}$	Difference of real part of effective mode indices of SP mode supported by Guide 1 and TM_0 mode supported by Guide 2
$\Delta_1 = N_{TM1}^{G2} - N_{SP}^{G1}$	Difference of real part of effective mode indices of SP mode supported by Guide 1 and TM_1 mode supported by Guide 2
D_{TM1}^{Cut}	Cut-off thickness of TM_1 mode supported by Guide 2

Depending on the silicon thickness, a number of different situations are possible, which are summarized in Table 3.2. We have excluded the cases $N_{SP}^{G1} >> N_{TM0}^{G2}$ and higher order modes supported by Guide 2 from consideration in this work because the case $N_{SP}^{G1} >> N_{TM0}^{G2}$ does not occur for any silicon thickness and, careful examination of the cases in Table 3.2 is sufficient to predict the higher order mode's field profile.

Table 3.2. Various conditions investigated in this work

Case #	Condition	Silicon thickness (*d*)	Difference between effective mode indices
1	$N_{SP}^{G1} > N_{TM0}^{G2}$, Small Δ_0, $d << d_{TM1}^{Cut}$	45 nm	Δ_0= - 0.0026
2	$N_{SP}^{G1} = N_{TM0}^{G2}$, Small Δ_0, $d << d_{TM1}^{Cut}$	50.8 nm	$\Delta_0 \approx 0$
3	$N_{SP}^{G1} < N_{TM0}^{G2}$, Small Δ_0, $d << d_{TM1}^{Cut}$	100 nm	Δ_0= 0.0426
4	$N_{SP}^{G1} < N_{TM0}^{G2}$, Large Δ_0, $d << d_{TM1}^{Cut}$	130 nm	Δ_0= 0.1
5	$N_{SP}^{G1} < N_{TM0}^{G2}$, Large Δ_0, $d \approx< d_{TM1}^{Cut}$	240 nm	Δ_0= 0.764
6	$N_{SP}^{G1} < N_{TM1}^{G2}$, Small Δ_1, Large Δ_0, $d > d_{TM1}^{Cut}$	340 nm	Δ_0= 1.346 Δ_1= 0.0344

In the following we investigate the behavior of the hybrid waveguide modes with varying silicon and spacer thicknesses {subject to the constraints enumerated in Table 3.2}. In some of the cases in addition to the hybrid mode, dielectric waveguide modes supported by the silicon slab also independently exists. For example in case 6 (*d*=340 nm), in addition to the modes whose field profiles are combinations of modes supported by Guide 1 and Guide 2, a mode also exists which is almost identical to the TM_0 mode supported by Guide 2. These dielectric waveguide modes are well studied and well understood, and hence will not be investigated in this work.

3.2.1. Variations of the Effective Mode Index

Figures 3.3(a), 3.3(b) and 3.3(c) show the variations of N_{Even}^{HG} with varying spacer thickness (*h*) for the cases of Table 3.2. Variations of N_{Odd}^{HG} for various cases are plotted in Fig. 3.3(d).

Variation of N^{HG}_{Even} and N^{HG}_{Odd} for case 1 and 2 are very similar and to avoid redundancy, case 2 is omitted in these plots. From Fig. 3.3 it is clear that quasi-even mode exists for any *h* but quasi-odd mode is cut-off for small *h*. For cases 1 and 2 ($N^{G1}_{SP} \geq N^{G2}_{TM0}$), for increasing spacer thickness (*h*), N^{HG}_{Even} approaches N^{G1}_{SP} and N^{HG}_{Odd} approaches N^{G2}_{TM0}. On the other hand, for cases 3 and 4, for increasing spacer thickness (*h*), N^{HG}_{Even} approaches N^{G2}_{TM0} and N^{HG}_{Odd} approaches N^{G1}_{SP}, a trend opposite to cases 1 and 2. For the case 5 (*d* = 240 nm) hybrid mode characteristics are significantly different from the other cases in Table 3.2. In this case the guide does not support quasi-odd mode for any spacer thickness, and as shown in Fig. 3.3(c) , the variation of N^{HG}_{Even} is opposite of that of quasi-even mode in other cases i.e., with increasing *h*, N^{HG}_{Even} increases instead of decreasing. For the case 6 (*d* = 340 nm) Guide 2 is multimode. In this case N^{HG}_{Even} approaches N^{G2}_{TM1} and N^{HG}_{Odd} approaches N^{G1}_{SP}. It is interesting to note that variations of the effective indices for case 3 (*d* = 100 nm) and case 6 (*d* = 340 nm) are very similar. The reason for this is explained in section 3.3.

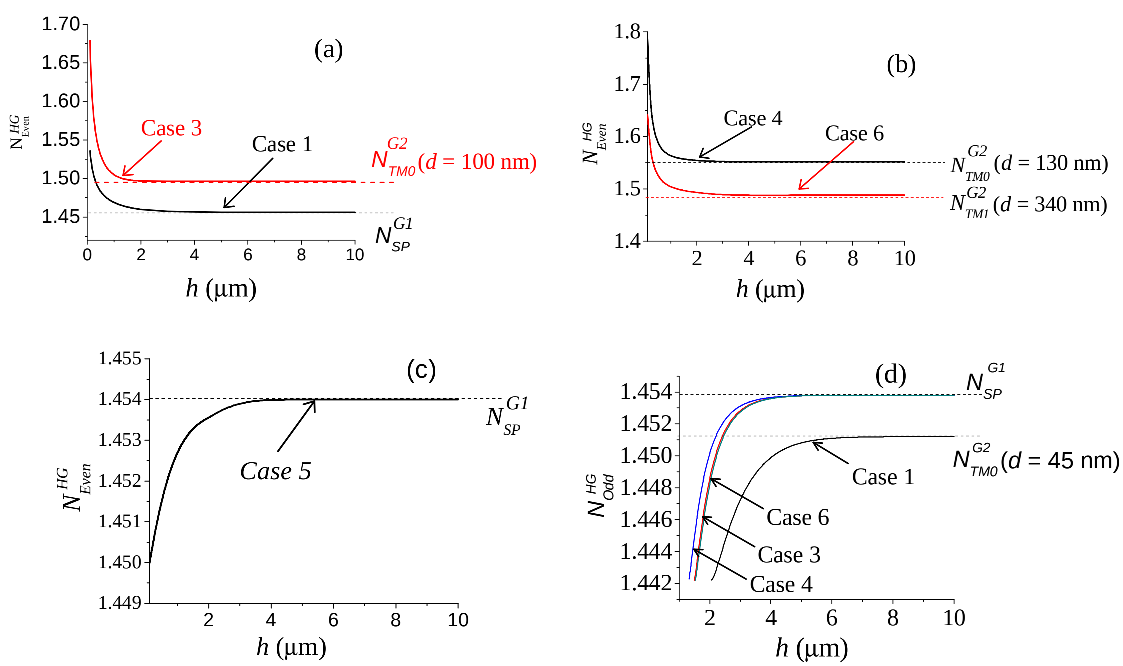

Fig. 3.3. Variations of effective mode indices for the guided modes as a function of *h* (spacer height) for various *d* (silicon thickness). (a), (b) and (c) are for quasi-even and (d) is for quasi-odd.

3.2.2. Evolution of the Mode Profiles as a Function of Spacer Thickness

In this subsection we examine the effects of varying the spacer thickness (h), for a fixed silicon thickness (d), on the field profiles for the cases considered in Table 2. We plot the real part of the transverse magnetic field (H_x). To properly designate the nature of the hybrid mode we use the following notations. If the hybrid mode is formed from the coupling of SP mode supported by the Guide 1 and TM_0 mode supported by the Guide 2, and if with increasing the spacer thickness (h) the mode converts to a SP mode supported by the Guide 1, we designate it as SP-TM_0. If on the other hand, the mode converts to a TM_0 mode supported by the Guide 2, we designate it as TM_0-SP. A similar nomenclature is used for other cases (e.g. SP-TM_1 or TM_1- SP).

Figures 3.4(a) through 3.4(c) show evolution of quasi-even and quasi-odd modes for varying spacer thickness (h) for the case 1of Table 3.2 (d = 45 nm). Here y=0 is the position of the silver/silica interface. To show the mode profiles clearly for both small and large h, we have plotted the mode profiles of quasi-even mode in two different figures, i.e. Figs. 3.4(a) and 3.4(b). As it can be seen from these figures, quasi-even mode is of the type SP-TM_0 and quasi-odd mode is of the type TM_0-SP. For the case 2 of the Table 3.2 (h = 50.8 nm), the mode profiles and their evolution with varying spacer thickness are very similar to those of the case 1 and are not discussed here. To keep the discussion brief, we will plot the field profiles only for the quasi-even mode for the rest of the cases and summarize the properties of both quasi-even and quasi-odd modes at the end of this subsection.

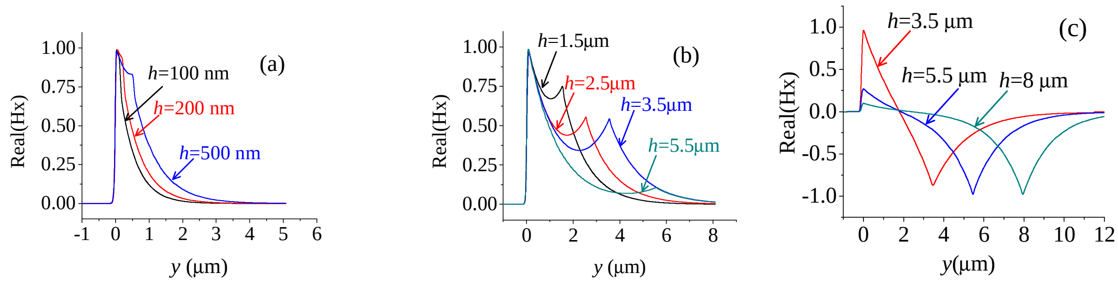

Fig. 3.4. (a) and (b) Real part of the normalized magnetic field for the quasi-even mode. (c) Real part of the normalized magnetic field for the quasi-odd mode. In all figures *h* is the spacer thickness and silicon thickness (*d*) is 45 nm. (Case 1 of Table 3.2)

Increasing silicon film thickness changes the nature of the mode. For the case 3 in Table 3.2 (d = 100 nm) in contrast to cases 1 and 2, the quasi-even mode is of the type TM_0-SP as shown in Fig. 3.5. The quasi-odd mode is of the type SP-TM_0 (not shown in the figure).

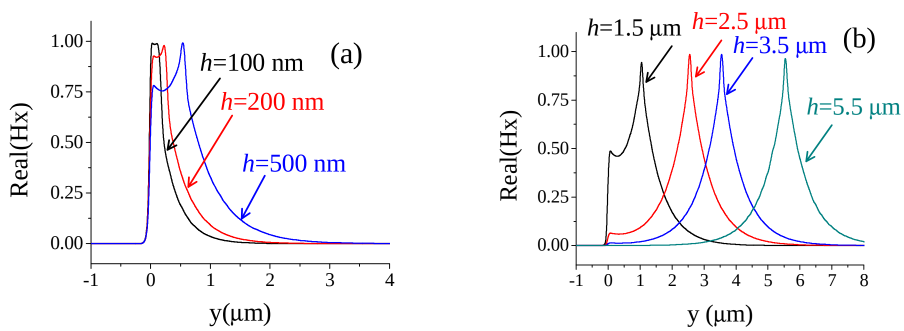

Fig. 3.5. Real part of the normalized magnetic field for the quasi-even mode for varying spacer thicknesses (*h*). Silicon thickness (*d*) is 100 nm. (Case 3 of Table 3.2).

A further increase in the silicon film thickness (d) makes Δ_0 larger and the mode begins to lose its hybrid nature. As an example, Fig. 3.6 shows the mode profiles for the case 4 of the Table 3.2 (d = 130 nm). The quasi-even mode in this case is concentrated in the silicon slab and is similar to the TM_0 mode supported by Guide 2 and with increasing spacer thickness it very quickly converts to TM_0 mode supported by Guide 2. For larger silicon thickness (greater than case 4 but smaller than case 5) the coupling becomes less significant i.e., the quasi-even mode and quasi-odd modes very closely resembles TM_0 mode of Guide 2 and SP mode of Guide 1 respectively.

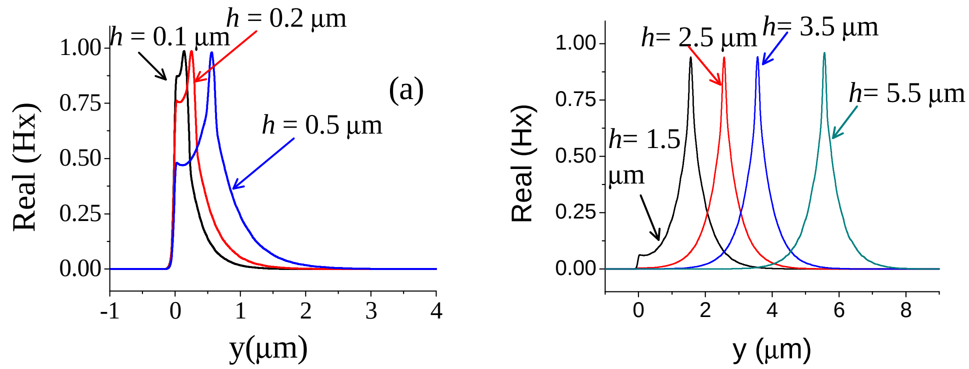

Fig. 3.6. Real part of the normalized magnetic field for the quasi-even mode for varying spacer thicknesses (*h*). Silicon thickness (*d*) is 130 nm. (Case 4 of Table 3.2).

For an even larger silicon thickness e.g., case 5 of Table 3.2 (*d* = 240 nm), the silicon slab supports a TM_0 mode which is weakly affected by presence of the metal and does not couple with the SP mode. However, a new mode appears in this case. As seen from the field profiles of Fig. 6 this is a quasi-even mode and although the silicon thickness is not large enough to support a TM_1 mode when surrounded by silica on both sides, the hybrid mode is still the result of coupling between SP and TM_1 mode. The mode is of type SP-TM_1 i.e., it converts to SP mode for larger spacer thickness. Quasi-odd mode is not supported in this case for any spacer thickness.

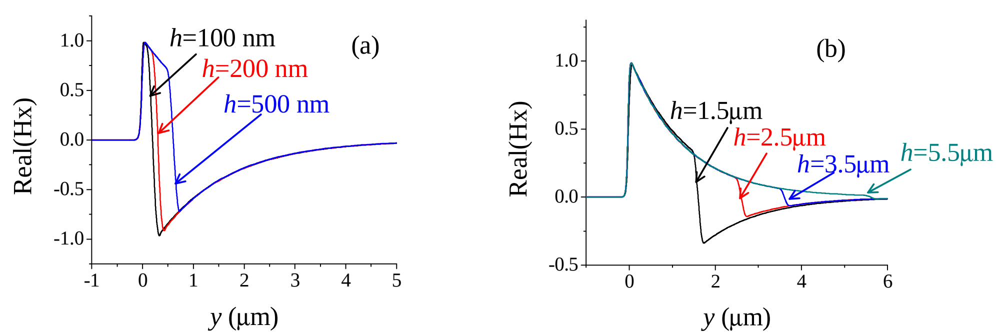

Fig. 3.7. Real part of the normalized magnetic field for the quasi-even mode for varying spacer thicknesses (*h*). Silicon thickness (*d*) is 240 nm. (Case 5 of Table 2).

With further increase in the silicon thickness (e.g. case 6 in Table 3.2, *d* = 340 nm), Guide 2 becomes multimode and supports both TM_0 and TM_1 modes. Similar to the case 5, SP couples with the TM_1 mode and the resulting quasi-even mode is of the type TM_1-SP, as shown in Fig. 7. It should be pointed out that although the field profiles in Fig. 6 and 7 may seem to resemble quasi-odd modes, the magnetic field (H_x) in fact does not cross zero in the spacer but inside the silicon film. The modes shown in Fig. 6 and 7 therefore are quasi-even modes and not quasi-odd. For case 6, the quasi-odd modes of the type SP-TM_1 is also present for large spacer thickness, which are not shown in the figure.

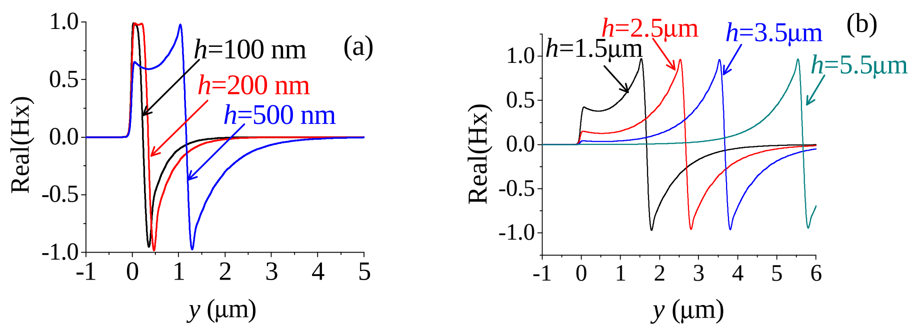

Fig. 3.8. Real part of the normalized magnetic field for the quasi-even mode for varying spacer thicknesses (*h*). Silicon thickness (*d*) is 340 nm. (Case 6 of Table 3.2).

Table 3.3 summarizes the mode types for the various cases mentioned in Table 3.2.

Table 3.3: Summary of the modal characteristics for the cases of Table 3.2

Case #	Nature of quasi-even mode	Nature of the quasi-odd mode
1	SP-TM_0	TM_0-SP
2	SP-TM_0	TM_0-SP
3	TM_0-SP	SP-TM_0
4	TM_0-SP	SP-TM_0
5	SP – TM_1	Does not exist
6	TM_1-SP	SP-TM_1

3.3. Summary and Analysis of the Hybrid Plasmonic Waveguide Modes

There are several general trends related to the mode formations in the HPWG which can be arrived at from our discussion in Section 3.2. In the following we will list these trends and provide some physical explanations underlying the observed behaviors.

a) The quasi-even mode of the HPWG waveguide exists for any spacer thickness (*h*), but the quasi-odd mode is cut-off for small spacer thickness.

   The presence of only one mode in the hybrid guide for small spacer thickness has led some researchers to question the validity of the mode hybridization concept in these waveguides [Avrustsky 2010]. However, it must be pointed out that some assumptions of the conventional CMT such as the weakly coupling condition and orthogonality of the guided modes are not necessary valid for the HPWG in which the separation between the constituent waveguides (Guides 1, and 2) is extremely small. In fact, *non-orthogonal* CMT formulation predicts that the odd modes reach the cut-off condition for small waveguides separation [Hardy 1985], which is illustrated in the case for the hybrid waveguides examined here and in Refs. [Alam 2007, Oulton 2008, Fujii 2009].

b) For increasing spacer thickness the hybrid modes convert to the modes guided by the constituent waveguides (Guides 1 and 2). The quasi-even mode always converts to the mode of Guide 1 or 2, whichever has a higher effective mode index. The quasi-odd mode on the other hand, will convert to the mode of Guide 1 or 2, whichever has a lower effective mode index.

   This behavior is expected when coupling takes place between two nonidentical waveguides as has been explained in more detail in [Haus 1991].

c) If Guide 2 supports multiple modes, SP mode supported by the Guide 1 couples to the dielectric waveguide mode supported by the Guide 2 whose effective index is closest to its own effective index.

This is consistent with the concept of coupled mode formation: only modes with comparable effective indices are expected to couple and form hybrid modes.

d) Hybrid mode of type SP–TM_1 exists even when $d < D_{TM1}^{Cut}$ provided that $\left| d - D_{TM1}^{Cut} \right|$ is small. Quasi-odd mode is absent in this case {case 5 of Table 3.2}.

The situation is very similar to the asymmetrical nano-scale plasmonic waveguide reported in [Berkovich 2008]. As shown in [Berkovich 2008], if a plasmonic (metallic) slot waveguide is placed on a dielectric substrate, the metal blocks the radiation away from the slot waveguide and the cut-off width of the guide is reduced. A similar explanation also holds for the case 5 {of Table 3.2}. The presence of the metal near the high index slab in a hybrid waveguide acts as a strong reflector and cut-off thickness of the TM_1 mode is reduced. Hence, a hybrid mode of the type SP-TM_1 is formed even when the silicon slab is below the cut-off thickness of the TM_1 mode ($d < D_{TM1}^{Cut}$). For large spacer thickness (*h*), the effect of reflection from the metal surface is less pronounced and the silicon slab fails to support the TM_1 mode. Hence, quasi-odd mode does not exist even for large *h*.

e) Hybrid mode characteristics can be very similar for very different silicon thicknesses. This is illustrated in Fig. 3.3. For the cases 3 and 6 {of Table 3.2} the variations of N_{Even}^{HG} and N_{Odd}^{HG} and the cut-off thickness of quasi-odd mode are very similar, although the silicon thicknesses for the two cases are 100 nm and 340 nm, respectively.

This behavior can also be explained using the concept of coupled modes. In the case 3, the hybrid mode results from coupling of the SP mode and the TM_0 mode. As shown in Table 3.2, the difference between the effective mode indices of the constituent modes (Δ_0) is 0.0426. In the case 6, coupling occurs between the SP mode and the TM_1 mode, and the difference between the effective indices in this case (Δ_1) is 0.0344, which is close to that of the case 3. Therefore, variations of the effective mode indices (N_{Even}^{HG} and N_{Odd}^{HG}) and also the cut-off thicknesses for the quasi-odd mode for the two cases are also similar.

3.4. Discussion

In this chapter we have investigated the properties of the modes supported by the HPWG for various choices of waveguide dimensions. We have shown that the characteristics of these modes can be explained by assuming that they result from the coupling of SP and dielectric waveguide modes. The results presented here are useful to understand the guiding mechanism of HPWG. It will also be useful for designing SP based devices, results of which are presented in later parts of the dissertation.

Chapter 4

Analysis of Two Dimensional Hybrid Plasmonic Waveguide

In the last chapter we analyzed the one dimensional HPWG and explained the physical mechanism of mode formation in such guides. For practical applications two dimensional guides are more important and hence in this chapter we investigate the two dimensional HPWG. We begin Section 4.1 with a description of our proposal of two dimensional HPWG. Since our first proposal of HPWG many different variations of the structure has been proposed by various groups. A brief review of these designs is also presented in the same section and a suitable geometry of HPWG for practical applications is identified. Unlike the one dimensional case, the solutions for the guided mode of a two dimensional structure cannot be found using analytical methods and use of numerical methods is essential. The presence of metal as part of a guiding structure makes modeling of plasmonic guides more complicated than dielectric waveguides, and one must carefully choose the numerical method in such a case. Also unlike dielectric waveguides, the choice of performance criterion for plasmonic guides is not straightforward. These issues are discussed in Section 4.2. A detailed investigation of various parameters on the mode characteristics of the two dimensional HPWG is presented in from Section 4.3 to Section 4.7. Section 4.8 concludes the chapter with some remarks.

4.1. Introduction to Two Dimensional Hybrid Plasmonic Waveguide

A finite width hybrid waveguide can be implemented in a number of ways. Fig. 4.1(a) shows the HPWG that we proposed. It consists of a high index dielectric slab (permittivity ε_{hi}) of dimensions $w \times h$ separated from a metallic surface (permittivity ε_{metal}) by a spacer (permittivity ε_{spacer}) of dimensions $w \times d$. The permittivity of the cover layer around the guide is ε_{cover}. The normalized guided power density for the structure at 0.8 μm wavelength is shown in Fig. 4.1(b). In this example the spacer, high index and cover region are assumed to be silica, silicon and air, respectively and the dimensions are w = 100 nm, h = 60 nm, d = 100 nm. Power is highly confined in the low index spacer layer despite the small dimension of the waveguide and the presence of the silicon slab.

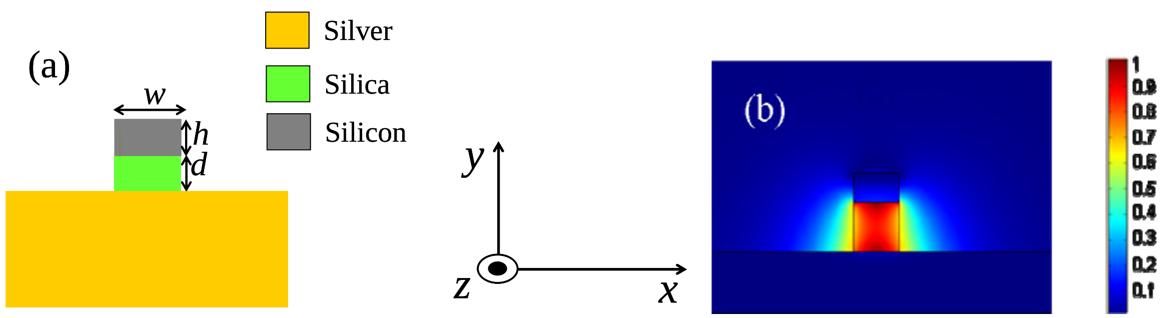

Fig. 4.1. (a) Schematic of the two dimensional hybrid waveguide. (b) Normalized guided power density. Waveguide dimensions and material properties are mentioned in the text.

Because of the ability of HPWGs to guide light in the low index medium and also its ability to support a highly confined mode, the two dimensional HPWG has attracted a lot interest, and our first proposal of HPWG has been followed by investigation of many other types of HPWG. Some of these are shown in Fig. 4.2. One of the most widely known HPWG structure proposed by Oulton et. al. [Oulton 2008], is shown in Fig. 4.2(a). It is very similar to our proposal. The only differences are: they used GaAs instead of silicon and used a circular geometry instead of a rectangular one. Dai et. al. proposed a finite width HPWG which has a metal cap supported by a silica substrate (Fig. 4.2.(b)) [Dai 2009]. The structure can be fabricated on SOI wafer using standard fabrication techniques and has attracted a lot of interest. Various other HPWG structures such as HPWG with semi-infinite spacer layer [Flammer 2010], wedge HPWG [Bian 2011] and HPWG consisting of a silver nanowire separated from a silicon surrounding by a silica spacer [Kou 2011] have also been investigated by various research groups and are shown in Fig. 4.2(c)-Fig. 4.2(e).

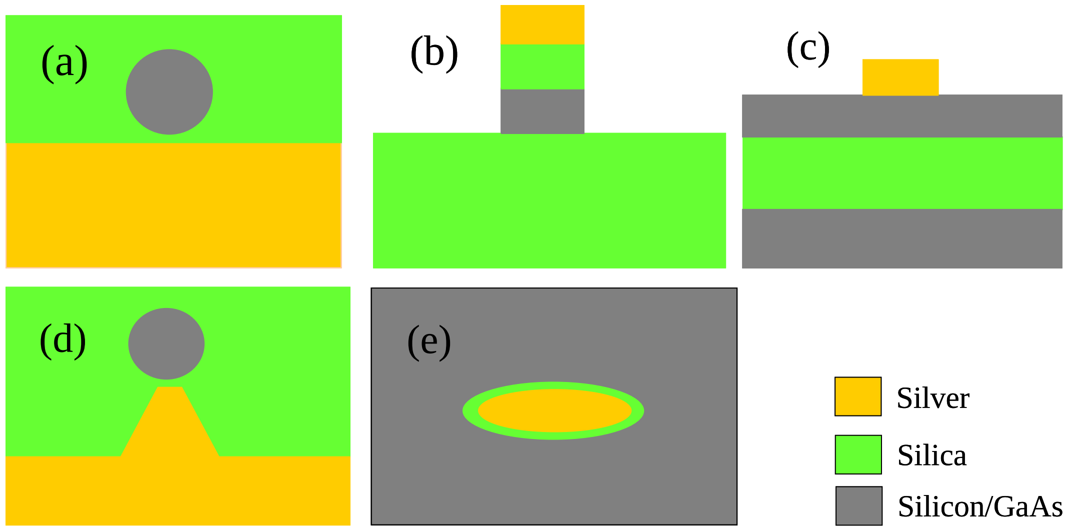

Fig. 4.2. Various types of HPWG proposed in recent years.

As can be seen from Figs. 4.1 and 4.2, the HPWG proposed to date either employ a rectangular or a circular cross section. It is important to know which of these two geometries will provide a better performance before we embark on designing HPWG based devices. One key objective of the current research is to design compact, SOI compatible, nanoplasmonic devices for integrated optic applications. Waveguides which can be closely packed without significant power transfer i.e., those having longer coupling length (the coupling length is defined as the distance necessary for complete power transfer between two coupled waveguides) will be preferred for these applications. We use this definition to determine whether rectangular or circular cross section provides better compactness.

Oulton et. al. [2008] studied in detail the characteristics of circular HPWG and according to their investigation, a minimum mode size is achieved when diameter of the high index circular rod is 200 nm and the spacing between the high index medium and metal is 2 nm. We found from our analysis that a rectangular HPWG with a width of 190 nm, spacer height of 10 nm and silicon height 220 nm, has the same propagation loss as the above mentioned design. We then compare the coupling lengths when two identical HPWG of either circular or rectangular cross section is placed with same edge to edge distance (*D*). Figure 4.3 shows the arrangement of the waveguides along with the variation of coupling length for both cases as a function of *D*. The coupling length is always larger for the rectangular cross section, indicating that it suffers less crosstalk for same waveguide spacing. Although fabrication of nanowire is a well controlled and well understood process, controlling the location of nanowires on a substrate precisely is a challenging task. Implementation of complex integrated optic components therefore, is easier with HPWG of rectangular cross section. We choose to investigate the rectangular HPWG for the remainder of this dissertation.

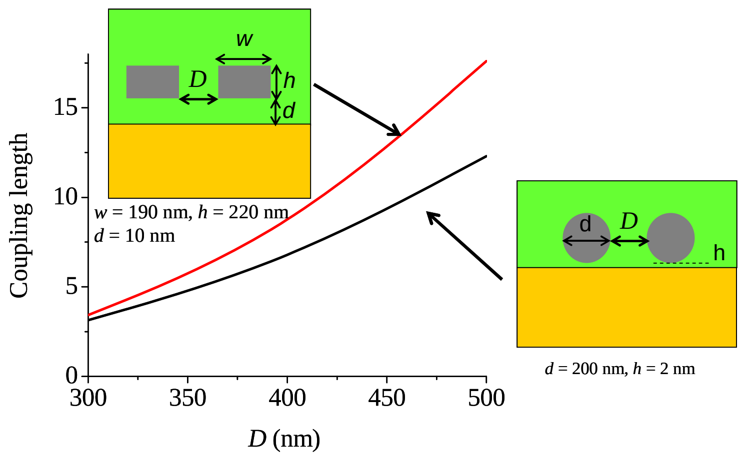

Fig. 4.3. Comparison of coupling length for rectangular and circular hybrid guide for various waveguide spacing.

4.2. Method of Analysis and Some Important Definitions

Despite the impressive progress of fabrication technology in last few years, the production of nanophotonic devices remains a challenging task. Optimizing a design by trial and error in fabrication is not feasible at this length scale. Accurate modeling of device performance is critical in all branches of nanophotonics including nanoplasmonics. As mentioned in Chapter 2, in the optical regime metals have a complex permittivity with a large negative real part. This negative real part of permittivity results in rapid decay of electromagnetic field inside the metal- the skin depth being on the order of tens of nanometers. The numerical method used in plasmonics should be capable of giving satisfactory results for structures with such rapidly varying fields while not using excessive amount of memory. The finite element method is one of the most popular methods for studying plasmonic structures, especially in two dimensions. We have used the commercial finite element code Femlab (now known as Comsol Multiphysics) for analyzing two dimensional structures. Femlab is a very popular finite element solver capable of accurately modeling a wide range of physical problems. The capability of Femlab for modeling plasmonic structures is well documented in literature [Breukellar 2004] and therefore, we refrain from discussing this in detail in our work. Some results which validates Femlab's ability to correctly predict the mode characteristics of HPWG are presented in Appendix A.

A common characteristic of plasmonic guides is that they show a trade off between loss (propagation distance) and confinement (mode size). To optimize a plasmonic guide and also to be able to compare various types of plasmonic guides, propagation distance and mode size need to be defined carefully. The definition of propagation distance of a plasmonic guide is straightforward. It is usually defined as the distance over which the guided power drops to 1/e of its initial magnitude. But unfortunately there is no unanimous definition of mode size followed by the plasmonic community.

Unlike the dielectric waveguides whose field profile is usually either circular or elliptical, the field profile of plasmonic guides can be very complicated, and as a result there is no general agreement about how the mode size should be defined for plasmonic waveguides. A number of different definitions of mode size has been proposed by various researchers. Berini et. al., have analyzed these issues in detail and proposed a number of figures of merit for plasmonic devices [Buckley 2007]. In their work they define mode size as the area bound by the 1/e field magnitude contour relative to the field maximum. Oulton et. al., have defined mode size (A_1) as [Oulton 2008]

$$A_1 = \frac{1}{\max\{W(r)\}} \int W(r) dA \tag{4.1}$$

Here $W(r)$ is the energy density of the mode at location r and the two dimensional integration is carried out up to infinity over the cross section of the waveguide.

The potential applications of SP span a wide range of areas from integrated optics, electronics to biosensing. No definition of mode size is suitable for all types of application. For example, in sensing application it is important to know how tightly the field is confined. The definition of mode size used by Berini would be useful for such applications. For integrated optics the waveguides are usually laterally displaced from one another and the lateral field confinement determines achievable packing density. Neither the definition of Berini or Oulton's will be applicable for these applications. Therefore, in our work we define mode size as the distance over which the transverse electric field E_y along the metal-dielectric interface drops to 1/e of its maximum amplitude. Defining mode size in terms of lateral confinement, as we have chosen to do is a common practice followed extensively by plasmonics community while designing plasmonic waveguides and devices for applications in integrated optics [Bozhevolnyi 2006], [Holmgaard 2010], [Pan 2012].

4.3. Effects of Various Parameters on the Waveguide Performance

In the following we present the effects of wavelength, waveguide dimensions and material properties on the waveguide characteristics for the structure shown in Fig. 4.1(a). Unless otherwise stated, the high index medium is silicon, spacer medium is silica and the cover medium is air. One major motivation behind nanoplasmonic research is the possibility of achieving very high mode confinement. In general the confinement of the plasmon modes decreases as one moves away from the SP resonance frequency. Therefore, if one aims at achieving high confinement, one needs to design the plasmonic guide at shorter wavelengths. Silicon, a part of the HPWG is highly lossy at shorter wavelength. In this chapter, with an aim to attain a small mode size while keeping the propagation loss low, we resorted to a compromise and selected 0.8 μm as the wavelength of operation of the HPWG. This choice also gives us the opportunity to compare the hybrid mode characteristics with those of dielectric loaded waveguide which has close resemblance to HPWG [Steinberger 2006]. The relevant material properties of interest for the HPWG design at 0.8 μm wavelength are summarized in Table 4.1.

Table 4.1. Material properties used for the two dimensional HPWG simulation

Wavelength	0.8 μm
Material properties	ε_{metal}= -32.8+i0.46(silver), ε_{spacer}=2.11(silica) ε_{hi}=13.77+i0.063 (silicon), ε_{cover}=1 (air)

4.4. Effects of Waveguide Dimensions

Figures 4.4 and 4.5 show the effects of waveguide dimensions on the HPWG mode characteristics with variations of waveguide width and spacer height for two silicon thicknesses (h = 60 nm and h = 100 nm). When waveguide width (w) is large and spacer thickness (d) is very small, a significant amount of power is confined in the silicon core, as indicated by large values of effective mode index (Fig. 4.4(a) and Fig. 4.5(a)). Although mode size is very small in such cases (Fig. 4.4(c) and Fig. 4.5(c)), the propagation distance of the guide is also very small (Fig. 4.4(b) and Fig. 4.5(b)). For large d on the other hand the coupling between SP mode supported by the metal-dielectric interface and the dielectric waveguide mode supported by the silicon slab becomes weak. This is indicated by a decrease of effective mode index (Fig. 4.4(a) and Fig. 4.5(a)), increase of propagation distance (Fig. 4.4(b) and Fig. 4.5(b)) and loss of field confinement i.e., increase of mode size (Fig. 4.4(c) and Fig. 4.5(c)).

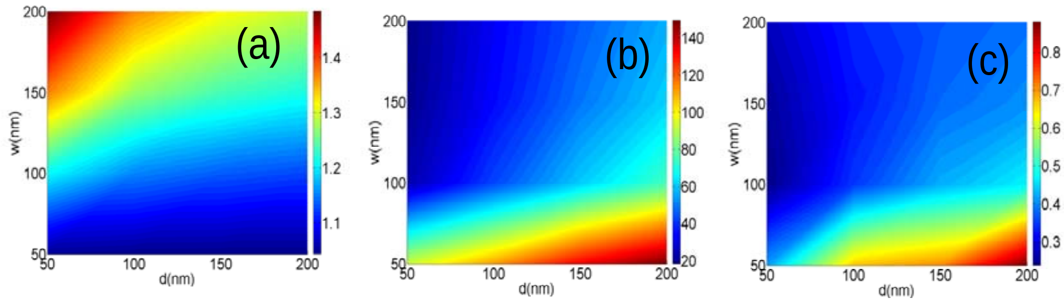

Fig. 4.4. Effects of varying waveguide width and spacer height for h = 60 nm (a) real part of effective mode index (b) propagation distance (μm) (c) mode size (μm).

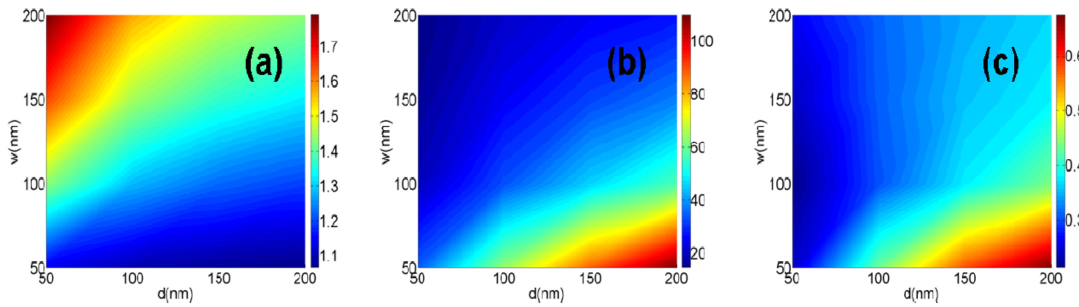

Fig. 4.5. Effects of varying waveguide width and spacer height for h = 100 nm (a) real part of effective mode index (b) propagation distance (μm) (c) mode size (μm).

Table 4.2 summarizes the effects of changing dimensions on waveguide performance. The trends shown in these figure were also observed for other choices of waveguide dimensions.

Table 4.2. Effects of changing different dimensions on waveguide performance

Dimension	Effects of increasing the chosen dimension		
	Effective mode index	Propagation distance	Mode size
Waveguide width (w)	Increases	Decreases	Decreases
High index slab height (h)	Increases	Decreases	Decreases
Spacer height (d)	Decreases	Increases	Increases

We choose the final waveguide dimensions to be *w*=100 nm, *h*=60 nm, *d*=100 nm. Fig. 4.1(b) shows that good confinement of guided power can be obtained for these dimensions. Propagation distance in this case is 43 μm and the mode size is 350 nm. We take this as a reasonable compromise between confinement and propagation distance.

4.5. Effect of Wavelength

The waveguide dispersion for the wavelength range of 0.5 to 1.2 μm is shown in Fig. 4.6. The dispersions of silica [Palik 1985], silicon [Palik 1985], and silver [Johnson 1972], [Dionne 2005] have been taken into account. As shown in Fig. 4.6(a), the mode is tightly confined at shorter wavelengths while the confinement becomes worse for longer wavelengths. This is expected since for longer wavelength light penetrates more into the cladding, resulting in a loss of confinement. Figure 4.6(b) presents the variations of the real part of the mode effective index and propagation distance as a function of wavelength. For longer wavelengths the mode penetrates deeper into air and the real part of effective mode index (n_{eff}) approaches 1. Like other plasmonic guides, there is a trade off between the propagation distance and confinement for the hybrid waveguide. As shown in Fig. 4.6(b), the loss of confinement is accompanied by an increase of propagation distance.

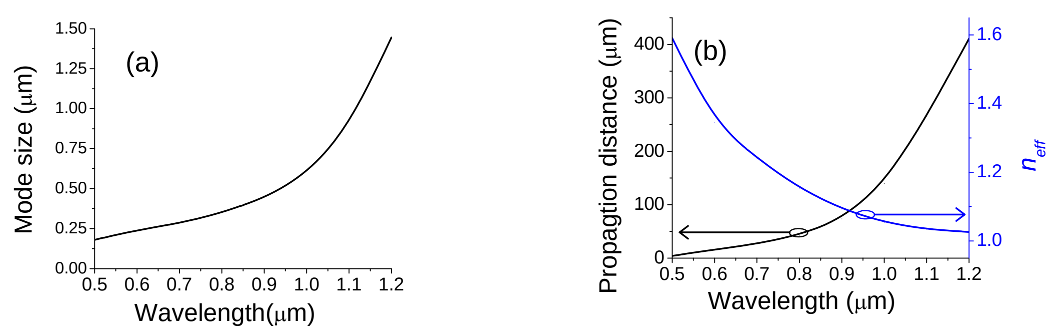

Fig. 4.6. Dispersion of the proposed guide (a) mode size (b) propagation distance and real part of effective mode index for waveguide dimensions *w*=100 nm, *h*=60 nm, *d*=100 nm.

4.6. Effects of Permittivity of the Cover Layer

Fabrication of the structure shown in Fig. 4.1(a) will require the deposition of silica on a metal surface followed by the deposition of silicon on top of silica and subsequent etching of these two layers. An alternate and easier fabrication process would be to implement the HPWG on SOI wafer as shown in Fig. 4.7(a). The fabrication steps will be selective etching of silicon to define the high index region followed by deposition of silica and metal. The cover medium i.e., the medium around the HPWG in this case will be silica instead of air. Hybrid mode supported by such a guide is shown in Fig. 4.7(b).

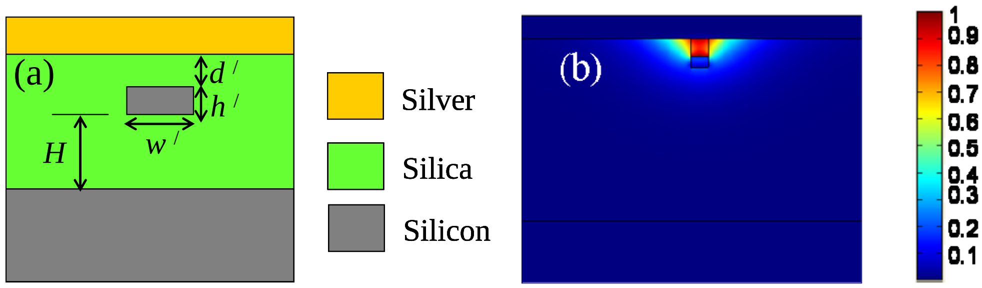

Fig. 4.7. (a) Schematic of the two dimensional hybrid guide on SOI wafer (b) normalized guided power density for waveguide dimensions w/=100 nm, h/=60 nm, d/=100 nm, H=1 μm.

We have investigated the effects of varying the permittivity of the cover region and show these results in Fig. 4.8. The HPWG structure investigated is the same as shown Fig. 4.1(a). The waveguide dimensions are w=100 nm, h=60 nm, d=100 nm. As shown in Fig. 4.8(a) an increase in ε_{cover} results in a loss of confinement and accompanying increase of mode size. This loss of confinement is accompanied by an increase in the effective mode index N_{eff} as shown in Fig. 4.8(b). Propagation distance reaches a maximum when ε_{cover} is approximately equal to ε_{spacer}. At a wavelength of 800 nm silicon has a complex permittivity and the resulting loss is appreciable. To examine the effect of material loss of silicon on overall propagation distance we have also plotted the propagation distance in absence of silicon loss. While silicon loss plays an important role in limiting the propagation distance, the metal loss is the main limiting factor.

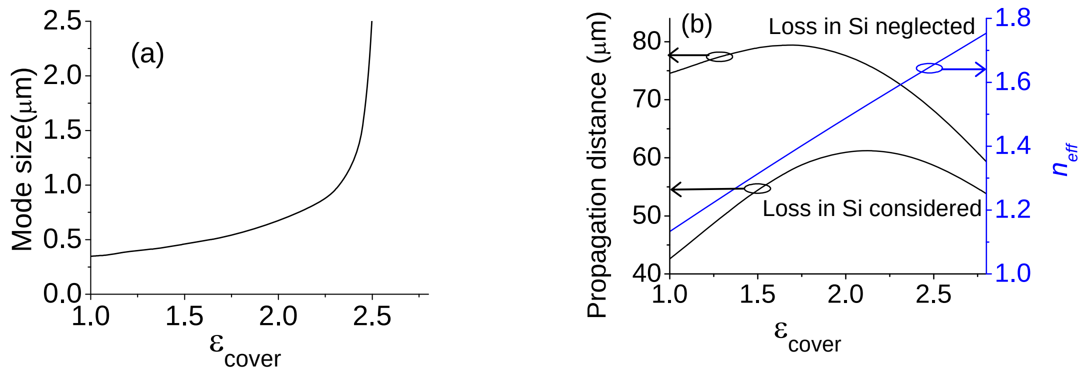

Fig. 4.8. Variations of mode characteristics as a function of the permittivity of surrounding medium for the HPWG structure (a) mode size (b) propagation distance and real part of effective mode index. The waveguide dimensions are *w*=100 nm, *h*=60 nm, *d*=100 nm. Wavelength of operation is 0.8 μm.

The variation of propagation distance for the hybrid mode differs significantly from that of single interface SP mode. The propagation distance of the SP at a single metal-dielectric interface (δ_{sp}) is given by [Raether 1988].

$$\delta_{SP} = \frac{1}{k_0}\left(\frac{\varepsilon_m' + \varepsilon_d}{\varepsilon_m' \varepsilon_d}\right)^{3/2} \frac{(\varepsilon_m')^2}{\varepsilon_m''} \tag{4.2}$$

Here ε_m' and ε_m'' are the real and imaginary parts of the metal permittivity and ε_d is the permittivity of the dielectric medium adjacent to the metal. The variation of δ_{SP} for a silver dielectric interface at 0.8 μm wavelength as a function of ε_d is shown Fig. 4.9. Unlike the case of the hybrid mode, the propagation distance in this case drops monotonically with increasing ε_d. For example when ε_d increases from 1 to 2, δ_{SP} drops by almost 65%. In contrast, Fig. 4.8(b) shows that for the hybrid waveguide structure propagation distance changes by less than 24% for same change in ε_{cover}. Also instead of changing monotonically, propagation distance becomes maximum for an optimum choice of ε_{cover}.

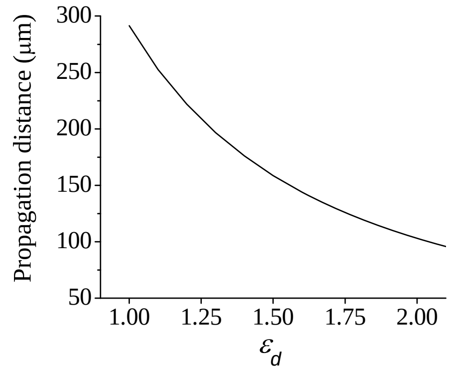

Fig. 4.9. Variation of propagation distance for SP at silver dielectric interface as a function of dielectric constant. Wavelength of operation is 0.8 μm.

To explain the attenuation characteristics of the hybrid mode, the variation of the field confinement in metal and silicon for the structure shown in Fig. 4.1(a), are plotted as a function of ε_{cover} in Fig. 4.10(a). For comparison variation of field confinement in metal for single interface SP mode is plotted in Fig. 4.10(b). Here confinement in the region i (η_i) is defined as

$$\eta_i = \frac{\iint_i |E_y| dxdy}{\int_{-\infty}^{\infty}\int_{-\infty}^{\infty} |E_y| dxdy} \tag{4.3}$$

Assuming the dielectric is lossless, the attenuation of SP at a metal dielectric interface will depend on the field confinement in metal. With the increase of permittivity of the surrounding medium, a larger fraction of the field goes in the metal resulting in reduced propagation distance. Since the proposed structure is operating near the band gap of silicon, the loss in silicon cannot be neglected. The attenuation of the guided mode will depend on the field confinement in metal and silicon. With the increase of ε_{cover} more field is in the metal which tends to increase the loss. An increase of ε_{cover} also results in less contrast between the silicon slab and surrounding medium. More field spreads out of the silicon slab and this effect tends to reduce the loss. These opposing effects make the reduction of propagation distance smaller for the hybrid mode.

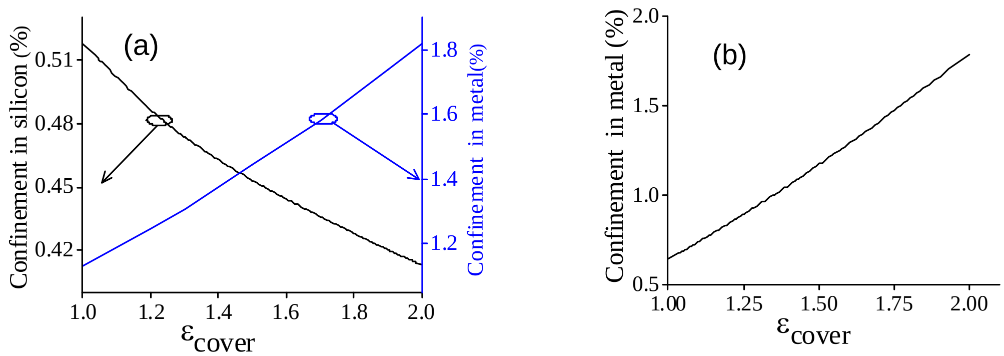

Fig. 4.10. Variation of field confinement with permittivity of cover layer (a) two dimensional HPWG (b) dielectric silver interface. The waveguide dimensions are w=100 nm, h=60 nm, d=100 nm. Wavelength of operation is 0.8 μm.

4.7. Effect of the Permittivity of Spacer Medium

Figure 4.11 shows the variation of modal characteristics of HPWG as a function of spacer permittivity (ε_{spacer}). Increase of ε_{spacer} results in better confinement (Fig. 4.11(a). As expected this reduction of mode size is accompanied by a decrease of propagation distance and increase of effective mode index (Fig. 4.11(b)).

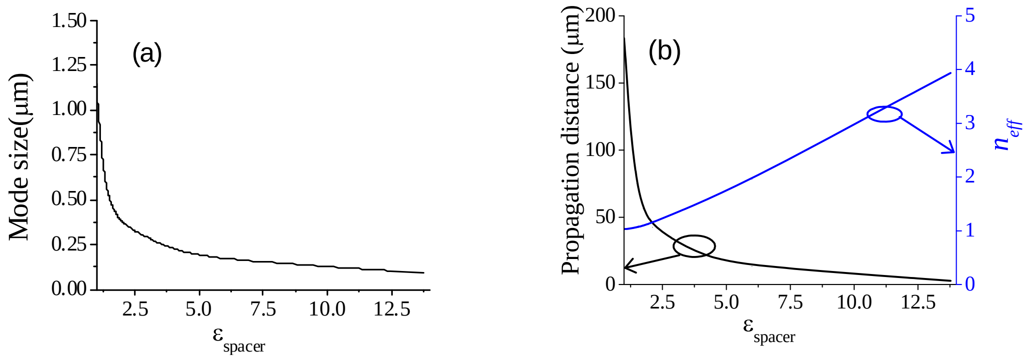

Fig. 4.11. Variations of mode characteristics as a function of the permittivity of spacer medium (a) mode size (b) propagation distance and real part of effective mode index.

4.8. Discussion

In this chapter we have analyzed the two dimensional hybrid waveguides. We have compared the rectangular and circular HPWG and shown that the former provides more compactness than the circular HPWG. We have also investigated in detail the effects of wavelength, waveguide dimensions and material properties on the hybrid mode characteristics. These results provide an estimate of the mode size and propagation distance achievable. It also sets the groundwork for the design of integrated optic HPWG which will be focus of next chapter.

Chapter 5

Hybrid Plasmonic Waveguide Devices for Integrated Optics

From the discussion of previous chapters we can identify a number of attractive features of HPWG. It offers a better compromise between loss and confinement than single interface SP modes. The fabrication of a HPWG is compatible with standard SOI fabrication technology, and it can be easily integrated with silicon waveguides on a SOI platform. Unlike dielectric waveguides where light is concentrated in the high index medium, in case of HPWG a significant amount of light is concentrated in the low index spacer layer. Because of these attractive features, HPWG has attracted a lot of interest, and many different applications of HPWG have been suggested; for example nano scale lasers [Oulton 2009], Bragg gratings [Xiao 2011], ring resonators [Chu 2011], and parametric amplifiers [Zhou 2010].

In addition to supporting a hybrid TM like mode which has been widely studied, the HPWG can also support a TE mode. This is illustrated in Fig. 5.1. Figure 5.1(a) shows cross section of a HPWG. As shown in Fig. 5.1(b) power for the TM mode supported by the structure is highly concentrated in the low index spacer region (silica, in the present case). On the other hand, power for the TE mode is very similar to conventional dielectric waveguide mode and is concentrated in the high index region i.e., in the silicon layer (Fig. 5.1(c)). Since the two modes are guided in two different layers, changing the dimensions and material properties of these layers will affect the two modes in different ways. Although a lot of attractive features of HPWG have been discussed and exploited by the plasmonic research community for various applications, the possibility of using the polarization diversity to make useful devices has attracted no attention. In our work on the applications of HPWG, we have taken a different approach than other groups and concentrated mostly on the utilization of polarization diversity. This chapter presents the results of our effort on designing HPWG devices for integrated optic communication system on an SOI platform.

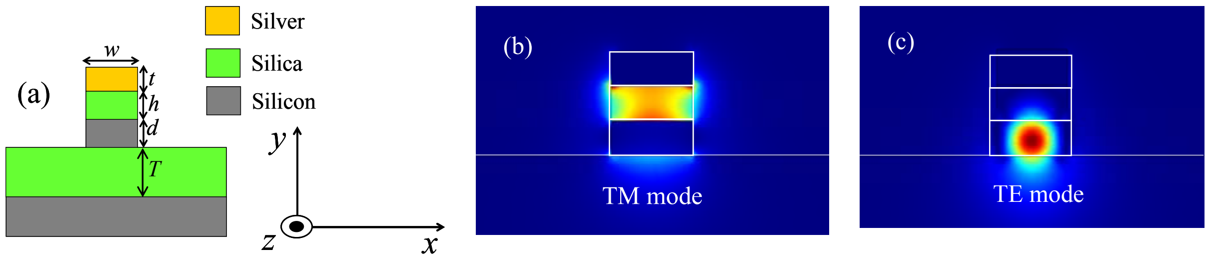

Fig. 5.1. (a) Cross section of the hybrid plasmonic waveguide. (b) Power density for the TM mode. (c) Power density for the TE mode. Waveguide dimensions are $w = 350$ nm, $t = 200$ nm, $h = 150$ nm, $d = 150$ nm, $T = 2$ μm. Wavelength of operation is 1550 nm.

In this chapter we present the designs of TE and TM-pass polarizers, polarization independent directional couplers, and waveguide bends. For each device, we begin with a brief review of previously reported designs. This is followed by description of the HPWG based device design and a comparison with previous work. We conclude this chapter with a few general comments about the design of HPWG based devices.

A few comments regarding the numerical methods used in this work are relevant before we discuss the designs in detail. Some commonly used numerical methods in integrated optics are the beam propagation method (BPM), finite element method (FEM) and finite difference time domain method (FDTD). BPM is a very fast and efficient numerical method when the paraxial approximation is valid. The high index contrast of silicon and silica renders the approximation invalid and the modeling of HPWG will require use of fully vectorial BPM which does not offer significant performance benefit over other numerical methods. BPM is therefore, rarely used in modeling plasmonic devices. Both FEM and FDTD are extensively used for plasmonic simulations. However, FDTD offers some advantages over FEM. For example, since FDTD is a time domain method, the performance over a broad wavelength range can be obtained from a single simulation. We have used the commercial FDTD code Lumerical for investigating the performance of our proposed devices. The simulations are carried out on multiple processors in parallel on the high performance computing facility

WestGrid. To achieve high accuracy without excessive demand of computational resources, we have used a nonuniform mesh with a finer mesh at the metal-dielectric interface and relatively coarse mesh else where. We have carried out simulations with different mesh sizes and found that decreasing the minimum mesh size below 2 nm does not significantly affect the simulation results. Therefore we have used a nonuniform mesh with a minimum mesh size of 2 nm in these simulations.

An important issue in the modeling of plasmonic devices is the choice of material parameters to be used. Although the values of permittivity for dielectric materials available in literature are usually consistent, the metal permittivity and especially its imaginary part is highly dependent on growth condition and the reported values for it varies widely from one report to another. In our work we have taken material data for all dielectric materials, unless otherwise stated from [Palik 1985] and the metal permittivity data has been taken from [Johnson 1972]. In addition to the material loss, plasmonic devices also suffer from scattering loss due to roughness of the metal surface. This loss has been ignored in all these simulations, a practice common in plasmonics. Therefore, in a real device, the loss should be slightly higher than predicted by the simulation. However, the scattering loss should not be very large if the fabrication steps are optimized and hence the results presented in this work should give a very good estimate of the losses expected from HPWG devices in practice.

The wavelength of operation chosen for all the designs presented in this chapter is the telecommunication band (around 1.55 μm). The only exception is the HPWG waveguide bend presented in Section 5.4. The reason behind this choice is explained in Section 5.4.2.

5.1. Hybrid Plasmonic TM-pass Polarizer

5.1.1. Previous Work on TM-pass Polarizer

Waveguide polarizers are an essential part of many integrated optic systems, including coherent optical communication systems, optical sensors, switches, interferometers and amplifiers. Controlling the polarization states is also very important for high index contrast platform like SOI. The high index contrast makes SOI devices highly birefringent and this issue must be taken into account while designing any optical system involving SOI. For example, the polarization state in a standard optical fiber varies randomly, and connecting it directly to an SOI optical chip may disrupt the proper function of the latter. One solution to this problem is to use a polarization diversity scheme, where the two polarization states are separated at the input of the SOI chip and processed separately. This results in an increased system size and complexity. Another solution which is satisfactory for many practical situations is to use a polarizer to extinguish the unwanted polarization state. Depending on the application either TE-pass or TM-pass polarizers may be necessary. For example, since SP is TM in nature, an integrated plasmonic biosensor may require a TM-pass polarizer to extinguish the unwanted TE mode.

Integrated optic TM-pass polarizers can be implemented in many different ways including the utilization of optical anisotropy, use of nano structured materials, photonic crystals and resonant buffer layers. The optical absorption of metal nonspherical nano particles strongly depends on their shape and orientation with respect to the electric field. By depositing nonspherical silver nano-composite film on a waveguide surface, a TM-pass polarizer can be realized [Bloemer 1996]. Waveguides separated by a buffer layer can be used to implement either TM-pass or TE-pass polarizer [Thyagarajan 1991]. In this approach the waveguide supporting the optical signal (Guide 1) is separated from a thin high index waveguide (Guide 2) by a buffer layer. To implement a TM-pass polarizer the dimensions of Guide 2 and the buffer layer are designed such that the TE modes supported by the two guides are resonantly coupled and hence power for the TE mode transfers from Guide 1 to Guide 2, which is then allowed to leak as a radiation mode. Since the operation of these devices requires phase matching, they are very sensitive to fabrication imperfections. Moreover, because of the relatively higher index of Guide 2, some power for the TM mode also leaks to Guide 2, which results in appreciable insertion loss for the TM mode. A combination of a metal clad and a resonant layer can provide very large extinction ratio (>30 dB) with very low insertion loss for the TM mode (<0.4 dB) [Li 2008]. Lengths of all the devices mentioned above are on the order of millimeters - limiting their applicability in nanophotonics.

Highly compact and SOI compatible TM-pass polarizer can be implemented in several ways. The photonic band gap structure for TE and TM modes are significantly different and therefore, photonic crystals can be used to guide only one polarization while the other polarization is reflected back. This mechanism can be used to implement either a TE-pass or TM-pass polarizer [Zhao 2002, Cui 2008]. Simulation results indicate that these polarizers can be very compact, can provide large extinction ratio with very low insertion loss for the desired mode. However, fabrication of these devices is challenging and their performance is very sensitive to fabrication imperfection [Zhao 2002]. It is also possible to design a silicon waveguide such that the TE mode is forced below cut off whereas the TM mode is well guided. Q. Wang et.al. have proposed a silicon nanowire polarizer using this concept [Wang 2010]. The device is very easy to fabricate, can be readily integrated with other silicon nanowire waveguides, and offers a large extinction ratio (>25 dB) for a short device length (18 μm). The design, however works only for certain buried oxide thicknesses. A somewhat similar principle was used in [Ng 2010]. A narrow silicon waveguide with copper strips on either side is used to block the propagation of TE polarization. The device length is only 100 nm. The extinction ratio, however, is rather small (11.5 dB).

5.1.2. Design of Hybrid Plasmonic TM-pass Polarizer

Figure 5.2(a) shows the schematic of the proposed HPWG TM-pass polarizer. It consists of a HPWG inserted between two silicon waveguides. Figure 5.2(b) and 5.2(c) show the cross sections of the HPWG section and the input/output silicon waveguides respectively. The coordinate system is defined with respect to (b) and (c) with the xz plane coinciding with the silicon waveguide-buried oxide interface and its origin located at the beginning of the HPWG section. By properly choosing the dimensions it is possible to cut off the TE mode while the TM mode is well guided. The structure shown in Fig. 5.2(a) then acts as a TM-pass polarizer.

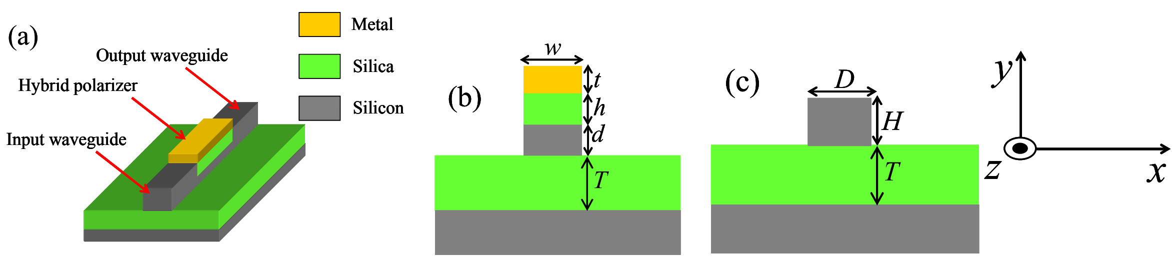

Fig. 5.2. (a) 3D schematic of the complete TM polarizer (b) Cross section of the HPWG section (c) Cross section of the input and output silicon waveguides.

For designing practical devices using the HPWG including polarizers, it is necessary to have a clear understanding of how the choice of waveguide dimensions and material properties affect the characteristics of both TE and TM modes. Although the two dimensional HPWG has been analyzed in some detail in Chapter 4, no comparison between the TE and TM mode characteristics were made. We have carried out some additional numerical analysis to obtain this information, results of which are presented below. The metal, high index material and spacer medium for this design are silver, silicon and silica respectively. Fig. 5.3(a) and 5.3(b) show the effects of spacer thickness (h) and silicon thicknesses (d) on effective mode index (n_{eff}) for TM and TE modes, respectively for the structure shown in Fig.5.2(b) for these choices of material properties. Here, effective mode index, n_{eff}, is defined as $n_{eff} = k/k_0$ where k is the phase constant of the guided mode and $k_0 = \omega/c$ is the free space wave number. Reduction of spacer thickness results in an increase of n_{eff} for the TM mode but the opposite is true for the TE mode. When silicon thickness is large (e.g., d = 200 nm), both modes exist for any spacer thickness considered here. For small silicon thickness (e.g. d = 100 nm) the hybrid waveguide supports only the TM mode.

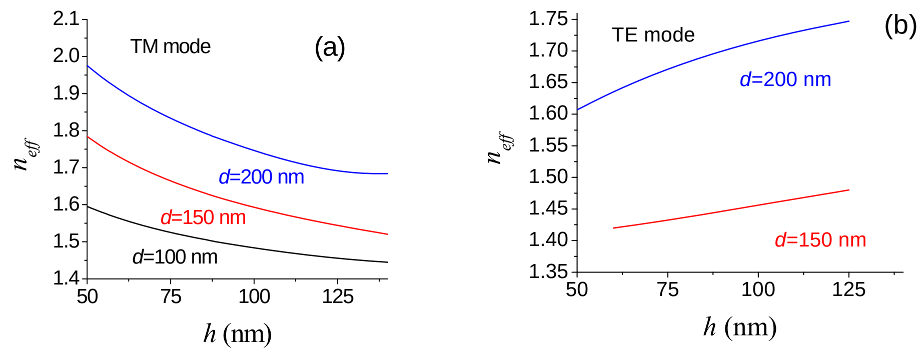

Fig. 5.3. (a) and (b): Variations of effective mode index (n_{eff}) for TM and TE modes with spacer thickness (h) for a number of fixed silicon thicknesses (d). Other dimensions are w = 350 nm, t = 200 nm, T = 2 μm. Wavelength of operation is 1.55 μm.

Figure 5.4 shows the variations of propagation distance for the two modes with varying waveguide dimensions for the structure shown in Fig. 5.2(b). The TM mode is lossier than the TE mode for all choices of silicon and spacer thicknesses. The propagation distance of the TM mode decreases monotonically with reduced spacer thickness. Propagation distance of the TE mode follows the same trend when silicon thickness is large (e.g., d = 200 nm). For a reduced silicon thickness (e.g., d = 150 nm) the propagation distance of the TE mode is small for intermediate values of spacer thicknesses.

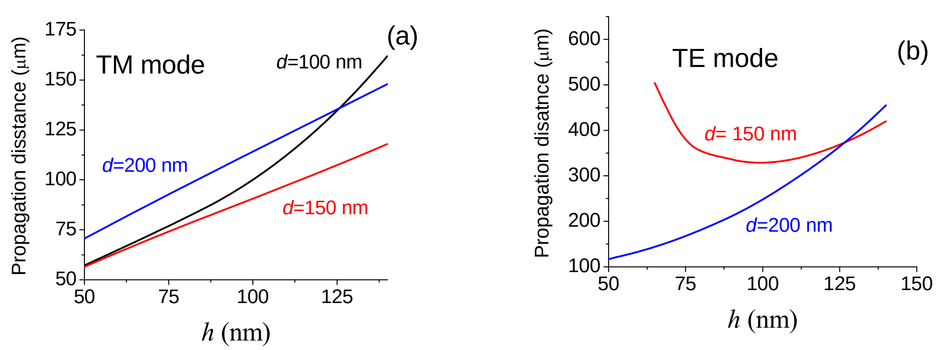

Fig. 5.4. (a) and (b): Variations of propagation distance for TM and TE modes with spacer thickness (h) for a number of fixed silicon thicknesses (d). Other dimensions are w = 350 nm, t = 200 nm, T = 2 μm. Wavelength of operation is 1.55 μm.

To explain the reason behind the variations of mode characteristics presented in Figs. 5.3 and 5.4, we have plotted the power density profiles of both modes. Figure 5.5 shows the power density of the TM mode for different spacer thicknesses (*h*). The dominant electric field component of the TM mode is perpendicular to the metal as shown by the electric field arrows in the figures. With reduced spacer thickness, the mode is more tightly confined and n_{eff} is larger as shown in Fig. 5.3(a). Like all plasmonic guides this increased confinement is accompanied by reduced propagation distance as shown in Fig. 5.4(a).

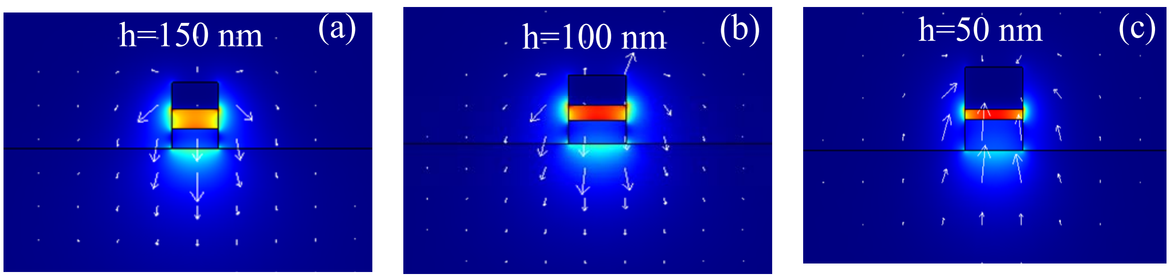

Fig. 5.5. Variations of power density of the TM mode with spacer thickness *h*. (a) h = 150 nm, (b) h = 100 nm, (c) h = 50 nm. The other dimensions are w = 350 nm, t = 200 nm, d = 150 nm, T = 2 μm. Wavelength of operation is 1.55 μm.

Figure 5.6 shows the power density of the TE mode for a number of spacer thicknesses. The field is concentrated in the high index region (silicon) and since the silicon film is thin in this case (d = 150 nm), the field is loosely confined. For large spacer thickness the mode is not significantly affected by the metal and propagation distance is large (propagation loss is low). As the spacer thickness is reduced, the mode is more affected by the presence of metal and propagation distance decreases (propagation loss increases). According to the boundary conditions of electric field, the tangential electric field is zero on the surface of a perfect conductor. Though silver is not a perfect conductor at near infrared, it still has a large negative real part of permittivity and can be considered a "good conductor". Hence, for a small spacer thickness the dominant electric field component of the TE mode, which is tangential to the metal surface, is pushed away from the metal. The net result is the following: for small spacer and silicon thicknesses the TE mode is pushed into the substrate and approaches the cut off condition as shown in Fig. 5.3(b). Since in this case the power resides mostly in the substrate (a "good dielectric") metallic losses are reduced. Therefore, for a thin silicon film (e.g., d = 150 nm) propagation distance is minimized for an intermediate choice of spacer thickness as shown in Fig. 5.4(b).

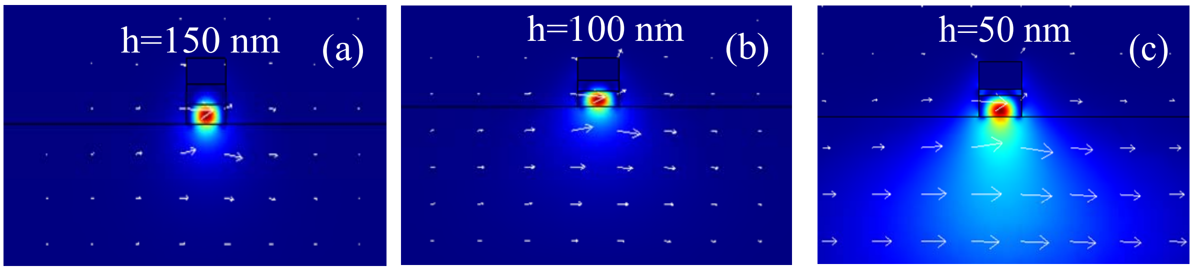

Fig. 5.6. Variations of power density of the TE mode with spacer thickness h. (a) h = 150 nm, (b) h = 100 nm, (c) h = 50 nm. The other dimensions are w = 350 nm, t = 200 nm, d = 150 nm, T = 2 μm. Wavelength of operation is 1.55 μm.

Since the TE mode can be cut off by properly choosing the dimensions while the TM mode is still well guided, it is possible to implement a TM pass polarizer using the HPWG. This is the working principle of the HPWG TM-pass polarizer.

Based on the simulation results presented in Fig. 5.3 and 5.4, we choose the dimensions of the TM-pass polarizer to be w = 350 nm, t = 200 nm, h = 50 nm, d = 100 nm. The dimensions of the input/output silicon waveguides chosen for this work are D = 350 nm and H = 300 nm. For these dimensions both TM and TE modes are well guided by the input/output waveguides. Finite difference time domain (FDTD) code Lumerical is used to investigate the performance of the polarizer. Figures 5.7(a) and 5.7(b) show power density profiles of the TM and TE modes, respectively along the polarizer for 1.55 μm wavelength for an 18 μm long polarizer. This device length is chosen to facilitate comparison of the HPWG based design with previously reported designs of TM-pass polarizer, as explained in more detail in section 5.1.3. The TM mode is well guided from the input to the output, although it suffers some propagation losses. The TE mode, on the other hand, is below cutoff, and hence is unable to propagate through the HPWG section.

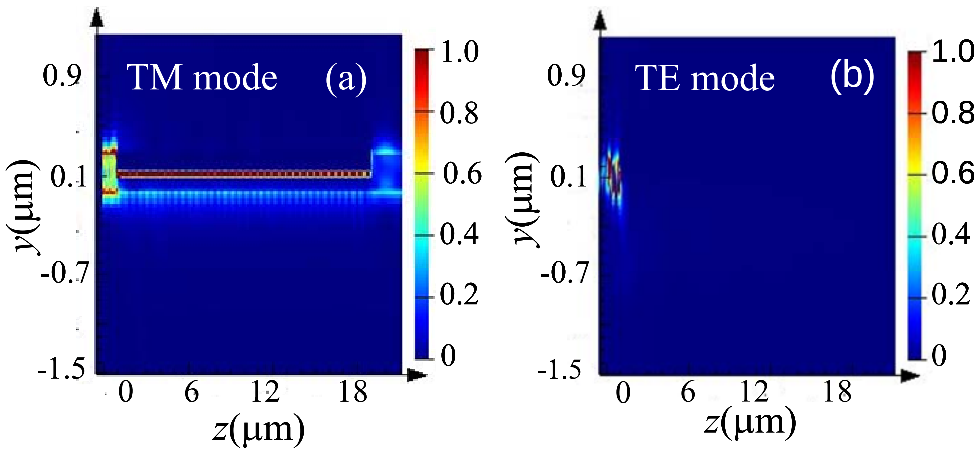

Fig. 5.7. Power density plots for the light propagating through the polarizer. (a) TM mode (b) TE mode for the proposed TM-pass polarizer.

The thickness of buried oxide layer (*T*) varies for commercially available SOI wafers and it was shown in previous works that proper choice of *T* is critical for proper operation of the TM-pass polarizer [Wang 2010]. Therefore, we have also carried out an analysis to determine the effect of *T* on the HPWG TM-pass polarizer performance. Figure 5.8 shows the insertion loss of the TM and TE modes for an 18 µm long polarizer for two different values of *T*. The HPWG section inserted between the silicon waveguides act as a cavity. Therefore ripples in the insertion loss spectrum of the TM mode are present which result from Fabry Perot resonance. Since most of the power of the TE power is leaked out of the waveguide and there is little propagation along the HPWG section, this effect is not observed for the TE mode. The operation of the device is not seriously affected by change of *T* and the extinction ratio (difference between the insertion loss of TM and TE modes) is high for both cases.

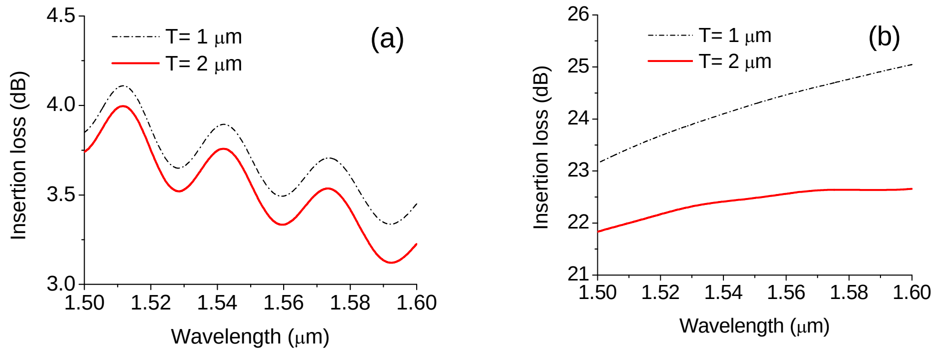

Fig. 5.8. Insertion losses of the HPWG TM-pass polarizer for (a) TM mode (b) TE mode. Device dimensions are w = 350 nm, t = 200 nm, h = 50 nm, d = 100 nm.

The insertion loss of both TM and TE modes for various polarizer lengths are shown in Fig. 5.9. Although we have chosen 18 μm as the device length in the example above, the HPWG polarizer can also provide a high extinction ratio for a shorter polarizer length. For example, a 13 μm long hybrid polarizer (with all other dimensions the same as in Fig. 5.8 caption) provides 21.8 dB and 3.2 dB insertion loss for the TM and TE modes, respectively, i.e., an extinction ratio of 18.6 dB.

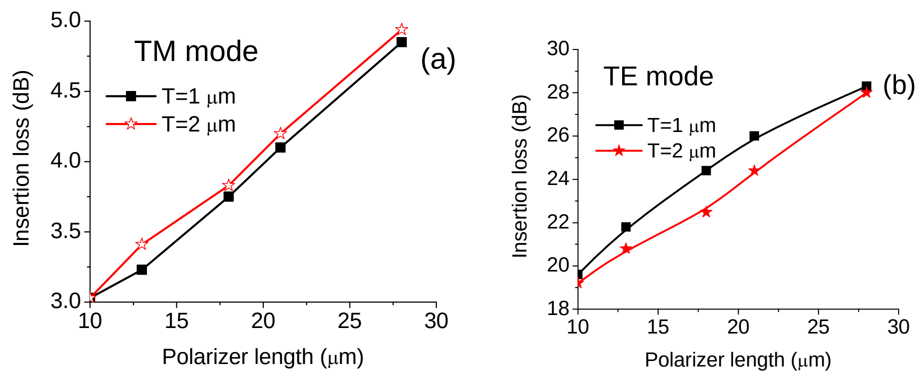

Fig. 5.9. Insertion losses of the TM-pass polarizer for two different buried oxide thicknesses. (a) TM mode (b) TE mode. Wavelength of operation is 1.55 μm.

The insertion loss of the TM mode is caused by three factors: material loss due to the presence of metal, mismatch of mode profile between the HPWG segment and input/output silicon waveguides, and reflection caused by the mode index mismatch between the HPWG and input/output waveguides. Because of the compact size of the proposed device, less than one third of the insertion loss results from material loss. The mode size in both HPWG and the silicon input/output waveguides are very similar and hence loss resulting from mode size mismatch is expected to be low. However, because of the difference of the effective mode indices for the TM modes in the HPWG section and input/output silicon waveguide sections, significant reflection occurs. One solution to this is to use a taper section between the input/output waveguides and the HPWG section. Design of taper for mode matching is a well studied and well understood topic, and hence will not be discussed in this work.

5.1.3. Comparison with Previously Reported SOI Compatible TM-pass Polarizers

A good TM-pass polarizer should provide large insertion loss for the TE mode and negligible insertion loss for the TM mode. To be applicable in nanophotonics, the device should also be very compact. The HPWG TM-pass polarizer easily outperforms most previously reported SOI based TM-pass polarizers in these respects. For example, it provides much better extinction ratio compared to [Ng 2010] and is much shorter than the other polarizers mentioned in section 5.1.1 for the same extinction ratio. The comparison between our proposal and the "silicon nanowire polarizer" [Wang 2010] needs more careful consideration. Therefore, we present here the comparison in some detail.

The performance of the polarizer proposed in [Wang 2010] is optimum when the length of device is 18 μm and buried oxide layer thickness is 1.5 μm. For these dimensions the insertion loss of the TE mode is 26 dB and the insertion loss of the TM mode is negligible (FDTD simulation results reported in [Wang 2010]), resulting in an extinction ratio of 26 dB. We recognize the impressive performance of the silicon nanowire polarizer and *in fact our final device length of 18 μm in section 5.1.2 was chosen to give us the opportunity to compare our proposal against the best alternative available in literature*. The performance of the silicon nanowire polarizer degrades significantly for smaller buried oxide layer thicknesses. To illustrate this we plotted the insertion loss for the TE mode for the TM-pass polarizer of [Wang 2010] for two different buried oxide thicknesses in Fig. 5.10. Insertion loss of the TM mode is negligible and hence not plotted here. For 1 μm buried oxide thickness and 18 μm polarizer length, the extinction ratio is 14 dB. Moreover, increasing the polarizer length does little to solve this problem. Even if the polarizer length is increased to 28 μm, for 1 μm buried oxide thickness, the TE insertion loss is still moderate (≈16dB).

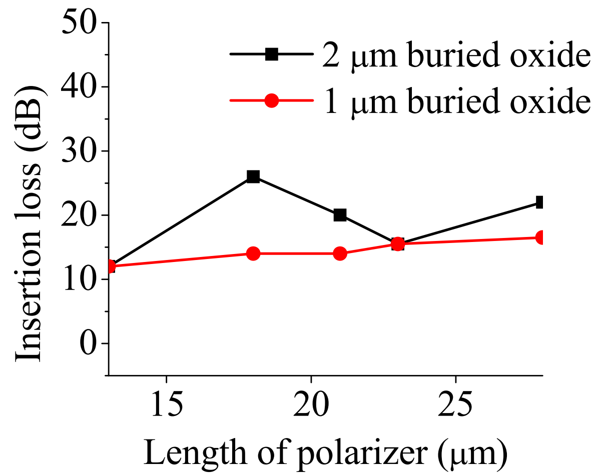

Fig. 5.10. Insertion loss of the TE mode for two different buried layer thickness for the silicon nanowire TM pass polarizer reported in [Wang 2010].

Although the polarizer is an important device, it is typically only one part of a complicated optical chip which may contain many other components. Some of these components may require an oxide thickness different than the one required by the polarizer. For example the optical amplifier described in [Park 2007] requires a 1 μm thick oxide layer for ensuring heat dissipation and proper operation. One motivation behind the wide adoption of SOI technology for photonics is the potential of integration of photonics and electronics on same platform. Thin oxide layer (1 μm or even less) is preferred for proper operation of many electronic circuits [Stefanou 2004]. Application of silicon nanowire polarizer in such cases will result in a negligible insertion loss for TM mode but also a small extinction ratio. Polarization purity is important for proper operation of many devices, and in such cases a polarizer with a high extinction ratio is highly desirable. Application of the silicon nanowire polarizer may not be satisfactory in such cases and an alternate design is worth consideration.

As shown in Figs. 5.8 and 5.9, the performance of HPWG based design is little affected by the change of buried oxide thickness and works very well even for a 1 μm thick oxide layer. Moreover, although, we have chosen a polarizer length of 18 μm to facilitate a fair comparison with the best possible alternative available in literature, our device can also provide a high extinction ratio for a shorter length, i.e., *it can also be more compact than previous design for same extinction ratio*. To illustrate this extinction ratios for the two polarizers are compared for various polarizer lengths in Fig. 5.11 (buried oxide thickness is 1 μm). For a 13 μm polarizer length, the extinction ratio for our design is 18.6 dB in contrast to 12 dB for the nanowire polarizer. More importantly for our design, the extinction ratio can be increased significantly by increasing the polarizer length but for the nanowire polarizer, the increase in extinction ratio with increased polarizer length is rather small. The improved in extinction ratio, comes at the cost of higher insertion loss for TM mode as illustrated in Fig. 5.9. But we believe the high extinction ratio achievable by the hybrid TM-pass polarizer can still be useful in many applications.

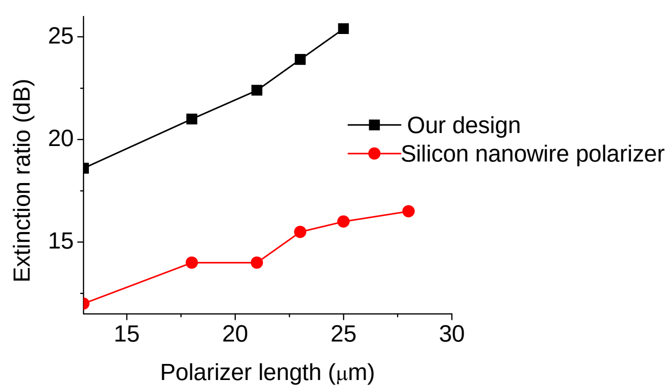

Fig. 5.11. Comparison of the extinction ratios for our design and silicon nanowire polarizer.

In summary we identify the following advantages of our proposal (for small buried oxide thickness).

1) Our design can provide high extinction ratio even for a very small polarizer length, which is not possible for the silicon nanowire polarizer.

2) By increasing the length, it is possible to achieve very high extinction ratio, which is not possible by the silicon nanowire polarizer, although this comes at the cost of a larger insertion loss for the TM polarization.

3) The implementation of HPWG based polarizer requires more process steps compared to the silicon nanowire polarizer, although all of these steps are compatible with standard SOI fabrication technology.

We therefore, conclude that the HPWG based TM-pass polarizer can be a better choice than previously reported SOI based TM-pass polarizers in many practical situations.

5.2. Hybrid TE-pass Polarizer

5.2.1. Previous Work on TE-pass Polarizer

Like the TM-pass polarizer, the TE-pass polarizer is also a very important component of integrated optical circuits and many different designs of such polarizers have been reported. Metal clad polarizers are the most common type of TE-pass polarizer [Sharma 2011]. In this structure, the waveguide is separated from a metal surface by a buffer layer. For proper choice of buffer thickness and index, the TM mode supported by the waveguide resonantly couples to the SP mode supported by the metal-dielectric interface and is attenuated because of propagation loss of SP. The TE mode on the other hand propagates relatively unaffected. A variation of the same idea was used by Avurtsky to design the shortest, broadband TE-pass polarizer designed to date [Avurtsky 2008]. The device extinguishes the TM mode by coupling it to a gap SP mode supported by a metal-insulator-metal structure. Shallowly etched silicon waveguide can supports TE mode while the TM mode is lost as leaky mode. This mechanism has also been used to implement TE-pass polarizer [Dai 2010]. J. Cheng et. al., experimentally demonstrated a single polarization silicon waveguide separated from the underlying silica layer by a pedestal realized by wet etching [Cheng 2011]. In addition to these proposals photonic crystal structure and resonant buffer layers, described in section 5.1.1 can also be used to implement TE-pass polarizer. Regarding applicability in SOI nanophotonics the TE-pass polarizer reported to date suffer from a number of limitations- either they are too long, too narrow band or have high insertion loss for the TE mode. A compact, low-loss, broadband SOI compatible TE-pass polarizer is yet to be reported.

5.2.2. Design of Hybrid Plasmonic TE-pass Polarizer

The configuration of HPWG TE-pass polarizer is very similar to that of the TM-pass polarizer (Fig.5.2) with the exception that the metal is chromium, instead of silver. The TM mode in a hybrid guide is concentrated in close vicinity of the metal. In contrast the TE mode is concentrated in the high index region. As a result the TM mode is always more lossy for such a guide. For a proper choice of waveguide dimensions, the TM mode propagating though the hybrid waveguide will suffer very high attenuation while the TE mode will be relatively unaffected. Inserting such a HPWG section (shown in Fig. 5.2(b)) between two input/output silicon waveguides (shown in Fig. 5.2(c)) will result in a TE-pass polarizer.

A good SOI compatible TE-pass polarizer should have

a) low insertion loss for the TE mode

b) high insertion loss for the TM mode

c) compact size.

For ease of discussion in this work we define the ratio of propagation loss of the two polarizations (η) as

$$\eta = \frac{\text{Propagation loss of TM mode (dB/}\mu\text{m)}}{\text{Propagation loss of TE mode (dB/}\mu\text{m)}} \tag{5.1}$$

Fulfillment of Condition (a) requires good effective mode index matching for the TE mode between the input/output silicon waveguide and the HPWG section. To simultaneously satisfy conditions (a) and (b), η has to be large. If the propagation loss for the TM mode per unit length is large, a high TM insertion loss will be achieved over a short polarizer length, which satisfies condition (c). The material properties and polarizer dimensions must be carefully chosen to simultaneously satisfy all three conditions.

Noble metals (gold and silver) can provide low propagation loss for plasmonic modes and are the metals of choice for most plasmonic devices. However, in the present case we prefer large losses for the hybrid mode and a metal having a large imaginary part of permittivity in near infra red, for example, chromium ($\varepsilon_r \approx -6.7+41i$) is a better choice. Chromium has very good adhesion to dielectric surfaces and hence will make the fabrication of the device less challenging. Therefore, chromium is chosen as metal in our design. Two possible choices of spacer material are silica ($\varepsilon_r \approx 2$) and silicon nitride ($\varepsilon_r \approx 4$). Since the latter choice gives a larger propagation loss for the TM mode, in this work we have chosen silicon nitride as the spacer material. The material properties of silicon nitride at telecommunication bands are not available from [Palik 1985]. Different permittivity values of silicon nitride are reported in literature by different groups but the values are all close to 4. Therefore, for silicon nitride we used a constant permittivity value ($\varepsilon_r = 4$). Permittivity of silicon nitride changes by less than 2 % over the wavelength range of our investigation (1.4 - 1.6 μm) and neglecting the dispersion of silicon nitride should not significantly affect the results.

Since the choice of waveguide dimensions affects the two modes differently, the waveguide dimensions need to be properly chosen to achieve large value of η. We have carried out a detailed analysis using commercial finite element code Femlab (now known as Comsol Multiphysics) to investigate the effects of waveguide dimensions on the modal properties. Figure 5.12 shows the effects of changing h and d for fixed waveguide width (w = 550 nm). Both propagation loss for the TM mode and η are large for large silicon thickness (d) and spacer thickness (h) as shown in Fig. 5.12(a) and 5.12(b). Figures 5.12(c) and 5.12(d) show the variations of real part of effective mode index $\{n_{eff}\}$ for the TE and TM modes, respectively. Large silicon thickness (d) results in a large n_{eff} for the TE mode, which results in better match between the input/output and silicon waveguide. However, as shown in Fig. 5.12(a), this also results in a much lower value of propagation loss of the TM mode. The final device dimensions chosen are: w = 550 nm, d = 120 nm, h = 500 nm, t = 200 nm to simultaneously satisfy conditions (a), (b) and (c). For these dimensions and a chromium layer on top of the spacer, the propagation loss for the TM mode is 3.7 dB/μm and the value of η is 152, whereas for gold these values become 0.2 dB/μm and 143, respectively. Therefore, chromium is a better choice for implementing a compact hybrid TE-pass polarizer.

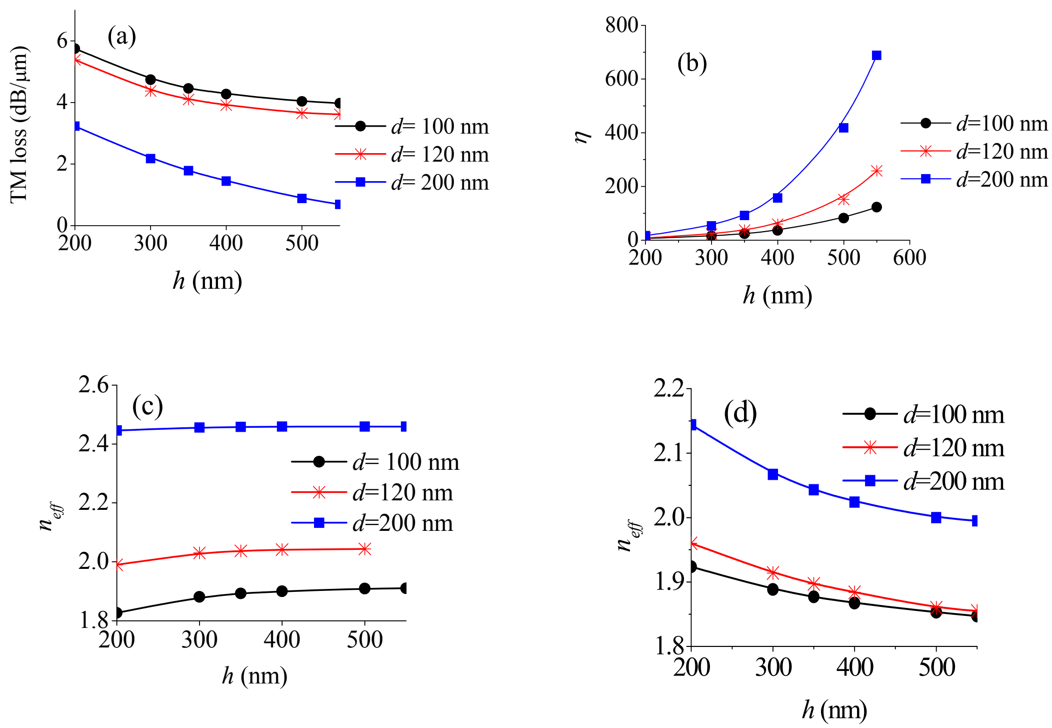

Fig. 5.12. Variations of the modal characteristics with spacer thickness (h) for a number of silicon thicknesses (d). (a) Propagation loss of TM mode (b) Ratio of TM and TE loss (η). (c) Effective mode index for TE mode. (d) Effective mode index for TM mode. Other dimensions are w = 550 nm, t = 200 nm, T = 1.5 μm. Wavelength of operation is 1.55 μm.

Performance of the complete device along with the input and output silicon waveguides is investigated by running full wave three dimensional FDTD simulations using Lumerical. The input/output silicon waveguide dimensions are chosen to be D = 350 nm and H = 310 nm. To minimize device length, no taper is used between the hybrid waveguide and silicon waveguides. The computational volume is 30 μm long, 4 μm wide in the lateral direction and 3.5 μm wide in the vertical direction and is terminated with perfectly matched layers. Figure 5.13 shows the insertion loss spectrum for the TE and TM modes of a 17 μm long polarizer. The hybrid waveguide placed between two silicon waveguides act as a Fabry Perot cavity as evident from the oscillations in the TE transmission spectrum (Fig. 5.13(a)). The large propagation loss diminishes the Fabry- Perot effect in case of TM mode and the TM transmission spectrum (Fig. 5.13(b)) exhibits no oscillation.

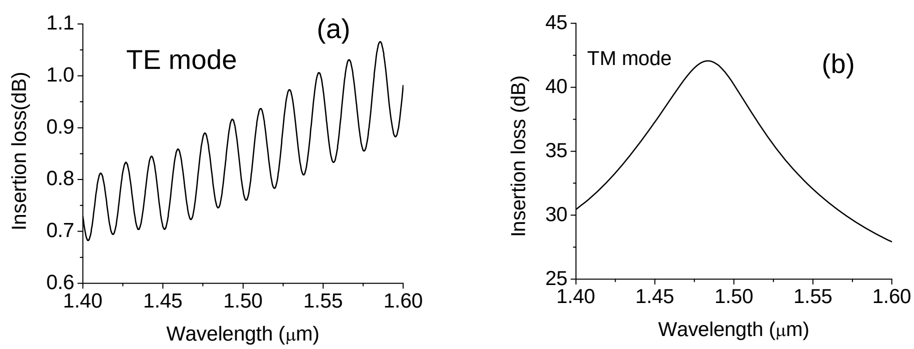

Fig. 5.13. Variation of insertion loss with wavelength for a 17 μm long polarizer. (a) TE mode. (b) TM mode. Waveguide dimensions are w = 550 nm, d = 120 nm, h = 500 nm, t = 200 nm, T = 1.5 μm.

Figure 5.14 shows the insertion losses for the TE and TM modes for various polarizer lengths at 1.55 μm wavelength. A large extinction ratio (difference between the insertion losses for the TE and TM modes) can be achieved for a very short polarizer length. For example an 8 μm long polarizer provides an extinction ratio of approximately 20 dB. The TE insertion loss undergoes sinusoidal variation as a function of polarizer length due to Fabry Perot effect. The insertion loss is slightly higher for a polarizer length around 14 μm. For the optimized design most power for the TE mode propagates through the hybrid waveguide from input to output silicon waveguide. However, part of the power leaks into the buried oxide layer, reflects back at the buried oxide/silicon substrate interface and then couples to the output guide. The amount of this coupling and hence insertion loss is maximum for a certain polarizer length. This phenomenon is well known for waveguide polarizers and was explained in more detail in [Wang 2010].

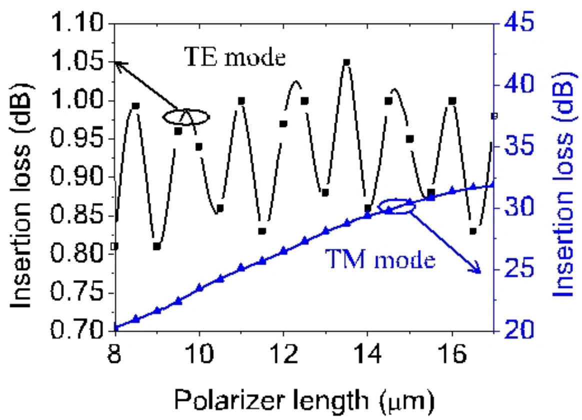

Fig. 5.14. Variations of TE and TM insertion losses with polarizer length for the final design.

The results presented above neglected nonlinear effects on the polarizer performance. The performance of the device may be affected by nonlinear effects at high power levels in a number of ways. For example the propagation loss will increase because of two photon absorption (TPA) and also there will be an additional phase accumulation because of the intensity induced change in refractive index. Here we examine the change of propagation loss and additional phase accumulation for the TE mode. The TPA coefficient (α_2) and nonlinear refractive index (n_2) of silicon at 1.55 μm wavelength are 0.45 cm/GW and 6×10^{-18} m^2/W respectively [Tsang 2002]. We neglect the nonlinear effects in silica because they are much weaker in silicon than in silica [Koos 2007].

The refractive index of silicon (n) and absorption coefficient (α) of silicon at intensity I of light is given by $n = n_0 + n_2 I$ and $\alpha = \alpha_0 + \alpha_2 I$ where n_0 and α_0 are refractive index of and absorption coefficient of silicon at low intensity. We consider 10 mW power input to the polarizer. For this power level, the propagation loss due to TPA effect for an 17 μm long polarizer is increased by 0.2 dB. The change of index of silicon due to the self phase modulation introduced by this change is also negligible. The fact that for the HPWG devices significant amount of power is concentrated in the low index spacer region, make them less susceptible to nonlinear effects compared to silicon waveguides.

5.2.3. Comparison with Previously Reported SOI Compatible TE-pass Polarizer

Metal clad polarizers [Sharma 2011] are the most common type of TE-pass polarizer. Since these polarizers depend on phase matching between SP mode and the dielectric waveguide mode, they are very sensitive to fabrication imperfection. Since the proposed device does not require phase matching, the performance of the device is not seriously degraded with some deviation from the design specification. This is illustrated in Table 5.1. Even if the thickness of silicon or silica is changed by tens of nanometers, the performance of the TE-pass polarizer remains acceptable.

Table 5.1. Effect of varying silicon and spacer thickness on TE-pass polarizer performance

Dimensions	**Maximum TE transmission loss (dB)**	**Maximum TM transmission loss (dB)**	**Comment**
d = 120 nm h = 500 nm w = 550 nm	1.07	42.1	Final design
d = 150 nm h = 500 nm w = 550 nm	0.8	37.6	Silicon thickness changed from final value
d = 120 nm h = 300 nm w = 550 nm	4.1	44.8	Spacer thickness changed from final value

To the best of our knowledge the most compact broadband TE pass polarizer for SOI reported so far has a length of 120 μm [Avrutsky 2008]. Simulation results for the polarizer reported in [Avrutsky 2008] predicted an insertion loss of more than 30 dB for the TM mode and 2 to 4 dB for the TE mode over a bandwidth of 350 nm. In contrast, as shown in Figs. 5.13(a) and (b), our proposed TE pass polarizer suffers much lower insertion loss for the TE mode (approximately 1 dB) and more than 30 dB insertion loss for more than 120 nm bandwidth. Though the bandwidth is lower than that reported in [Avrutsky 2008], the extinction ratio (difference between TE and TM transmission loss) is more than 30 dB over the entire S and C band and the device length is only 14.2 % of that reported in [Avrutsky 2008].

In conclusion the proposed HPWG based TE-pass polarizer is the shortest, broadband, SOI based TE-pass polarizer proposed to date.

5.2.4. Experimental Demonstration of HPWG TE-pass Polarizer

As explained in section 1.1, the key objectives of this dissertation are to examine the characteristics of modes supported by HPWG and to design HPWG based devices. However, we have also started working on the fabrication and testing of some of the devices we designed. In this section we report the experimental results for the HPWG TE-pass polarizer. The work was done in collaboration with Xiao Sun, an M. A. Sc. student of our group. The samples were fabricated in collaboration with Xiao Sun and the sample characterization was also carried out by her.

Although we have presented the optimized design of a TE-pass polarizer in section 5.2.2, we decided to implement a slightly modified design which is more compatible with the nanofabrication facility available at the University of Toronto. Similar to the polarizer shown in Fig. 5.2(a), the modified design consist of a HPWG section between two silicon waveguide. Figures 5.15(a) and 5.15(b) show the cross section of the HPWG and input/output silicon waveguides. Power density profiles for the TE and TM modes supported by the HPWG section are shown in Fig. 5.15(c) and 5.15(d) respectively. Similar to the TE mode supported by a dielectric waveguide power for the TE mode is concentrated in the high index medium i.e., silicon. The TM mode on the other hand is a hybrid mode and concentrated in the silica between the metal and silicon similar to the design described in Section. 5.2.2.

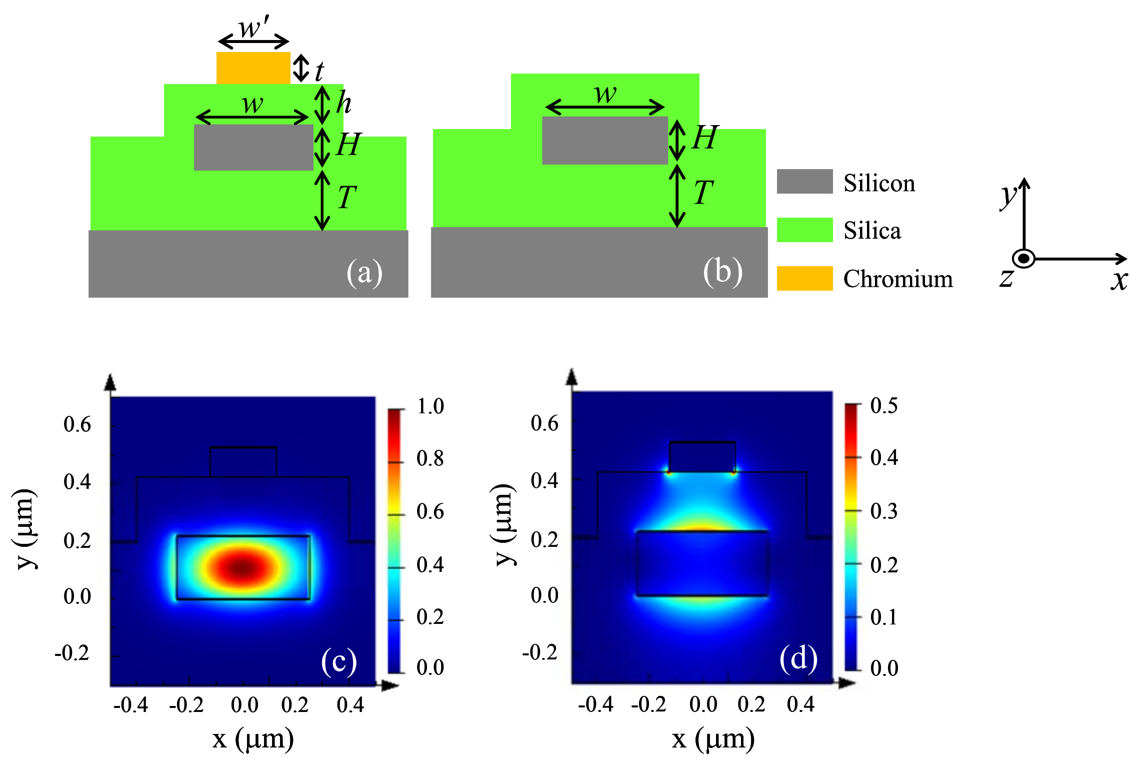

Fig. 5.15. (a) and (b) Cross sections of the HPWG and the input/output silicon guide (c) and (d) Power density profiles of the TE and TM modes supported by the HPWG section. Dimensions are w = 350 nm, w$^{/}$ = 250 nm, h = 250 nm, d = 200 nm, t = 100 nm, T = 3 μm. Wavelength of operation is 1.55μm.

Using finite difference time domain (FDTD) code from Lumerical we optimized the design of the TE-pass polarizer. The optimization process is very similar to that mentioned in section 5.2.2, and hence will not be repeated here. The final dimensions of the HPWG sections are w = 350 nm, w' = 250 nm, h = 250 nm, d = 200 nm, t = 100 nm, T = 3 μm, and dimensions of the input/output silicon waveguides are w = 350 nm, H = 250 nm. Fig. 5.16 shows the insertion loss for a 30 μm long HPWG TE-pass polarizer inserted between two silicon waveguides of dimensions

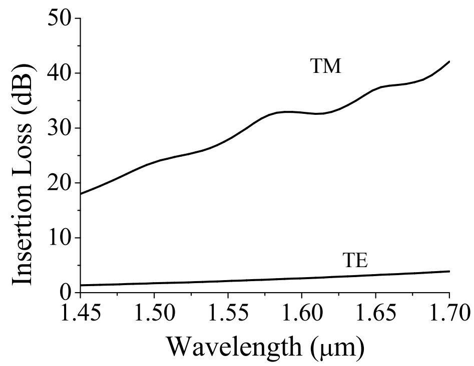

Fig. 5.16. Insertion loss of a 30 μm long TE-pass polarizer predicted by FDTD simulation. Device dimensions are as mentioned in the caption of Fig. 5.1.

The TE-pass polarizer was implemented on a SOI wafer consisting of a 220 nm thick silicon device layer on a 3 μm buried oxide layer supplied by Soitec (Fig. 5.17(a)). The process steps are summarized in Fig. 5.17. In the first step positive electron beam resist Zep 520 was spun on the substrate and patterned using electron beam lithography (Fig. 5.17(b)). This was followed by reactive ion etching to define the silicon waveguides and the silicon section of the HPWG (Fig. 5.17(c)). A 200 nm thick silica layer was then deposited over the sample using plasma enhanced chemical vapor deposition (Fig. 5.17(d)). Using an electron beam lithography step, the area where chromium needs to be deposited was defined (Fig. 5.17(e)). The sample was then covered with 150 nm thick chromium using thermal evaporation process followed by lift off to complete the fabrication (Fig. 5.17(f)). Since the fabrication requires multiple steps, proper alignment was required between various steps. Gold markers on sample surface (not shown in Fig. 5.17) were used for this purpose.

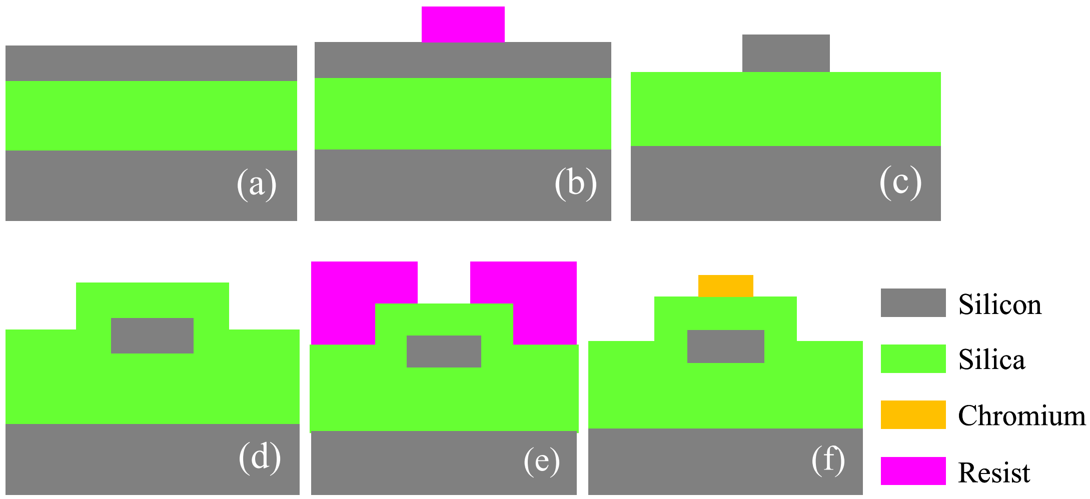

Fig. 5.17. Fabrication process flow of the HPWG TE-pass polarizer (a) SOI substrate (b) Resist spin-coating and electron-beam pattern (c) RIE etching (d) Silica deposition by PECVD (e) Resist spin-coating and electron beam patterning (f) Chromium deposition and lift-off.

Figure 5.18(a) shows the optical microscope image of the final sample. A number of TE-pass polarizers of various lengths were fabricated on the same chip. In addition a number of reference channels were also fabricated. The reference channels are identical to the TE-pass polarizer branches with the exception that they have no HPWG sections. Fig. 5.18(b) and 5.18(c) show the SEM images of the top view and end facet of the HPWG section. The 250 nm wide chromium section is located almost at the middle of the HPWG - which confirms the precise alignment achieved in our fabrication. Because of the imperfect etching using RIE the silicon waveguide is of trapezoidal shape with the width of the trapezoid varying from 580 nm at the bottom to 420 nm at the top. Consequence of this deviation from the desired rectangular section will be discussed later in this section.

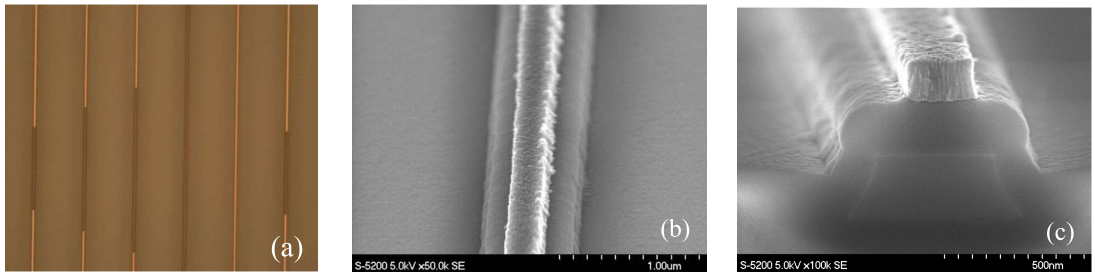

Fig. 5.18. (a) Optical microscope image of several HPWG TE-pass polarizers and one reference waveguide (second guide from right end). (b) SEM image of the top of HPWG section. (c) SEM image of the cross section of HPWG.

Figure 5.19 shows the experimental setup used to test the fabricated device. Power from a continuous wave laser was coupled to free space from a single mode fiber. The polarization of the light is controlled using a combination of a half wave plate and a polarizing beam cube. The sample was mounted on a rig and two 40x microscope objectives were used to couple light in and out of the sample. An infrared camera was used at the output to ensure that light is coupled properly to only one waveguide at a time. The power output of the TE-pass polarizer branch was compared to that of the reference branch to measure the insertion loss of the TE-pass polarizer.

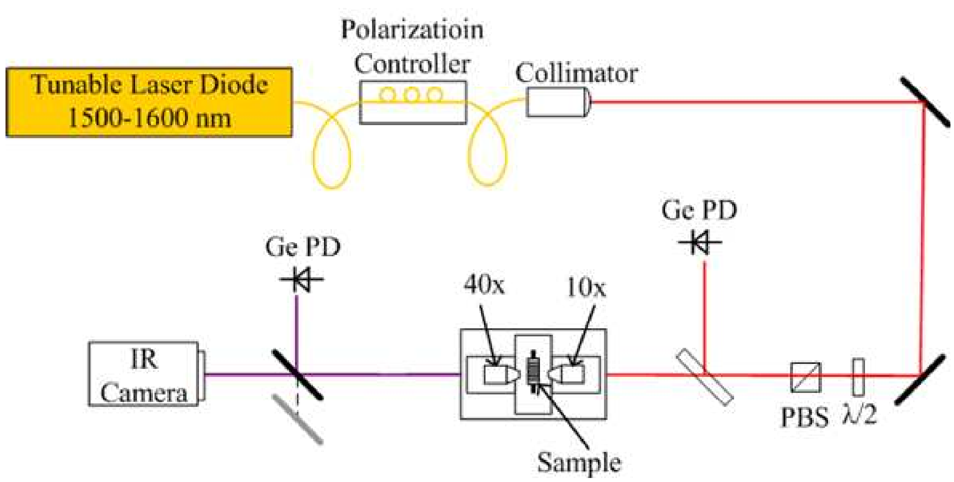

Fig. 5.19. Experimental set up used for optical characterization of the HPWG TE-pass polarizer.

The measured insertion loss for both TE and TM modes are shown in Fig. 5.20 over a wavelength range of 1.52 to 1.58 μm. The extinction ratio varies from 19 dB to 25 dB for this range. Although the device is expected to work well even beyond this wavelength range, the finite bandwidth of our tunable laser precludes measurement over a wider range. For ease of comparison between simulation and measurement, we have plotted the predicted insertion loss obtained from FDTD simulations for this wavelength range in Fig. 5.20(b). Comparison of Fig. 5.20(a) and (b) confirms good agreement between simulation and experiment. The slight discrepancy between the results is not unexpected. In our simulation we assumed that the silicon waveguides and the HPWG section have rectangular cross section. However, as shown in Fig. 5.18(c) the cross sections are trapezoidal, which may affect the insertion loss. For our simulations, we have taken the material properties of chromium from [Palik 1985]. The permittivity of metal and especially the imaginary part of permittivity can vary significantly depending on the growth condition - which will also result in some discrepancy. We have also neglected loss due to scattering from surface roughness in our simulation - a practice common in plasmonic research. All these will contribute to discrepancy between simulation and measurements but the agreement between the measurement and simulation is still good. The good agreement also confirms the validity of the other designs presented in this dissertation.

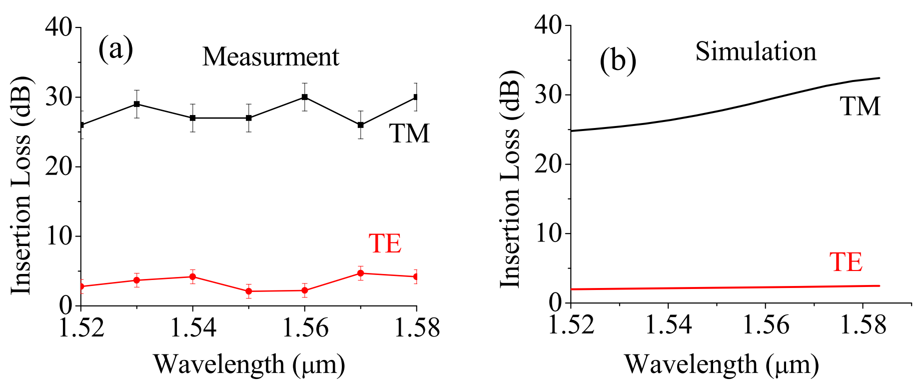

Fig. 5.20. Insertion loss of the TE and TM modes for a 30 μm long HPWG TE-pass polarizer. (a) Measurement (b) Simulation.

In section 5.2.2 we predicted that the HPWG TE-pass polarizer can outperform previously proposed SOI compatible TE-pass polarizers. Here we compare results of our experiments with relevant experimental results to confirm this. Although many different types of TE-pass polarizers have been investigated in the past, the number of experimental demonstrations of SOI-based TE pass polarizers are very few [Bhat 2012, Dai 2010]. Silicon rib waveguide coated with aluminum can act as a TE-pass polarizer [Bhat 2012] but the device length is more than a millimeter and the extinction ratio achievable is relatively low (< 20 dB). Shallowly etched ridge waveguide TE-pass polarizer reported in [Dai 2010] is very simple to fabricate and the insertion loss of the TE and TM modes achieved for the device are comparable to that of our current work but the device is 1 mm long. In contrast we have achieved an extinction ratio of more than 20 dB and moderate loss for the TE mode for a device length of only 30 μm. Our work therefore is a considerable progress compared to previous works.

5.3. Hybrid Plasmonic Polarization Independent Directional Coupler

5.3.1. Previous Work on SOI Compatible Polarization Independent Directional Coupler

Directional couplers are widely used for many integrated optic applications; for example in implementing power splitters, signal tap lines and for implementation of electro-optic switches. As shown in Fig. 5.21(b), a directional coupler consists of two waveguides placed close to each other. Under this condition, the modes supported by the two guides couple and form even and odd modes. As light propagates along these couples lines, periodic power transfer takes place between the waveguides in the manner shown in Fig. 5.21(c).

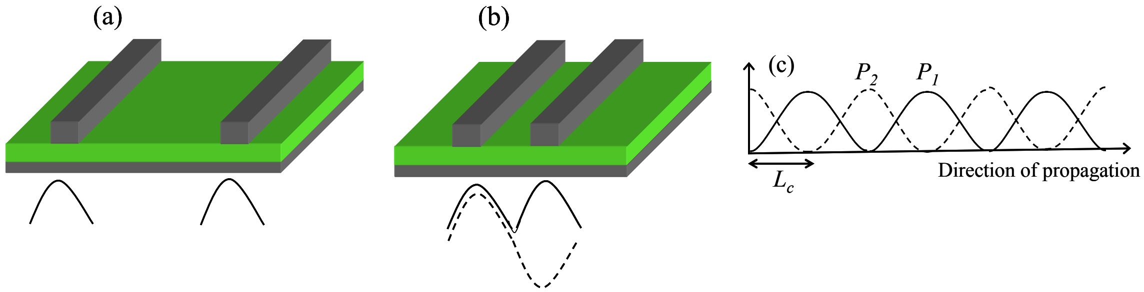

Fig. 5.21. (a) Normal modes in two uncoupled waveguides (b) Normal modes in two coupled guides (c) Interchange of power between the two guides with distance. P_1 and P_2 are power in the two waveguides shown in (b).

The important figures of merit of a directional coupler are its insertion loss, power transfer ratio and coupling length. Insertion loss (*IL*) is defined as the power lost in the coupler from input to output. If the input power is P_{in} and power output from branch 1 and 2 are P_1 and P_2 respectively, the insertion loss (in dB) is given by

$$IL = 10\log\left(\frac{P_1 + P_2}{P_{in}}\right) \qquad (5.2)$$

Coupling length (L_C) is the distance necessary for complete power transfer from one guide to the other guides. It is given by

$$L_C = \pi / (\beta_{even} - \beta_{odd}) \qquad (5.3)$$

Here, β_{even} and β_{odd} are the phase constants of the even and odd modes.

The power transfer ratio (Γ) can be defined as the fraction of total output power delivered to the two output branches. In our case the ratio will be given by

$$\Gamma = \frac{P_1}{P_2} \qquad (5.4)$$

Since operation of the directional coupler depends on the coupling between the modes, the change in mode profile will significantly affect the coupling length. As a result directional couplers are inherently polarization dependent. This is illustrated with an example in Fig.

5.22. Fig. 5.22(a) shows a directional coupler consisting of two silicon waveguide. The power transfer ratio spectrum for the TE and TM modes for a directional coupler implemented by placing two such guides at 200 nm spacing is shown in Fig. 5.22(b). As expected, Γ is strongly dependent on polarization of light. This polarization dependence may be problematic for many applications. Although extinguishing one polarization state is a viable solution for many cases, there are applications, where this is not feasible. One such application is on chip optical interconnect where there is no control on the polarization state of light. Making the directional coupler polarization independent is essential for these applications [Dokania 2009].

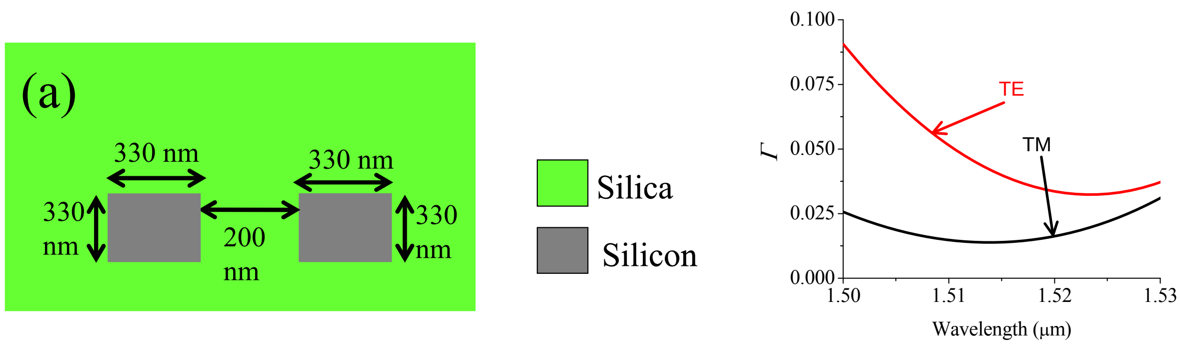

Fig. 5.22. (a) SOI directional coupler (b) Power ratio spectrum for TE and TM and modes.

Although realization of polarization independent SOI waveguides is relatively straight forward [Lim 2007], doing the same for SOI devices such as directional coupler is more challenging; consequently, to date there have been very few reports on polarization independent directional couplers. Polarization independent and wavelength sensitive coupler on SOI using a Mach-Zehnder configuration has been reported [Hsu 2010]. The device is several millimeters long, thereby sacrificing compactness, which is one of the attractive features of silicon nanophotonics. Slot waveguides offer high structural birefringence. Hence by properly choosing the dimensions, it is possible to obtain equal coupling length for both TE and TM modes [Ma 2010]. It is also possible to choose silicon waveguide dimensions carefully to make the directional coupler polarization independent [Passaro 2008]. All these devices are very sensitive to variations of waveguide width and their fabrication will be very challenging.

5.3.2. Design of Polarization Independent Hybrid Plasmonic Directional Coupler

Figure 5.23(a) shows the proposed device. It consists of two identical HPWGs separated by distance D. The power input to the first silicon input waveguide is separated into power P_1 and P_2 among the two output silicon waveguides. As shown in Fig. 5.23(b) each HPWG consists of a silicon slab of dimensions $w \times d$ separated from a silver layer of dimensions $w \times t$ by a silica spacer layer of height h.

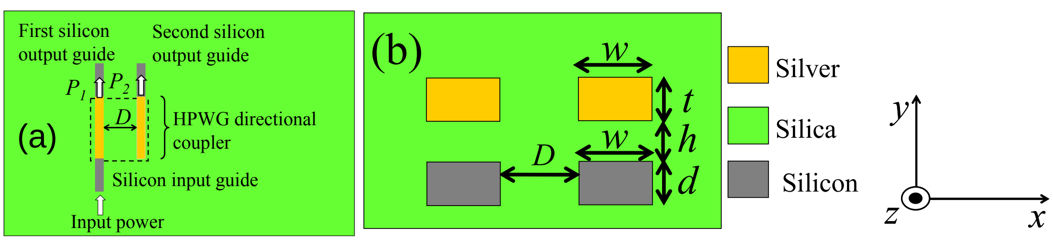

Fig. 5.23. (a) Top view (x-z plane) of the HPWG directional coupler. (b) Cross section (x-y plane) of the HPWG coupler section.

When D is small, modes supported by the two HPWG interact and form supermodes. Fig. 5.24 show the guided power density profiles of HPWG at a transverse plane (x-y plane) calculated using finite element code Femlab. Arrows indicating magnitude and direction of the transverse electric field components are also shown. For the TM supermodes an appreciable amount of power is present in the silica spacer layer, whereas for the TE supermodes power is mostly confined in the silicon slab. Since the fields in the HPWG for the two polarizations are confined in two different layers, changing the waveguide dimensions affect the confinement of the two modes and their interactions differently. By choosing the dimensions properly it is possible to have equal level of coupling and hence equal coupling lengths for both polarizations.

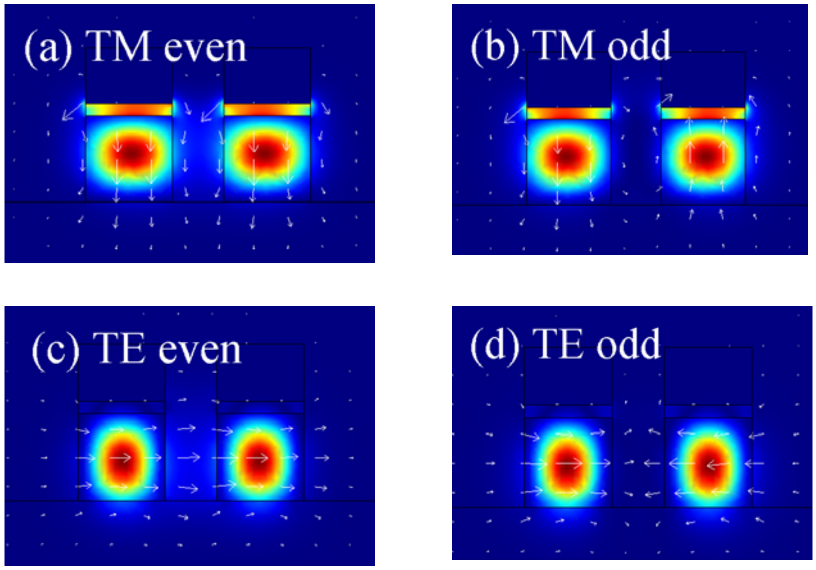

Fig. 5.24. Power density profiles in the hybrid section (x-y plane) for the TM and TE supermodes. Dimensions are w = 330 nm, t = 200 nm, h = 65 nm, d = 330 nm, D = 200nm. Wavelength of operation is 1.55 μm.

Fig. 5.25 shows the effects of varying spacer (silica) and silicon thicknesses (h and d respectively) on coupling lengths for both modes. With increasing silicon thickness (d), both TM and TE modes are more tightly confined and coupling length increases for both modes. In the case of the TE mode, with decreasing spacer thickness (h) the field is pushed out more from the silicon core region and coupling length is reduced. On the other hand, for the TM mode, with decreasing h the mode is more tightly confined in the spacer region (silica) which results in increased coupling length. For h = 65 nm, d = 330 nm the device becomes polarization independent ($L_C^{TM} = L_C^{TE}$ = 8.9 μm).

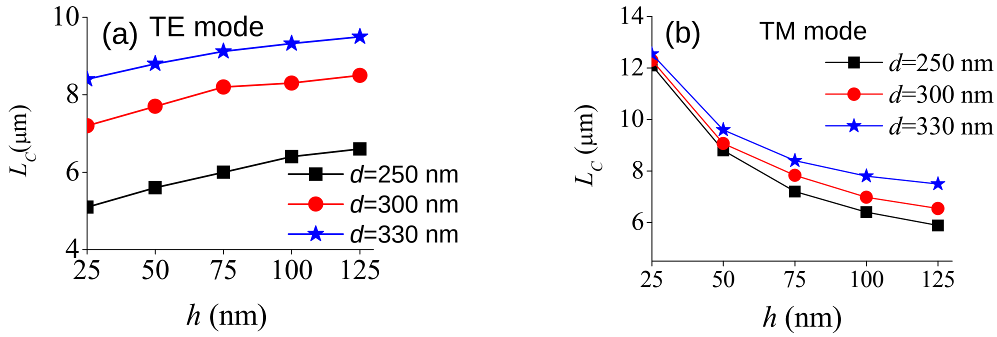

Fig. 5.25. Variations of coupling length (L_C) with silica (h) and silicon (d) thicknesses for (a)TE mode (b)TM mode. Other dimensions are w = 330 nm, t = 200 nm, D = 200 nm. Wavelength of operation is 1.55 μm.

As a design example we analyzed the performance of a polarization independent 3 dB HPWG coupler. The length of the coupler is 4.45 μm. Dimensions of the input/output silicon waveguides cross section (in the x-y plane) are 330nm × 330 nm. We define the fraction of power (η) delivered to the second guide as $\eta = P_2 / (P_1 + P_2)$, where P_1 and P_2 are the power delivered to the first and second output silicon waveguides as shown in Fig. 5.23(a). Fig. 5.26(a) shows η for both TE and TM modes from 1.53 to 1.56 μm, calculated by finite difference time domain code Lumerical. Over this wavelength range η_{TE} and η_{TM} differ by less than 0.5 dB (Fig. 5.20(b)). Because of the short length of the hybrid plasmonic coupler (4.45 μm), the material loss resulting from the presence of metal is small. The insertion losses, (which includes both material loss and coupling loss) for both TE and TM modes are less than 0.5 dB.

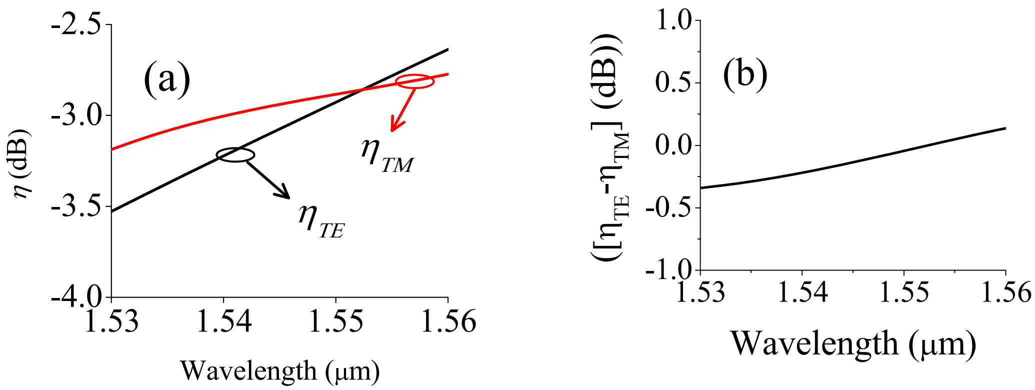

Fig. 5.26. (a) Fraction of the power transferred to the second branch (η). (b) Difference between η_{TE} and η_{TM}. Dimensions are w = 330 nm, t = 200 nm, h = 65 nm, d = 330 nm, D = 200nm.

Fig. 5.27 shows the variation of coupling length of both TE and TM modes with waveguide spacing (D). Although the coupling lengths changes with gap, the device remains polarization independent for a wide range of waveguide spacing.

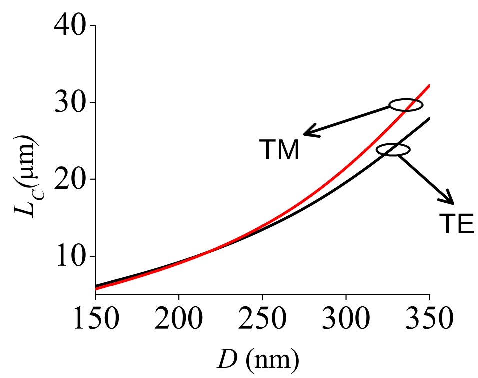

Fig. 5.27. Effect of waveguide spacing on coupling lengths. Other dimensions are w = 330 nm, t = 200 nm, h = 65 nm, d = 330 nm. Wavelength of operation is 1.55 μm.

Realization of the silver sections on the two arms of the coupler will require silver deposition followed by lift off. The silver width can be different than the waveguide width (w) if these steps are not carried out precisely. The resulting structure may look similar to the one shown in Fig. 5.28(a). To determine the effect of such deviations from design values, we investigate two different cases. In case 1 we assume only one of the silver films has a width different than that of the silicon layer ($w = w_1$ and $w_1 \neq w_2$). In case 2, we assume the silver films have equal width but the width is different than that of silicon ($w \neq w_1$ and $w_1 = w_2$). Figures 5.28(a) and (b) show the variations of coupling lengths for TE and TM modes for the two cases. The operation of the device is not significantly affected in either case.

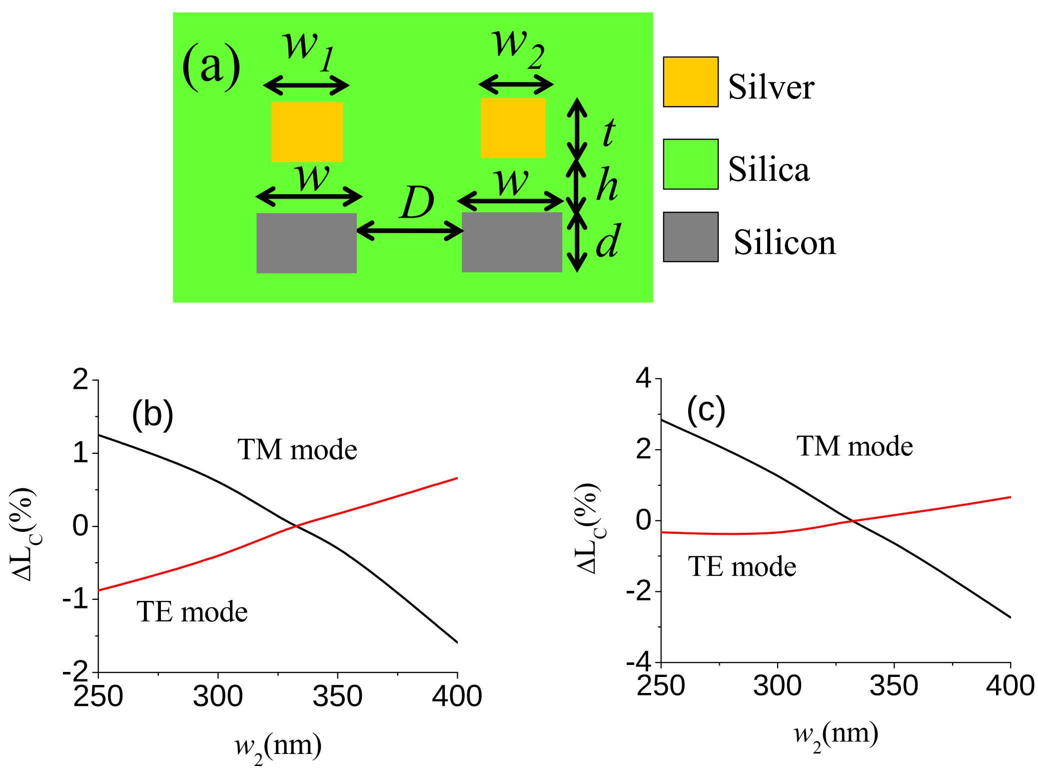

Fig. 5.28. (a) Cross section of hybrid polarizer when metal width is different than silicon width (b) Ratio of coupling lengths for two polarization when $w = w_1$ and $w_1 \neq w_2$. (c) Ratio of coupling lengths for two polarization when $w \neq w_1$ and $w_1 = w_2$.

5.3.3. Comparison with Previously Reported SOI Compatible Polarization Independent Directional Couplers

Polarization independent directional coupler can be designed using slot waveguides [Ma 2010]. Very precise control of the widths of the slots and waveguides will be required to ensure polarization independent operation of the device reported in [Ma 2010]. Also the device requires 20 μm section at either end to achieve good coupling with silicon waveguide. Since the proposed device can be connected directly to silicon waveguides, without the need of any such section, the device length is much shorter than its slot waveguide based counterpart. Polarization independent operation can also be realized by carefully selecting silicon nanowire dimensions [Passaro 2008]. The device is very simple, compact and does not require multiple steps. Though the fabrication requirement is less stringent than that of the slot waveguides coupler, the tolerance is still very small. For example, changing the waveguide width by 12 nm from the specified width (278 nm) i.e., 4.3 % from the design value makes the coupling length of the TE mode 12 % longer than that of the TM mode. The HPWG coupler has a number of more design parameters and offers more flexibility compared to [Passaro 2008]. The first step of implementing the HPWG coupler shown in Fig. 5.17 would be fabrication of silicon sections shown in Fig. 5.17(b). If after fabrication of the silicon waveguide it is found that the widths are different from the specifications, by tuning the spacer height (h) polarization independent operation can still be obtained. For example in the example of previous section if one of the waveguides width is more than the design value of 330 nm by same amount (4.3 %), polarization independence can still be obtained by increasing the silica thickness from 65 nm to 110 nm. Control of film thickness grown by PECVD is much easier than controlling the etch profile. Therefore, although the HPWG coupler requires more process steps than the alternatives, the fabrication process is less demanding. It should be pointed out that the change of both width of waveguide and thickness of spacer results in approximately 11 % change of coupling length for both modes, and hence the power transfer ratio will be changed. Directional couplers are often used for implementing signal taps, where a fraction of the signal power is extracted to monitor signal status. Polarization independent rather than exact power transfer ratio is more important for these applications. Change of coupling to some extent will be acceptable for such devices and HPWG based coupler can be useful for such applications. Finally, polarization independent directional coupler can also be implemented by introducing a bend at one arm of a SOI Mach-Zehnder directional coupler [Hsu 2010]. Though this device provides polarization independence over a broad wavelength range with low insertion losses, its length is several millimeters, in contrast to the 4.45 μm length of the HPWG coupler.

In conclusion the HPWG based polarization independent directional couplers are very compact and their implementation should be less stringent than previously reported designs.

5.4. Hybrid Plasmonic Waveguide Bend

5.4.1. Review of Previous Work on Waveguide Bends

Bends are essential part of almost any integrated optical system. Compared to straight optical waveguide, a waveguide bend suffers from two additional types of losses: the bend loss and the transition loss. When light travels through a bend, to preserve the phase front, the tangential phase velocity has to be proportional to the distance from the center of curvature. If the bend radius is too small, the required phase velocity will be more than that of speed of light. The light in that case is not able to be guided round the bend and is lost due to radiation [Hunsperger 2002]. The mode in the bent section is also shifted laterally compared to the mode in the straight section. Therefore, when light enters a bend from a straight section, it suffers transition loss. Although transition loss can be greatly reduced by offsetting the straight and bent sections, reducing the bend loss is more challenging. This is one of the biggest challenges in realization of compact optical devices and systems. The typical bend radius of low index contrast waveguides can be tens of millimeters. In high contrast waveguides, the mode is more tightly confined and suffers lower bend loss. SOI waveguides provide one of the most compact ways of achieving low loss and compact waveguide bend. For example SOI waveguides can be designed to have less than 1 dB loss for 1.5 μm bend radius. Because the index contrast achievable with naturally occurring material is limited, implementation of very sharp bend with negligible loss has not yet been possible with purely dielectric waveguides.

Because of the different guiding mechanism of plasmonic waveguides, they can guide light through very sharp bends with negligible losses. For example a channel plasmon waveguide can guide light through a sharp 90 degree bend with only 0.13 dB loss. Other types of plasmonic guides, for example slot waveguide [Veronis 2005], metal nano particle array [Brongersma 2000] are also capable of guiding light through sharp bends. Though bend loss for these waveguides can be very low, unfortunately, they suffer large propagation loss because of the presence of metal and also cannot be easily integrated with dielectric waveguides. At alternative guiding mechanism was investigated in [Buckley 2009]. where it was shown that a combination of dielectric wave guiding and parallel plate wave guiding can be used to simultaneously achieve low bend loss and low propagation loss.

5.4.2. Hybrid Plasmonic Waveguide Bend

The goal of our investigation regarding the performance of HPWG bend is two fold: to determine whether it offers any performance benefit compared to previously reported plasmonic waveguides and also whether it performs better than the most compact dielectric waveguides i.e., silicon nanowires. Dielectric loaded plasmon waveguide (DLSPW) proposed in [Steinberger 2008] closely resembles the HPWG shown in Fig. 5.29. Both of them utilize a combination of dielectric and SP wave guiding. Both consist of dielectric film on metal surface. In this section we investigate the performance of a bend consisting of HPWG shown in Fig. 5.29 to find the answers to the questions mentioned at the beginning of this subsection. The major theoretical and experimental works on DLSPW have been carried out at 800 nm wavelength [Steinberger 2008]. For ease of comparison we analyze the performance of the HPWG bend at 0.8 μm.

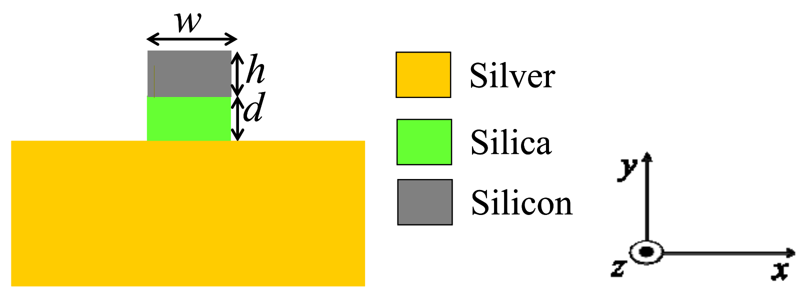

Fig. 5.29. Cross section of the HPWG

In chapter 4 it was shown that HPWG such as the one shown in Fig. 5.29 can provide good mode confinement and moderate propagation loss for the dimensions w = 100 nm, h = 60 nm, d = 100 nm. Fig. 5.30 shows transmission as a function of bend radius using air as the cover material for such a waveguide. Significant power transmission occurs even for sub-micron bend radius. As discussed in Chapter 4, the propagation distance is larger and fabrication process is simpler when the cover region is silica instead of air. However, this increased propagation distance and reduced fabrication complexity come at the cost of diminished mode confinement. Such reduction in confinement may significantly increase the leakage loss especially in case of bends with small bend radii. To investigate the effects of cover layer on bend losses, we show the transmission as a function of bend radii when cover material is silica in Fig. 5.30(b). All other parameters are same as those of Fig. 5.30(a). From the figure it is clear that transmission is much worse when the cover material is silica.

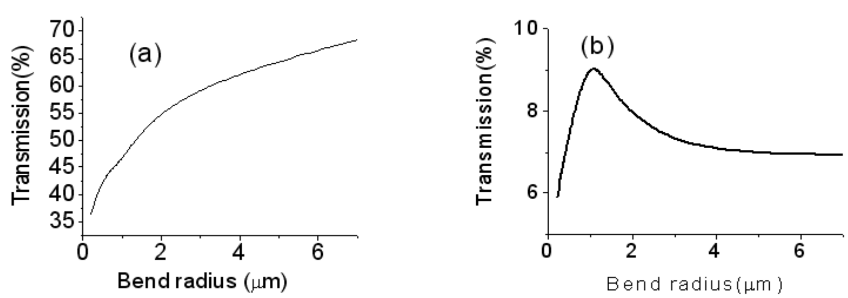

Fig. 5.30. Transmission through 90 degree bends for different bend radii for two different cover materials (a) air (b) silica for the waveguide shown in Fig. 5.29. Spacer medium is silica for both straight and bend sections.

The difference between the transmissions in the two cases is illustrated further in Fig. 5.31(a) and 5.31(b). Here, we have plotted the square of the *y*-component of the electric field ($|E_y|^2$) for a 1.5 μm bend with air [Fig. 5.315(a)] and silica [Fig. 5.31(b)] cover layers. This field quantity is chosen since it is responsible for the power flow and has similar field profile as the guided power. As Fig. 5.31(b) indicates, barely any power is transmitted when silica is the cover material.

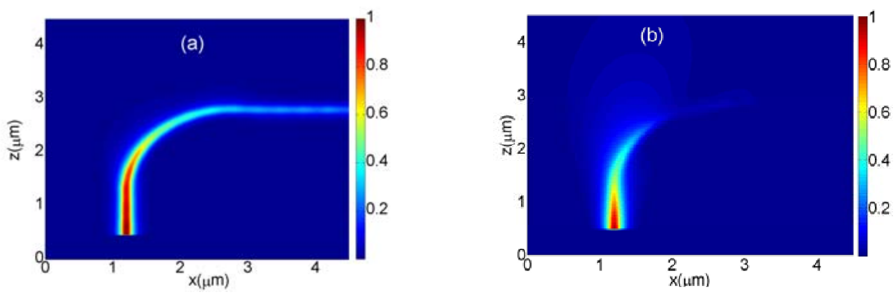

Fig. 5.31. Square of the magnitude of E_y for a 90 degree bend with bend radius 1.5 μm when cover medium is (a) air (b) silica. Spacer layer is silica for both straight and bend sections.

One possible way to do reduce bend loss is to use a spacer layer of higher permittivity to increase confinement and reduce leakage radiation, but this would also increase material loss and hence reduces the propagation distance. For example, if the spacer layer for the straight waveguide is changed from silica to silicon nitride; propagation distance will reduce from 43 μm to 21 μm. A more promising solution would be to use a spacer layer of higher permittivity only in the bend section to reduce bend loss and to use a spacer with lower permittivity in the straight waveguide sections to minimize overall propagation loss. Fig. 5.32 shows the transmission for different bend radii for this scheme. The waveguide structure is same as that of Fig. 5.29 but with silicon nitride (ε_{spacer} = 4) spacer layer in the bend region and silica spacer layer in the straight waveguide section. Transmission is significantly enhanced for both cover material i.e., air and silica.

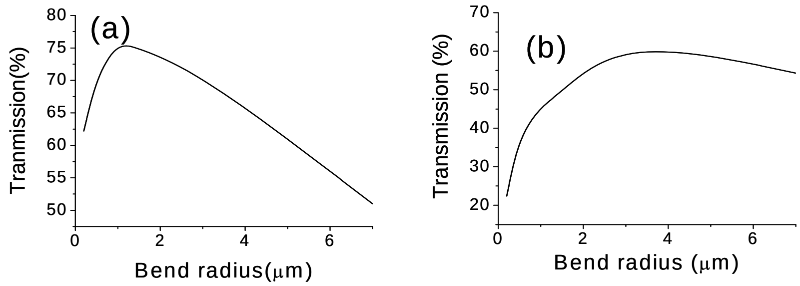

Fig. 5.32. Transmission through 90 degree bend for different bend radii for two different cover materials (a) air (b) silica. Spacer is silicon nitride in bend and silica in straight sections.

The effect of the silicon nitride spacer is further illustrated in Fig. 5.33. The structure is same as that shown in Fig. 5.31 but the spacer layer is now silicon nitride in the bend region. A standing wave is formed in the bend region because of index mismatch between bend and straight section but an improvement in transmission is evident.

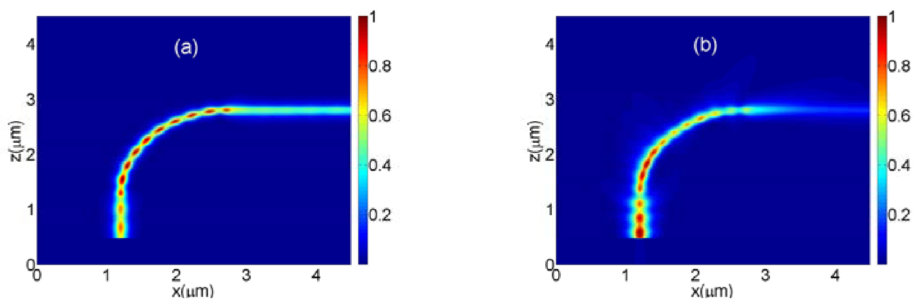

Fig. 5.33. Square of the magnitude of E_y for a 90 degree bend with bend radius of 1.5 μm when cover medium is (a) air (b) silica. Spacer layer is silica nitride in bend and silica is straight sections.

For plasmonic waveguide bend, there is a trade-off between propagation loss and radiation loss. Increase in mode confinement will result in reduced radiation loss. However, as the results of the parametric study in section 2 shows, increase in mode confinement also results in increased propagation loss. Transmission through bend reaches a maximum for an optimum bend radius. Waveguide dimensions, material properties and bend radius should be properly chosen to simultaneously achieve good confinement and high transmission through bends.

5.4.3. Comparison with Previously Reported Waveguide Bends

As seen from previous section in case of HPWG bends, significant transmission occurs even when the bend radius is as small as 1.5 μm. Previous works on DLSPW consisting of a silica ridge on gold substrate reported complete loss of transmission for such bends [Steinberger 2006]. It was also reported that ridge width less than 300 nm fails to confine the SP mode. In case of hybrid waveguide we achieve more than 46 % transmission through a 90 degree bend having bend radius of 1 μm and waveguide width of 100 nm. The results reported here, therefore, indicate a significant improvement in performance. This is not unexpected. Since the proposed structure uses silicon in addition to silica, the guiding capability is expected to be enhanced. The guiding ability of hybrid waveguide bend, however is not very strong compared to that of SOI nanowire bends.

5.5. Discussion

In this chapter we have presented the designs of several HPWG devices for SOI based nanophotonics. We have also compared their performances with previously reported relevant designs. For most of these designs, HPWG devices outperform previously reported devices. The HPWG TM-pass polarizer can provide a lager extinction ratio than silicon nanowire polarizer and its performance is not significantly affected by the change of buried oxide thickness. The HPWG TE-pass polarizer is shortest broadband SOI based polarizer reported to date. The HPWG can also be used to implement couplers which are polarization independent over a broadband wavelength range. All these devices are very compact and despite the lossy nature of the hybrid mode, the insertion loss of these devices is either moderate or very low. To the best of our knowledge, these are the first class of plasmonic devices which provide a combination of compactness, while keeping the overall loss comparable to their dielectric waveguide based counterpart. The extreme confinement of light in the spacer also led us to investigate the possibility of implementing compact waveguide bends based using HPWG. The attempt however was not completely successful. We found that although HPWG bends can outperform some other plasmonic waveguides, it cannot match the performance of SOI waveguide bends. These results may work as useful guideline for future design of HPWG devices.

Although the high concentration in low index medium was not completely successful in implementation of compact bends, there are a number of areas where this property can be very useful. It can be used for achieving enhanced nonlinear effect as discussed in detail in [Zhou 2010]. The combination of guiding in low index medium and polarization diversity can also be very useful for biosensing. This possibility will be explored in detail in next chapter.

Chapter 6

Hybrid Plasmonic Waveguide Biosensor

In the last chapter we have investigated the potential applications of HPWG for integrated optic communication systems. It was shown that the HPWG devices hold great promise for such applications. We now turn our attention to biosensing, one of the most promising areas of plasmonics. Although SP based sensing has already established itself as a successful commercial technology, the information obtained from such sensing is rather limited. For example an SP sensor cannot be used to find both index and thickness of an adlayer (a layer of materials that has been adsorbed on a surface). The combination of high field confinement, lower loss and polarization diversity of HPWG offers the possibility of realizing new types of biosensors which will overcome some of these limitations. In this chapter we investigate these possibilities in detail. In section 6.1 we briefly review various types of biosensors with an emphasis on optical sensing schemes. Because of the relevance of SP sensing for the work under discussion, SP sensors are discussed separately in more detail in section 6.2. We explain the basic principle and various schemes of SP sensing, and summarize the advantages and limitations of SP sensing. The HPWG sensor is introduced in section 6.3; we describe its principle of operation, and also explain how such a sensor can overcome some limitations of SP based sensors. The HPWG sensor can be implemented in many different configurations. In our work we choose to analyze the HPWG sensor in the Mach-Zehnder Interferometer (MZI) configuration. The general principle of a MZI sensor is described and sensor's figures of merit are derived in Section 6.4. This is followed by an investigation of the effects of various parameters on HPWG sensor performance in MZI configuration in section 6.5. The sensor design is optimized for both TE and TM modes in section 6.6. The chapter is concluded with some remarks in Section 6.7.

6.1. Present Status of Optical Biosensing

A biosensor is a device that is composed of a bio-recognition element coupled to a transducer that generates an analytically useful signal to detect the presence and concentration of biological agents of interest. Since the demonstration of the first biosensor by L. C. Clark in 1962, biosensors have been a very active area of research. Today an overwhelming array of biosensors is available for applications ranging from disease diagnosis to analysis of new drugs, agriculture, food safety, environmental analysis and bioterrorism prevention. Figure 6.1 explains the operating principle of a biosensor.

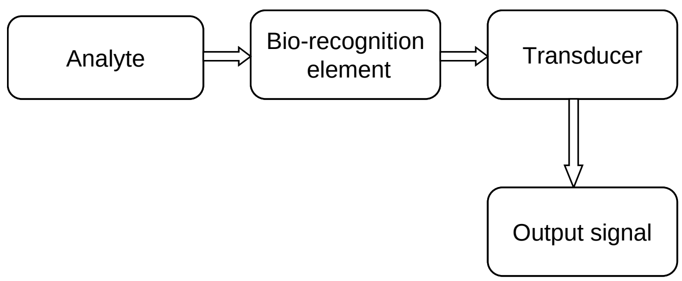

Fig. 6.1. Schematic of a biosensor

Biosensors can be classified depending on the type of bio-recognition element or the transduction mechanism used as shown in Figure 6.2. A detailed review of all types of biosensors is beyond the scope of this work. Instead in this section we very briefly describe various types of biosensors with an emphasis on optical sensors. Many excellent books and review papers are available where more detailed reviews can be found [Marks 2008], [Zourob 2008], [Prasad 2003].

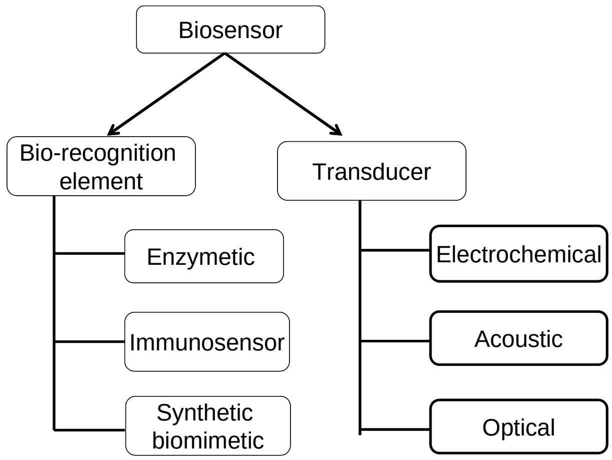

Fig. 6.2. Common types of biosensors

Depending on the biorecognition element biosensors can be classified into three major categories: enzymetic, affinity and synthetic biosensor. Enzymetic sensors use enzymes as the recognition element. This is the major type of sensor used when a suitable enzyme is available and the concentration of the target analyte is in the 10^{-1} to 10^{-7} M range. Blood glucose level monitor, the most widely used biosensor falls into this category. The affinity type biosensors makes use of the high affinity of antibody and antigen and are mostly used for analyte concentration in the range of 10^{-6} to 10^{-10} M. Antibodies are special types of molecules that the body uses for identifying and neutralizing foreign objects (antigens). Affinity type sensors are widely used for medical diagnosis, research on bio-molecular interactions and drug discovery. An alternate and emerging technology is to use synthetic molecules specifically developed for biosensing applications.

Depending on the transduction mechanism used the major types of biosensors are electrochemical, acoustic and optical sensors. Many chemical reactions of interest for biology produce or consume heat, ions or electrons. Electrochemical biosensors work by detecting physical changes of the sample (temperature, resistance etc.) because of these chemical reactions. These sensors are cheap, disposable and reproducible but their detection limit is relatively high i.e., they are not suitable for detection of low analyte concentrations. Acoustics waves i.e., oscillations that propagate through a solid as a time dependent mechanical deformation can also be used for biosensing. The most notable example of acoustic sensors is a quartz crystal microbalance (QCM). Development of acoustic sensors has been slow until recently. However, there is a renewed interest in acoustic sensors at present and there is a possibility that these sensors will find wider applications in the near future.

Optical sensors use changes of light properties (intensity, phase or polarizations state) for detection of species of interests. Optical sensors stand apart from other methods for a number of unique features. They are highly sensitive: even single molecule detection is possible with some optical techniques. They are free from electromagnetic interference. Optical sensors can be easily multiplexed. For example, fluorescence microarrays consisting of thousands of sensing elements are widely used in DNA analysis. Because of these attractive features, optical sensing has already established itself as one of the dominant sensing technologies in medical diagnosis, drug discovery and biological research.

Optical biosensors can be classified into two major categories: labeled (fluorescence) and label free sensors. In fluorescence spectroscopy either the target molecules or the molecules of interest are tagged with fluorescent molecules. The sample is then illuminated with either visible or ultra violet light. The molecules absorb the light and are excited to high energy states from where they can move to various lower energy states. The resonance life time of the decay and hence the emission spectrum will dictate the presence of target molecules. The instrument used for these analyses are relatively inexpensive and can be readily incorporated with other techniques e.g., confocal microscope and spectrometers. The labeling molecules can interfere with the function of biomolecules. In addition obtaining quantitative information from fluorescence can be challenging. Despite its limitations, fluorescence spectroscopy remains one of the most widely used analytical techniques in biology and medicine.

Label free biosensing offers an attractive alternative to the above mentioned technique. These techniques detect the presence of target molecules in a sample by measuring the changes of refractive index caused by their presence. This makes it possible to detect the biomolecules in their natural forms, even when their concentration is very low. Many different label free optical sensing schemes have been proposed by various researchers and many of them have been commercialized. Here we will discuss only three examples of label free sensing: Raman spectroscopy, dual polarization spectroscopy and surface plasmon resonance. More details on different types of label free optical sensing schemes can be found in [Daghestani 2010, Marks 2008, Fan 2008].

When light interacts with a molecule, some of the energy of the light can be transferred to the vibrational and rotational modes of the molecule. As a result the energy of the scattered light is different (usually lower) than that of the incident light by the energy difference between the initial and final vibrational states- a phenomenon known as Raman scattering. The Raman spectra of a molecule have sharp and distinct peaks and hence Raman Spectroscopy is very suitable for accurate and reliable detection of molecules from a complex mixture, for example blood serum. However, only 1 in approximately 10^7 photon participates in Raman scattering and hence the Raman signal is very weak. Detecting such a signal unambiguously is a challenging task. One possibility of enhancing the Raman signal is surface enhanced Raman scattering (SERS). The enhanced electric field intensity resulting from the excitation of localized surface plasmon on rough metal surface and on nano particle surface can be used to enhance Raman scattering up to 10^{10} to 10^{11}. SERS is one of the few techniques which are capable of single molecule detection [Barnes 2003].

The dual polarization interferometer (DPI) consists of two waveguides stacked on each other. The bottom waveguide acts as the reference guide, and the top one acts as the sensing guide. Light supported by the two guides radiates in free space at the end facet and form interference fringes on a CCD array. The adhesion of molecules of interest on the sensing waveguide results in change of optical path length, which can be determined from the shift of the fringes. The sensitivity of DPI is high and since this device can carry out measurements for both TE and TM polarizations, the thickness and refractive index of the adlayer can be determined in a straight forward manner [Dejardin 2006]. Since the DPI consists of only dielectric materials and functionalization of dielectric surfaces with bio-recognition molecules is challenging, DPI is not suitable for sensing all biomolecules. Also DPI averages the adlayer property over a large sensing area, and is not very suitable for examining chemical kinetics.

Surface plasmon resonance spectroscopy is one of the most popular label free biosensing methods currently in use. Since SP based sensing is very relevant for this present work, we examine it in more detail in the next section.

6.2. Surface plasmon based biosensing

SPs are highly localized to a metal surface and hence can be very sensitive to the index change on the surface. This property can be used to implement highly sensitive biosensors. Figure 6.3 shows a typical set up for SP based sensor. A binding antibody is immobilized on a gold surface and a biological sample, e.g., blood serum is passed over the surface. If the molecule to be detected (antigen) is present, it will be attached to the antibodies on the functionalized surface and cause a change in the effective index of the SP mode, which in turn changes the position of the dip in reflection in an attenuated total reflection (ATR) measurement, as shown in Fig. 6.3(b).

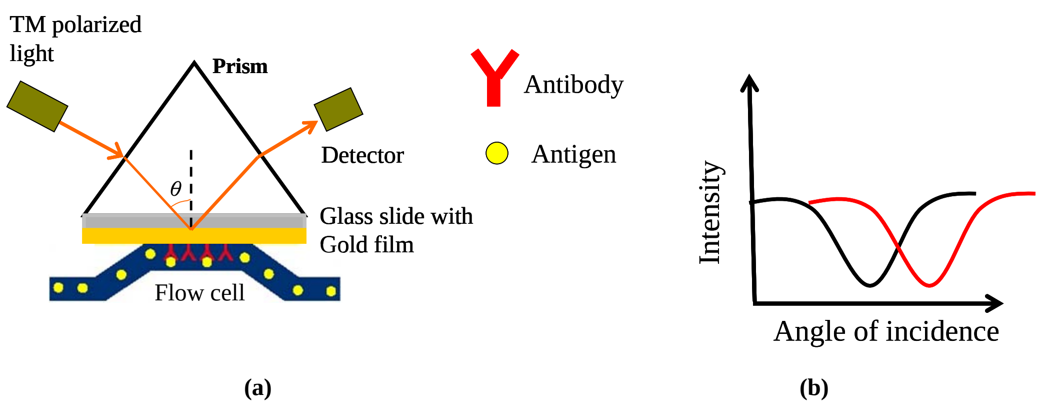

Fig. 6.3. (a) Typical set up for a surface plasmon resonance biosensor (b) Reflection spectrum of the biosensor, where the black line is a reference spectrum, and the red line shows a shifted spectrum. The shift happens due to the attached antigens.

Prism coupling based SP sensors use very simple optical instruments and the measurement is straightforward. Almost all currently available commercial SP sensors use prism coupling. These sensors are bulky; requires large space and usually are not suitable for use outside a laboratory environment. With a goal to miniaturize SP sensor and making it useful for a wider range of applications many other SP sensing configurations have been investigated, for example grating and fiber based and planar SP sensors. Grating based SP sensors are compact, light weight and low cost. The sensitivity of such a sensor is low and more work is necessary before they can compete with the performance of prism based sensors. Fiber based SP sensors are very compact, have very flexible geometry and can be used for remote detection and sensing. The major limitation of the fiber sensors is the effect of fiber deformation on the coupling of the SP and waveguide modes. Planar sensors are superior to optical fiber sensors in a number of ways. They are more robust, offer easier and more precise deposition of various reagents and are especially suitable for implementing many different sensing channels on one platform. Waveguide based SP sensors depend on resonant coupling of the waveguide mode with the SP mode on a gold surface. Many different types of integrated optic SP sensors have been proposed including sensor using buffer layer [Lavers 1994], high index overlayer [Ctyroky 1997] or using of photonic crystals [Skorobogatiy 2006]. Although planar SP sensors are not yet commercially available, with the rapid progress made in last few years the scenario is expected to change in near future.

SP sensors offer a number of advantages.

1) They offer label free detection.

2) They are highly sensitive.

3) The gold surface can be easily functionalized by thiol chemistry for detecting a wide variety of molecules.

Because of these advantages SP based sensing has become one of the most successful affinity sensing scheme proposed to date. However it also has a few significant limitations.

1) Although SP is a surface mode, the field of an SP mode extends a few hundred nanometers into the dielectric and its characteristics are affected by both changes in surface and bulk properties. Typical SP sensing scheme uses only wavelength or angular interrogation schemes and cannot differentiate between bulk and surface changes. This may be problematic for many practical cases. Some examples are given below.

1.a) Blood serum proteomics: Concentrations of certain biomarkers (protein, DNA or RNA) change at the very early stage of cancer. Detecting their presence and measuring their concentrations will lead to early diagnosis. Success of this scheme will require detection of extremely small amounts of the various biomarkers from a complex, small volume sample. However, blood serum is a very complex mixture containing many kinds of proteins, DNAs and RNAs whose concentration may differ by many orders of magnitude. To illustrate this we have plotted the concentrations of some common blood serum proteins in Fig. 6.4 [Anderson 2002]. As can be seen from the plot concentrations of interleukins (a group of protein molecules secreted by various cells), some of which are important biomarkers can be eight to ten orders of magnitude lower than more abundant plasma proteins e.g., hemoglobin and albumin. In addition the concentrations of proteins like hemoglobin and albumin may change from one person to another and even for the same person from one day to another. Since SP based sensor cannot differentiate between change of bulk index and change of adlayer thickness, even if the sensor surface is functionalized for detection of interleukins, their presence may be completely overshadowed by change of bulk index caused by variation of concentrations of more abundant plasma proteins. SP based sensing therefore is not suitable for these types of sensing.

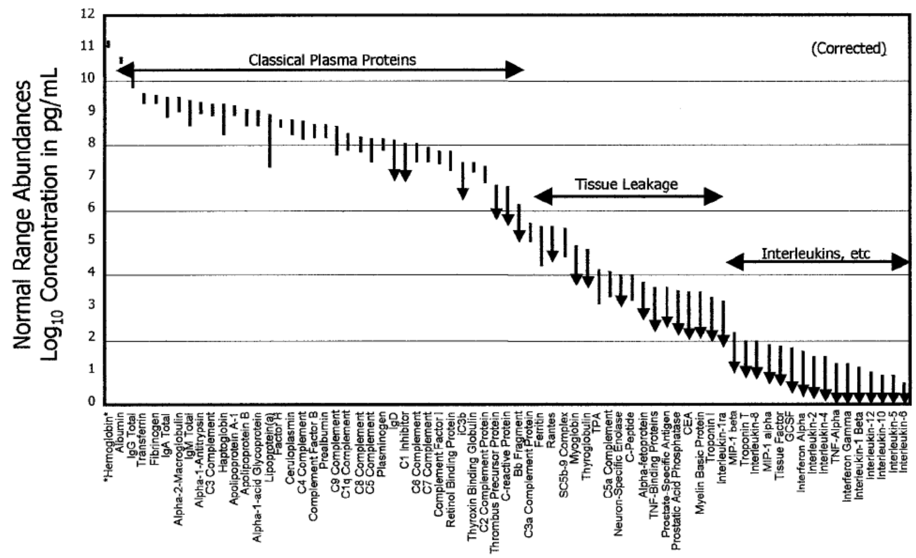

Fig. 6.4. Reference intervals for 70 protein analytes in plasma [Anderson 2002]

1.b) Effect of temperature variation: SP sensors are often used to detect very low concentration of analytes. An index change on the order of 10^{-6} is typical for conventional SP sensors. Since the change of index of aqueous solutions are of the order of 1×10^{-4} $°C^{-1}$, very strict control of temperature is necessary for such instruments. The problem is particularly severe, when the sensor is exposed to laser irradiation for long period of time [Xiao 2010]. Since the adlayer has a large thermal conductivity and is in contact with gold, its temperature and hence index changes little under such condition. However, the index of the solution may change enough to influence the measurement results. A reference channel is usually used to circumvent such problems but they are not effective enough for many highly demanding cases [Naimushin 2003].

2) In SP sensing usually the index of the adlayer is assumed to be known and the thickness is determined from measurements. This is not a good assumption in many cases [Nellen 1988], [Nellen 1993].

3) There are many biological process of interest which results in little or no change of mass of adlayer on the surface. For example the conformational changes of proteins (folding and unfolding) are very important information to gain insight into a protein's structure and functionalities but these processes are usually either zero or low mass signature event. SP is not suitable for the investigation of such changes. Lipid is another class of anisotropic molecules which are of great interest for biology and drug industry. Their anisotropic nature cannot be investigated using SP.

In summary, although SP is a very successful sensing technology, the information obtained from SP sensing is rather limited. A sensing technology that can retain the sensitivity and ease of surface functionalization of SP while offering the ability to obtain additional information will greatly extend the scope of plasmonic sensing.

6.3. Introduction to Hybrid Plasmonic Waveguide Biosensor

The geometry of the one dimensional HPWG is shown in Fig. 6.5 (a). It consists of a gold surface separated from a high index region (silicon or silicon nitride) by a nano-fluidic channel. The cladding is silica. The structure is similar to HPWG described in Chapter 3 with the exception that the silica spacer is replaced with a nano-fluidic channel containing a biological sample of interest. As shown in Fig. 6.5(b), for the hybrid TM mode a significant amount of power is concentrated in the nano-fluidic channel. As a result the hybrid mode is expected to be more sensitive than single interface SP. In addition to supporting TM type hybrid mode, the silicon slab which is a part of the hybrid waveguide also supports a conventional TE type dielectric waveguide mode, as shown in Fig. 6.5(c). Although the TE mode is concentrated in silicon, part of the evanescent mode will also be in the nano-fluidic channel. Therefore, the TE mode supported by HPWG can also be used for sensing.

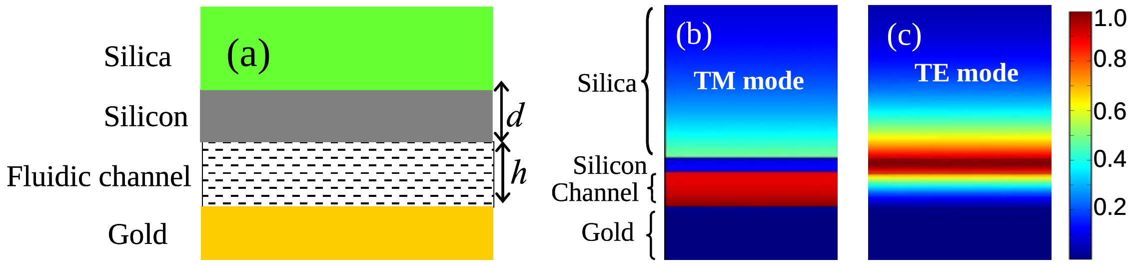

Fig. 6.5. (a) Schematic of hybrid waveguide biosensor. Guided power densities for (b) TM mode (c) TE mode for h = 100 nm, d = 50 nm. Wavelength of operation is 1.55 μm.

In the following we will explain how the polarization diversity of HPWG can be used for overcoming the limitations of SP sensors. The following notations will be used throughout this discussion.

$\gamma = \beta + j\alpha$; γ is the propagation constant of the guided mode, α and β are the attenuation and phase constants respectively

$N_{eff} = \gamma / \beta_0 = n_{eff} + jk_{eff}$; N_{eff} is the effective mode index; β_0 is free space wave number given by $\beta_0 = 2\pi / \lambda_0$.

a = adlayer thickness

n_c = refractive index of bulk sample

$\dfrac{\partial n_{eff}}{\partial a}$ = surface sensitivity

$\dfrac{\partial n_{eff}}{\partial n_c}$ = bulk sensitivity

The nature of the mode (TE or TM) will be mentioned with the symbol where there is a risk of ambiguity. For example, $n_{eff}\,(TM_0)$ will mean the real part of effective mode index of the TM_0 mode and $\frac{\partial n_{eff}}{\partial a}(TE_0)$ would mean the surface sensitivity of the TE_0 mode.

The HPWG sensor can potentially overcome the limitations of the SP sensor in following ways.

1) Since the TM mode is highly concentrated in the nano-fluidic channel the HPWG can offer higher sensitivity compared to plasmonic sensors.
2) Since HPWG can support both TM and TE modes, the contributions from bulk and surface sensitivities can be separated by a procedure similar to that proposed in [Tiefenthaler 1989]. The variation of bulk index of the fluid (Δn_c) and the variation of thickness of adlayer (Δa) are related to the change of effective index for the fundamental TE mode $\Delta N(TE_0)$ and for the fundamental TM mode $\Delta N(TM_0)$ as

$$\Delta N(TE_0) = \frac{\partial n_{eff}}{\partial n_c}(TE_0)\Delta n_c + \frac{\partial n_{eff}}{\partial a}(TE_0)\Delta a \tag{6.1}$$

$$\Delta N(TM_0) = \frac{\partial n_{eff}}{\partial n_c}(TM_0)\Delta n_c + \frac{\partial n_{eff}}{\partial a}(TM_0)\Delta a \tag{6.2}$$

Reorganizing (6.1) and (6.2) we get

$$\Delta n_c = \frac{1}{\frac{\partial n_{eff}}{\partial n_c}(TE_0)\frac{\partial n_{eff}}{\partial a}(TM_0) - \frac{\partial n_{eff}}{\partial a}(TE_0)\frac{\partial n_{eff}}{\partial n_c}(TM_0)}\left[\frac{\partial n_{eff}}{\partial a}(TM_0)\Delta N(TE_0) - \frac{\partial n_{eff}}{\partial a}(TE_0)\Delta N(TM_0)\right] \tag{6.3}$$

$$\Delta a = \frac{1}{\frac{\partial n_{eff}}{\partial n_c}(TE_0)\frac{\partial n_{eff}}{\partial a}(TM_0) - \frac{\partial n_{eff}}{\partial a}(TE_0)\frac{\partial n_{eff}}{\partial n_c}(TM_0)}\left[-\frac{\partial n_{eff}}{\partial n_c}(TM_0)\Delta N(TE_0) + \frac{\partial n_{eff}}{\partial n_c}(TE_0)\Delta N(TM_0)\right] \tag{6.4}$$

As explained in [Tiefenthaler 1989] (6.3) and (6.4) are applicable provided that determinant of sensitivity matrix S is nonzero.

$$S = \begin{bmatrix} \frac{\partial n_{eff}}{\partial n_c}(TE_0) & \frac{\partial n_{eff}}{\partial a}(TE_0) \\ \frac{\partial n_{eff}}{\partial n_c}(TM_0) & \frac{\partial n_{eff}}{\partial a}(TM_0) \end{bmatrix} \qquad (6.5)$$

Once $\Delta N(TE_0)$ and $\Delta N(TM_0)$ are known from measurements, Δn_c and Δa can be determined from equations (6.1) and (6.2).

3) Carrying out a procedure similar to the one described above, it is also possible to determine both adlayer index and thickness [Nellen 1993] when the bulk index is known.

4) Because of the polarization diversity, the hybrid sensor in addition to providing high sensitivity can also be used to find additional structural information about complex molecules, similar to dual polarization interferometer.

6.4. Hybrid Biosensor in Mach-Zehnder Configuration: Figures of Merit

The hybrid waveguide biosensor can be implemented in many different configurations; for example using a Mach-Zehnder interferometer (MZI), prism coupling or by using a grating. MZI sensors are highly sensitive, simple to fabricate and compatible with planar technology. Therefore, we choose to investigate the hybrid MZI sensor in this work. Fig. 6.6 (a) shows the schematic of a general MZI type biosensor. It consists of a sensing arm which is typically coated with binding molecules and a reference arm which is coated with some material that inhibits absorption on the surface. A fraction (typically 50%) of the input power (P_{in}) propagates through the sensing arm and another fraction propagates through the reference arm and they combine at the sensor output. A biological sample is allowed to flow over both sensing and reference arm. If the molecules of interest are present, they will attach themselves only to the sensing arm and result in a phase difference between the lights coming out of the two arms. The output light amplitude thus varies with adlayer thickness as shown schematically in Fig. 6.6(b). By examining the output power, the presence of a molecule of interest and its concentration can be determined.

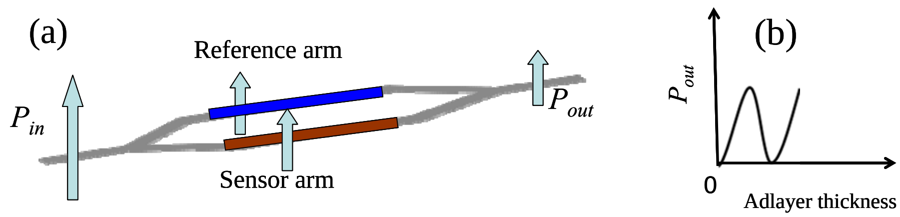

Fig. 6.6. (a) Schematic of a MZI biosensor (b) Variation of output power of the MZI biosensor with adlayer thickness.

A few comments about the criterion of a good biosensor are relevant before we embark on a detailed analysis of the hybrid sensor. A significant number of previous investigations on plasmonic sensors reported in literature considered bulk sensitivity (change of effective mode index for unit change of bulk index) as the key measure of sensor performance. They assumed larger bulk sensitivity is an indication of a good biosensor. Although this is true for a bulk sensor, most biosensors are affinity type and large bulk sensitivity is in fact undesirable in such cases. It is also a common practice to use surface sensitivity (change of effective mode index for unit change of adlayer thickness) as the sensor figure of merit. Although surface sensitivity is a very important parameter for an affinity sensor, a larger surface sensitivity does not necessarily mean a smaller limit of detection (LoD). Berini has discussed this issue in detail and showed that LoD depends on both sensitivity and propagation loss of the guided mode [Berini 2008]. He defined two quantities: figure of merit for surface sensing (*G*) and figure of merit for bulk sensing (*H*). He also showed that LoD for bulk and surface sensing are inversely proportional to *G* and *H* respectively. In our work we used these figures of merit instead of using bulk and surface sensitivity as the criterion of a good biosensor. Unfortunately the expressions for *G* and *H* defined by Berini are usable only when the length of sensor section equals that of the propagation distance of the guided mode. As we will see later in this chapter, satisfying this condition will be difficult for a HPWG sensor designed to use both polarizations. Therefore, we need to derive expressions for figures of merit for a sensor of arbitrary length. In the following we briefly summarize the procedure Berini used in [Berini 2008] to derive the figures of merit (G and H) and then extend it to the case of sensor of arbitrary length.

6.4.1. Figure of Merit for Optimized Sensor Length

In this subsection we briefly outline the method Berini used to derive the figures of merit for biosensors in MZI configuration. We follow the notations described in Section 6.3. Assuming φ_D is the difference in phase accumulated by light in the sensing and reference arm of the MZI sensor shown in Fig. 6.6(a), the output power is given by

$$P_{out} = P_{in} e^{-2\alpha(L_0+L)} \frac{1}{2}(1+\cos\varphi_D) \tag{6.3}$$

Here L is the length of the sensing region and L_0 is the length needed for the input and output access lines, φ_D is the insertion phase between the sensing arm and the reference arm. The phase sensitivity of the sensor ($\partial P_{out} / \partial \varphi_D$) is given by

$$\frac{\partial P_{out}}{\partial \varphi_D} = -P_{in} \frac{1}{2} e^{-2\alpha(L_0+L)} \sin\varphi_D \tag{6.4}$$

If the effective mode index of light in the sensing and reference arms are n_{eff} and $n_{eff,r}$ respectively, φ_D is given by

$$\varphi_D = \frac{2\pi L}{\lambda_0}(n_{eff} - n_{eff,r}) \tag{6.5}$$

For a MZI sensor, the most important criterion is sensitivity defined as $\partial P_{out} / \partial a$ i.e., the change of output power as a function of adlayer thickness. Using (6.4) and (6.5) the expression for this is

$$\frac{\partial P_{out}}{\partial a} = \frac{\partial P_{out}}{\partial \varphi_D}\frac{\partial \varphi_D}{\partial a} = -P_{in}\frac{1}{2}e^{-2\alpha(L_0+L)}\sin\varphi_D\;\frac{2\pi L}{\lambda_0}\frac{\partial n_{eff}}{\partial a} \tag{6.6}$$

In case of a lossy MZI sensor, the length L needs to be carefully chosen to maximize sensitivity. The maximum sensitivity is achieved when L = 1/2α i.e., the length of the sensing region equals the propagation distance of the mode [Berini 2008]. The corresponding sensitivity is

$$(\frac{\partial P_{out}}{\partial a})_{L=L_{prop}} = -P_{in}\frac{1}{4}e^{-(1+2\alpha L_0)}\sin\varphi_D\,\frac{2\pi}{\lambda_0}\frac{1}{\alpha}\frac{\partial n_{eff}}{\partial a} \tag{6.7}$$

Defining

$$G = \frac{2\pi}{\lambda_0}\frac{1}{\alpha}\frac{\partial n_{eff}}{\partial a} = \frac{\beta_0}{\alpha}\frac{\partial n_{eff}}{\partial a} = \frac{\frac{\partial n_{eff}}{\partial a}}{k_{eff}} \tag{6.8}$$

(6.7) can be rewritten as

$$(\frac{\partial P_{out}}{\partial a})_{L=L_{\Pr op}} = -\frac{1}{4}P_{in}e^{-(1+2\alpha L_0)}\sin(\varphi_D)G \tag{6.9}$$

The value of L_0 will depend on the specific design and it is difficult to assume a value of L_0 which will be applicable in all cases. If we make the following assumption similar to [Berini 2008]

$$L_0 = L_{prop} \tag{6.10}$$

We can rewrite (6.9) as

$$(\frac{\partial P_{out}}{\partial a})_{L=L_{\Pr op}} = -\frac{1}{4}P_{in}e^{-2}\sin(\varphi_D)G \tag{6.11}$$

From (6.11) we see that the sensitivity ($\partial P_{out} / \partial a$) can be maximized by maximizing *G*. The factor *G* lumps into a single parameter the effects of material properties and wavelength of operation on sensitivity of the sensor. Therefore, *G* is the *combined sensitivity factor for surface sensing*. The best affinity sensor will be one that has maximum G.

The adlayer thickness detected by an affinity sensor can be translated into surface mass coverage (Γ) by the following relation [Feijter 1978].

$$\Gamma = \frac{a(n_a - n_c)}{\partial n / \partial c} \tag{6.12}$$

Here n_a and n_c are index of adlayer and bulk sample respectively and $\partial n/\partial c$ are change of index with analyte concentration. The minimum detectable change in surface coverage ($\Delta\Gamma_{min}$) is related to corresponding change in adlayer thickness (Δa_{min}) by

$$\Delta\Gamma_{min} = \frac{(n_a - n_c)}{\partial n / \partial c} \Delta a_{min} \tag{6.13}$$

Change of output power (ΔP_{out}) is related to Δa by the following relation

$$\Delta P_{out} = \frac{\partial P_{out}}{\partial a} \Delta a \tag{6.14}$$

From (6.14) it follows that the minimum detectable change of output power ($\Delta P_{out,min}$) is related to the corresponding change in adlayer thickness (Δa_{min}) by the following

$$\Delta P_{out,\min} = \frac{\partial P_{out}}{\partial a} \Delta a_{\min} \tag{6.15}$$

Putting the expression of Δa_{min} obtained from (6.15) into (6.13) and using (6.11) we see the limit of detection for surface sensing i.e., minimum surface mass coverage Γ_{min} is related to *G* by the following relation.

$$\Delta\Gamma_{\min} = \frac{(n_a - n_c)}{\partial n / \partial c} \frac{1}{(\partial P_{out} / \partial a)_{L=L_{\Pr op}}} \Delta P_{out,\min} = \frac{(n_a - n_c)}{\partial n / \partial c} \frac{1}{-\frac{1}{4} P_{in} e^{-2} \sin(\varphi_D) G} \Delta P_{out,\min} \tag{6.16}$$

From (6.16), we see that minimum detection limit is inversely proportional to *G*. In addition to change of adlayer thickness or index, the MZI sensor is also sensitive to change in index of fluid (n_c). Berini defined a sensor figure of merit for bulk sensing which he denoted as *H* and has the following form.

$$H = \frac{2\pi}{\lambda_0} \frac{1}{\alpha} \frac{\partial n_{eff}}{\partial n_c} = \frac{\beta_0}{\alpha} \frac{\partial n_{eff}}{\partial n_c} = \frac{\frac{\partial n_{eff}}{\partial n_c}}{k_{eff}} \tag{6.17}$$

Berini showed that the limit of detection for bulk sensing is inversely proportional to *H*.

6.4.2. Figure of Merit for Sensor of Arbitrary Length

As seen from (6.11) and (6.16) G provides a direct measure of minimum detection limit only when equation (6.10) is satisfied. In many practical situations this may not be possible. For example, we may not be able to satisfy (6.10) simultaneously for both TE and TM modes for a HPWG sensor. We therefore, examine the sensitivity of a MZI sensor for which $L \neq L_{prop}$. Let the length of sensor be $L = x \times L_{prop}$. Following (6.6) the sensitivity in this case is

$$\left(\frac{\partial P_{out}}{\partial a}\right)_{L=xL_{\Pr op}} = -P_{in} \frac{1}{2} e^{-2\alpha(L_0 + xL_{prop})} \sin\varphi_D \frac{2\pi(x \times L_{prop})}{\lambda_0} \frac{\partial n_{eff}}{\partial a} \tag{6.18}$$

In case of $L = L_{prop}$ the sensitivity is

$$\left(\frac{\partial P_{out}}{\partial a}\right)_{L=L_{Prop}} = -P_{in}\frac{1}{2}e^{-2\alpha(L_0+L_{prop})}\sin\varphi_D \frac{2\pi L_{Prop}}{\lambda_0}\frac{\partial n_{eff}}{\partial a} \tag{6.19}$$

Dividing (6.18) by (6.19) we get

$$\frac{\left(\frac{\partial P_{out}}{\partial a}\right)_{L=xL_{Prop}}}{\left(\frac{\partial P_{out}}{\partial a}\right)_{L=L_{Prop}}} = \frac{x}{e^{2\alpha L_{prop}(x-1)}} \tag{6.20}$$

Utilizing the fact that $L_{prop} = 1/2\alpha$ we get

$$\left(\frac{\partial P_{out}}{\partial a}\right)_{L=xL_{Prop}} = \frac{x}{e^{(x-1)}} \times \left(\frac{\partial P_{out}}{\partial a}\right)_{L=L_{Prop}} \tag{6.21}$$

From (6.13) , (6.15) and (6.21) we can write

$$\Delta\Gamma_{\min} = \frac{(n_a-n_c)}{\partial n/\partial c}\frac{1}{(\partial P_{out}/\partial a)_{L=xL_{prop}}}\Delta P_{out,\min} = \frac{(n_a-n_c)}{\partial n/\partial c}\frac{1}{-\frac{1}{4}P_{in}e^{-2}\sin(\varphi_D)G\times\frac{x}{e^{(x-1)}}}\Delta P_{out,\min} \tag{6.22}$$

Comparing (6.16) and (6.22) we see that the expressions of detection limit (Γ_{min}) are very similar to both cases. The only difference is the presence of the factor $\frac{x}{e^{(x-1)}}$ in the denominator for the latter case. Therefore we define the effective sensitivity factor G_{eff} for a sensor of arbitrary length as

$$G_{eff} = \frac{x}{e^{(x-1)}} \times G \tag{6.23}$$

G_{eff} has an interpretation similar to G but is valid for any sensor length i.e., the limit of detection for surface sensing for a sensor of arbitrary length is inversely proportional to G_{eff}.

6.5. Analysis of One Dimensional Hybrid Plasmonic Sensor: Effects of Various Parameters

In this section we investigate the effects of channel and high index medium thickness and wavelength on sensor performance. We study the one dimensional guide shown in Fig.6.5(a) since it can be handled analytically and accurate solutions for the guided modes can be obtained with little numerical effort. Also its characteristics e.g., field profile, sensitivity etc. closely resembles those of the more realistic two dimensional structure. Permittivity of silica and silicon are taken from [Palik 1985]. Although we have used permittivity value of gold from [Johnson 1972] for most part of our work, here we use the values from [Palik 1985]. This allows us to compare the performance of the hybrid sensor with that of the other types of plasmonic sensors reported in previous works [Berini 2008]. Most biological samples are aqueous in nature with large water content. Therefore we consider the index of the sample filling the nano-fluidic channel to be same as water. The material loss data of water is taken into account [Kou 1993]. Spine interpolation is used to obtain all the material data at the wavelengths of interest. The adlayer is assumed to be a homogenous, isotropic and uniform dielectric material. Following earlier works we assume a wavelength independent relative permittivity 1.5 for the adlayer.

Since the structure considered in this work is one dimensional, accurate solutions for the guided modes can be obtained by direct application of Maxwell's equations and proper boundary conditions. We use the transfer matrix method for this purpose in our work. Surface and bulk sensitivities are calculated using the central-difference formulae.

$$\frac{\partial n_{eff}}{\partial a} = \frac{n_{eff}(a+\Delta a) - n_{eff}(a-\Delta a)}{2\Delta a} \tag{6.20}$$

$$\frac{\partial n_{eff}}{\partial n_c} = \frac{n_{eff}(n_c + \Delta n_c) - n_{eff}(n_c - \Delta n_c)}{2\Delta n_c} \quad (6.21)$$

Here a and n_c are the initial adlayer thickness and index of the bulk and h and h_c are the changes in these two quantities. Similar to [Berini 2008] we assume a = 3 nm, Δa = 0.1 nm, n_c = 1.5 and Δn_c = 1e-3.

Figure 6.8 shows the variations of sensor characteristics as a function of wavelength for three different silicon thicknesses (d = 70 nm, 100 nm, 140 nm). The sensor is multimode for d = 100 nm and d = 140 nm but to keep the plots less crowded, the higher order modes for d = 100 nm and d = 140 nm are not plotted in Fig. 6.8. For all cases with increasing wavelength, the mode spreads out more from the silicon, which results in reduction of effective mode index as shown in Fig. 6.8(a). Variations of the other parameters are more complicated. As shown in Fig. 6.8(b), the propagation loss reduces monotonously for two cases (d = 70 nm, 100 nm) but reaches a minimum around 1 μm wavelength for d = 140 nm. The variations of surface sensitivity are also different in three cases. For the first case (d = 70 nm), it decreases monotonously with increasing wavelength. In the second case, surface sensitivity reaches a maximum around the wavelength of 1.05 μm. In the third case (d = 140 nm), unlike case 1 (d = 70 nm), surface sensitivity always increases with increasing wavelength. As shown in Fig. 6.8(d), the combined surface sensitivity factor (G) in all cases is maximized for specific wavelengths, though the position of the maximum is different for the three cases.

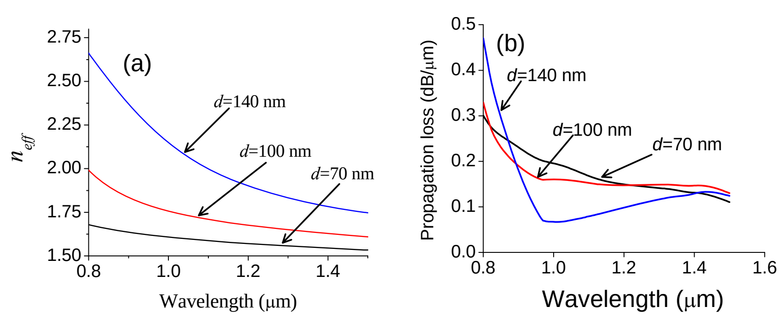

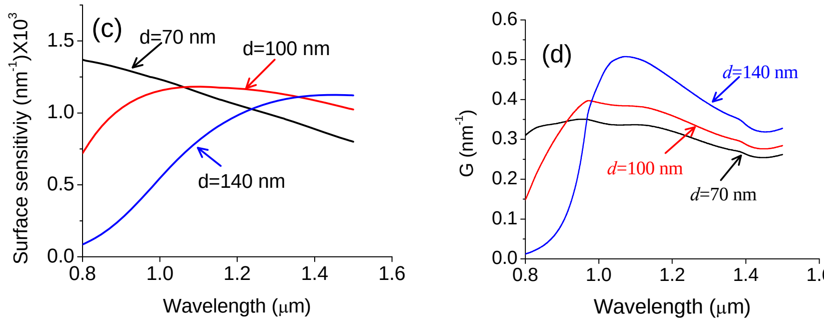

Fig. 6.7. Surface sensing parameters for the TM mode supported by the hybrid waveguide sensor as a function of wavelength. Both silicon and channel thicknesses (*d* and *h*) are 100 nm. (a) Effective mode index (b) Propagation loss (c) Surface sensitivity (b) Combined surface sensitivity factor.

The variations shown in Fig. 6.7 can be explained by examining the field profiles for the three silicon thicknesses (*d*) at various wavelengths (λ). Figure 6.8 shows the field profiles for the three cases at λ = 0.1 μm, 1 μm and 1.4 μm. For the 70 nm thick silicon film, the guided mode always has hybrid nature (Fig. 6.8(a)). With increasing wavelength the field becomes less confined and hence surface sensitivity decreases. In the second case (*d* = 100 nm), the field is very similar to TM_0 mode supported by a silicon slab at λ = 0.8 μm. At longer wavelength (λ = 1.1 μm) the wave converts to hybrid mode, as shown in Fig. 6.8(b). This results in a higher concentration of power in the channel, which in turn results in an increase of surface sensitivity. Like case 1, the hybrid mode becomes less confined at longer wavelength, and sensitivity drops. The over all result is a maximum in sensitivity for certain wavelengths. For the last case (*d* = 140 nm) depicted in Fig. 6.8 (c) the field is similar to TM_0 mode supported by the silicon film at shorter wavelengths but with increasing wavelength, it continues to become more like the hybrid guide. Therefore, the surface sensitivity continually increases with increasing wavelength in this case. More details of the variations of HPWG mode characteristics with waveguide dimensions have been presented in chapter 3.

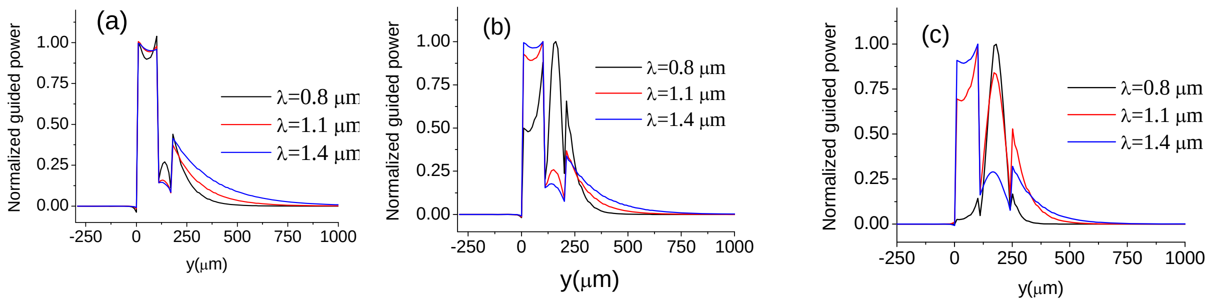

Fig. 6.8. Guided power intensity profiles for three different wavelengths (λ) and three different silicon thicknesses (d). Channel thickness is 100 nm for all cases. (a) d = 70 nm (b) d = 100 nm (c) d = 140 nm.

Figure 6.9 shows the effects of channel thickness (h) and silicon thickness (d) on the sensor performance at a wavelength of 1.05 µm. With increasing channel thickness, the field intensity on the metal surface is reduced. As a result for all cases propagation distance of the mode increases (Fig.6.10(b)) but the surface sensitivity decrease (Fig.6.10(c)). The rate of decrease of surface sensitivity is larger than the rate of increase of propagation distance. Hence for all cases net result is a smaller value of G for increases spacer thickness, as shown in Fig.6.10(d).

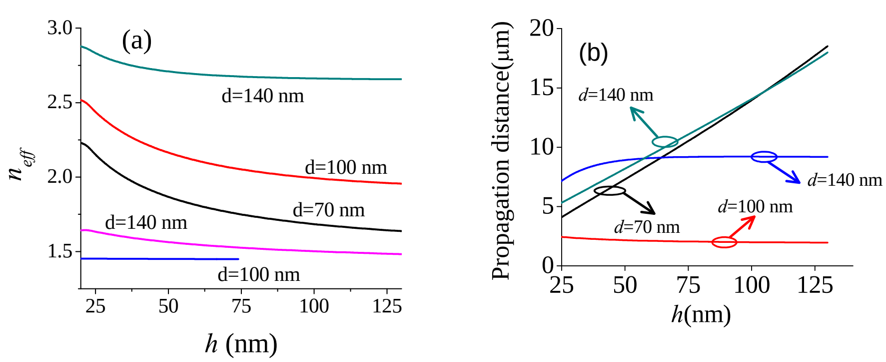

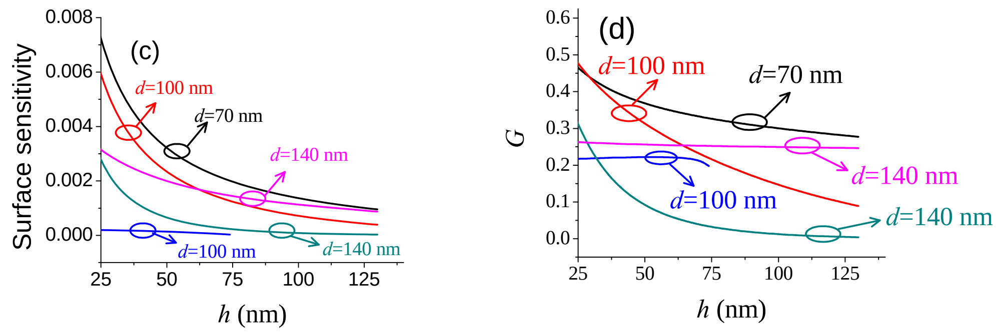

Fig. 6.9. Surface sensing parameters for the TM mode supported by the hybrid waveguide sensor as a function of channel thickness (h) for a number of silicon thicknesses (d). (a) effective mode index (b) propagation loss (c) surface sensitivity (d) surface sensitivity factor.

From the above discussion we make the following observations.

a) The effect of wavelength and silicon thickness on the performance of the hybrid guide is rather complicated. Although a physical picture behind the variation of the mode characteristics is clear, finding a general trend is difficult.

b) Surface sensitivity and G decreases with increasing channel thicknesses in most cases. In some cases it is almost insensitive to the channel thickness.

The objective of this section was to observe the general trends the sensor characteristics follow with change of design parameters. To keep the discussion brief, we presented here results for only the TM mode. Additional results for both TE and TM modes are presented in Appendix C. Optimization of the HPWG sensor for both TE and TM mode are carried out in next section.

6.6. Optimization of the One Dimensional HPWG Sensor

As explained in section 6.3, the HPWG sensor can be used for two kinds of applications. It can be used to achieve detection limit lower than possible by single interface SP sensor. For this kind of applications, the target of the optimization will be to maximize the G for the TM mode and disregard the TE mode since the TM mode always has higher G compared to the TE mode for a HPWG [see Appendix B]. The other kind of application is to use both TE and TM polarizations for making the sensor capable of providing more information about the adlayer or differentiating between bulk and surface change. In this case the target of the optimization would be to achieve sufficiently large G for both polarizations.

In this work we will optimize the HPWG sensor design for both types of applications. As shown in Fig. 6.9, a narrower channel height (h) results in a higher value of G. Though fabrication and fluid flow through nano-channel of even 20 nm width have been demonstrated [Liang 2007], for ease of fabrication, we choose a 100 nm channel thickness in this work. For each of the two applications mentioned above we vary the high index slab thickness and wavelength to optimize G. We investigate two different choices of high index medium: silicon and silicon nitride. The maximum value of G achievable from single interface SP mode (G_{SP_max}) is 0.28 [Berini 2008]. This number will be used as the benchmark for evaluating the performance of the HPWG biosensor.

6.6.1. Optimizing *G* for Single Polarization Application

In this case the TE mode is ignored and the device is designed to achieve the highest value of G for the TM mode while maintaining single mode condition. Table 6.1 summarizes the results of optimization. In case of silicon slab the highest G achievable is 0.545 which is 1.95 times that can be achieved for single-interface SP. Higher value of G is achievable for thicker silicon films. For example, for d = 300 nm, G is 1.006 which is 3.5 time that of G_{SP_max}. However in this case the waveguide supports multiple modes.

The maximum G achievable for the case of silicon nitride is comparable to G_{SP_max}. This is not unexpected. Since the index contrast between silicon nitride and water is relatively smaller, enhancement of power concentration in the channel is lower and hence the values of G in the case of silicon nitride is also closer to G_{SP_max}.

Table 6.1. Optimization of HPWG for single polarization operation

High index material	***d*(nm)**	**G (nm^{-1})**	**λ (μm)**	**L_{Prop} (μm)**
Silicon	155	0.545	1.1	81
Silicon nitride	250	0.396	0.85	47

6.6.2. Optimizing *G* for Dual Polarization Application

Since the values of G for the TE mode are always significantly lower than those of the TM mode (as shown in Appendix B), we aim at maximizing G for the TE mode for the dual polarization operation of HPWG. Table 6.2 summarizes the results of optimization for this case. Similar to the case of section 6.6.1, the high index slab is chosen to be sufficiently thin to ensure single mode condition. To avoid ambiguity, the type of polarization is mentioned as superscript. For example G^{TM} is the highest G value expected for the TM polarization and the corresponding wavelength and propagation distance are designated as λ^{TM} and $L^{TM}_{\mathrm{Pr}op}$ respectively. A similar nomenclature is also used for the TE mode. When the high index medium is silicon, $G^{TE}_{\max}$ is 0.012 which is only 4.3% of $G_{\mathrm{SP\_max}}$. G^{TE} is significantly larger when the high index medium is silicon nitride instead of silicon. In this case for d = 100 nm, G^{TE} is more than 14% of G_{SP_max} while G^{TE}= 0.31 which is slightly higher than G_{SP_max}.

Table 6.2. Optimization of HPWG for dual polarization operation

High index material	***d*(nm)**	G^{TM} **(nm^{-1})**	λ^{TM} **(μm)**	$L^{TM}_{\Pr op}$ **(μm)**	G^{TE} **(nm^{-1})**	λ^{TE} **(μm)**	$L^{TE}_{\Pr op}$ **(μm)**
Silicon	150	0.543	1.05	90	0.012	1.1	280
Silicon nitride	100	0.31	1.1	37	0.0395	0.65	87

As discussed in section 6.4, *G* is valid as sensor's figure of merit only when the sensor length equals the propagation distance of the guided mode. The propagation distance of the TE and TM modes for the case of silicon nitride are 87 μm and 36.5 μm respectively. Therefore, it is not possible to simultaneously achieve $G^{TM-TE\max}_{\max}$ = 0.31 and $G^{TE}_{\max} = 0.0395$ for the same device and a compromise needs to be made. Figure 6.10 shows the variations of normalized combined sensitivity factors with sensor length (*L*). These plots are obtained with the help of equation (6.23). At *L* = 65 μm we achieve $G^{TM}_{eff} = 0.91 G_{SP\_\max}$ and $G^{TE}_{eff} = 0.127 G_{SP\_\max}$. We take this as a reasonable compromise between the performance achievable for TE and TM modes.

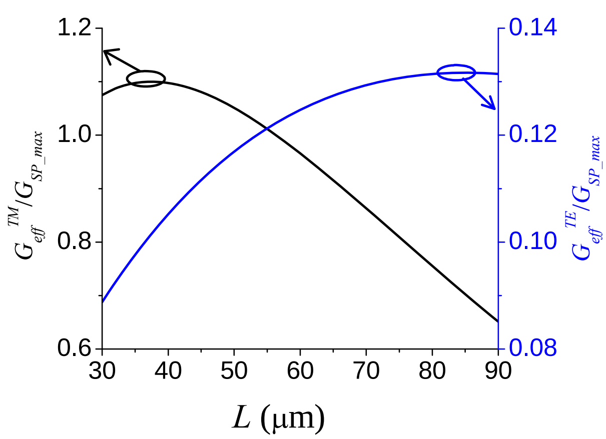

Fig. 6.10. Variations of *G* for TE and TM modes as a function of sensor length.

The analysis carried out in this chapter so far has been for one dimensional HPWG. Implementation of such a sensor will require fabrication of a nano-fluidic channel which is a challenging task. Fabrication can be considerably simplified if the structure is rotated by 90 degree as shown in Fig. 6.11(a). The guided power density for the TM and TE modes are shown in Fig. 6.11(b) and (c) respectively. Arrows indicating in plane electric field vector direction and magnitude are also shown. The directions of the arrows indicate that despite the finite dimensions of the silicon nitride and metal sections, one of the guided mode is almost purely TM and another is almost purely TE. The values of combined surface sensitivity factor (*G*) for the mode shown in Fig. 6. 11(b) is approximately 0.12 which is less than obtainable from single interface SP mode (0.28). The value of the *G* for the TE mode (Fig. 6.11(c)) is 0.042 which is almost identical to that achievable from the one dimensional HPWG sensor.

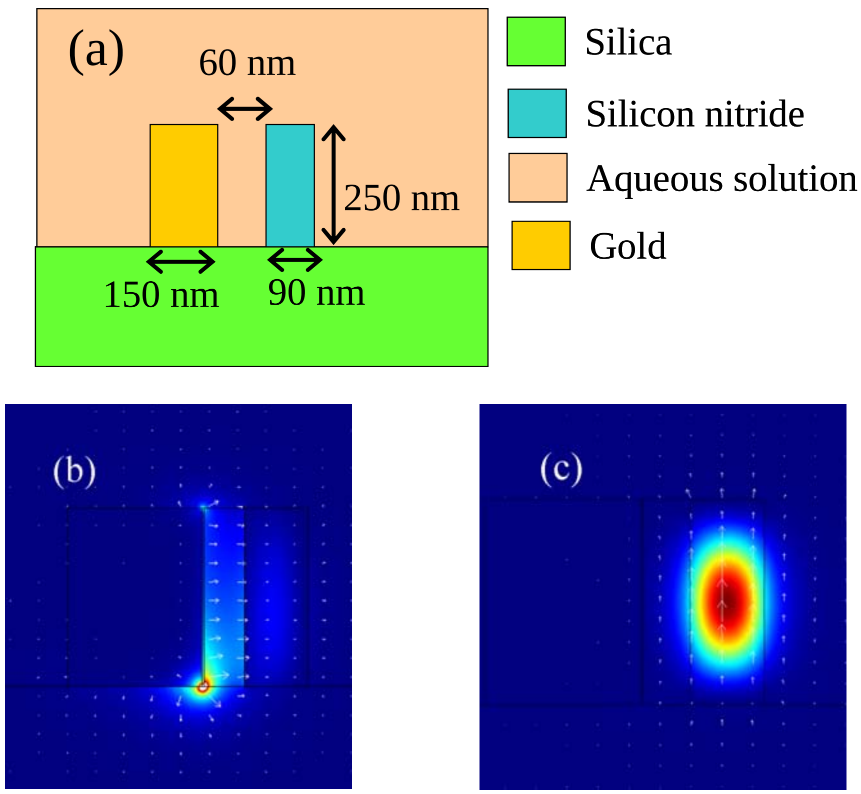

Fig. 6.11. (a) Schematic of the two dimensional HPWG sensor. Power density profiles and electric field arrows for (b) TM mode and (c) TE mode.

6.7. Discussion

In this chapter we have examined in detail the applicability of HPWG for biosensing applications. The hybrid TM mode for the HPWG is highly concentrated in the low index spacer region. Therefore, the HPWG sensor can be more sensitive than purely plasmonic sensors. The polarization diversity can be used for either differentiating between change in adlayer thickness and that of bulk index. It can also be used to find structural information of complex biological molecules (similar to DPI sensing schemes described in Section 6.1).

A detailed study has been carried out to analyze the effects of various parameters on the HPWG sensor performance in Mach-Zehnder configuration and the sensor designs are optimized for both single and dual polarization operations. It was found that the best achievable combined surface sensitivity factor (G) for the single polarization operation of the plasmonic sensor is double that of SP mode for single mode condition. This is achieved when the high index region of HPWG is a 150 nm thick silicon film.

We have also optimized the performance of the sensor for dual polarization operation. Better results for the TE mode sensitivity are achieved when the high index region is silicon nitride instead of silicon. For a 150 nm thick silicon nitride layer and 65 μm device length, the G of the TM mode is 91% of that of single interface SP mode (G_{SP_max}) and that of the TE mode is 12.7% of that of (G_{SP_max}). Though the sensitivity of the TE mode is lower than that of the TM mode, it is still significant and should be useful for many applications.

We have also investigated applicability of a two dimensional HPWG structure for biosensing. Though the sensitivity of the TM mode is reduced compared to the single interface, the sensitivity of the TE mode is almost same as that of the one dimensional case. G_{eff} (defined in Section 6.4.2) of both TE and TM modes for this structure are of the same order of magnitude of G_{SP_max}.

As mentioned in Section 6.1 and 6.2, two very popular optical biosensing schemes are dual polarization interferometry (DPI) and SP sensing. The advantages and limitations of these two schemes are somewhat complimentary. The reason behind the popularity of DPI is its ability to obtain structural information about biological molecules by utilizing both TE and TM polarizations. However, these devices are long (more than 10 millimeters) and hence DPI is less precise for investigation of chemical kinetics [Sonesson 2007]. Moreover, the absence of a metal surface makes functionalization of DPI sensor surface more challenging than the case of SP sensor. Plasmonic i.e., SP sensors, on the other hand are very compact, ideal for analysis of chemical kinetics but since they can support only the TM mode, the information obtained from a SP sensing scheme is limited. Since the HPWG sensor can support both TE and TM polarizations and also have a very short length (less than 100 μm), it can combine the advantages of SP sensing (ease of functionalization because of presence of metal surface, compact size and high precision necessary for study of chemical kinetics) and that of DPI (polarization diversity) on the same platform.

Chapter 7

Contributions and Conclusions

Plasmonics has been a very active area of nanophotonic research for last few years. Many different applications of plasmonics have been suggested. Although this extensive research on plasmonics has highlighted its great potential, the large propagation loss of surface plasmon diminishes the usefulness of many of these proposals for real life applications. Several ways to mitigate the issue of propagation loss, e.g., use of gain medium or long range plasmon have been suggested. However, the loss reduction using these schemes is accompanied by either a significant increase of system complexity or increase of the device size.

The objectives of this dissertation were to find some mechanism to address the issue of large propagation loss of plasmonic waveguides and also to design plasmonic devices which outperform existing devices. To meet these objectives we have proposed a new hybrid plasmonic wave guiding (HPWG) mechanism that combines plasmonic and dielectric wave guiding mechanisms. The proposal has been widely recognized by the plasmonics community as one of the best ways to achieve a good compromise between loss and confinement. We have also carried out theoretical analysis to clarify the physical picture of the mode formation in such guide and have suggested a number of applications ranging from polarizers and couplers to biosensors. The results presented in this dissertation lay the ground work for future research in HPWG.

7.1. Original Contributions

In chapter 3 we proposed the HPWG consisting of a metal surface separated from a high index slab by a low index spacer and analyze its properties. The novel contributions are:

a) We proposed the HPWG which provides a better compromise between loss and confinement than purely plasmonic waveguides.

b) We carried out a detailed analysis that clarified the nature of the modes supported by HPWG and dispelled doubts raised by some researchers about hybrid nature of the modes guided by such a structure.

The introduction of the concept of HPWG in chapter 3 was followed by an analysis of the two dimensional HPWG in chapter 4. The novel contributions are:

a) We proposed a two dimensional HPWG structure was proposed. The proposed structure offers the possibility of integration of silicon photonics and nanoplasmonics on the same platform.

b) We analyzed the effects of various parameters on the HPWG performance in detail. These results should be useful for designing HPWG devices for various applications.

In chapter 5 we investigated the possibility of using HPWG for integrated optic communication systems. The novel contributions are:

a) We explored the possibility of designing HPWG which supports both TE and TM modes. A detailed analysis has been carried out to analyze the effects of various parameters on the two polarizations.

b) We designed the following SOI compatible HPWG integrated optic devices which utilize the polarization diversity of HPWG.

1) A TM-pass polarizer which is very compact and can provide better extinction ratio than achievable from use of a purely SOI based polarizer.

2) A TE-pass polarizer that has very low insertion loss and high extinction ratio. It is the most compact, broadband SOI compatible TE-pass polarizer proposed to date.

3) A polarization independent HPWG directional coupler which is very compact and offers more flexibility compared to previously reported SOI based polarization independent directional coupler.

These designs are the first demonstrations that plasmonic devices can outperform their dielectric waveguide based counterparts without suffering excessive propagation loss.

c) We also analyzed the possibility of implementing compact bends using the HPWG. It was found that the HPWG bend outperform previously reported plasmonic waveguides.

The work presented in this chapter highlights both the advantages and limitations of HPWG devices and should serve as a guideline for future work on HPWG device design.

We explored the applicability of HPWG for biosensing in chapter 6. The novel contributions are:

a) We proposed a HPWG biosensor. The sensor is more sensitive than a purely plasmonic sensor and is capable of obtaining more information about biological molecules compared to purely plasmonic sensors. It also has the capability to differentiate between change of bulk index and adlayer thickness.

b) We carried out a detailed numerical analysis to optimize the HPWG sensor and determined the best possible sensitivities achievable from such a sensor.

c) We proposed a two dimensional HPWG sensor that requires a simpler fabrication process compared to the one dimensional HPWG sensor.

A list of publications resulting from this study is provided at the end of this dissertation.

7.2. Future Research Directions

There are some immediate paths for extending the research presented in this dissertation. The most immediate extension of the work should be implementation of the devices proposed in this dissertation. Our group has already made some progress in this direction. For example, we have fabricated and tested the first HPWG TE-pass polarizer which shows very promising results [Sun 2012].

This dissertation work can act as a guideline for further exploration of HPWG for other applications. We have also made some progress in this regard. For example we have recently designed ultra compact, low loss, broadband directional coupler and polarization rotator. New kind of HPWG devices, for example electro-optics modulator, laser etc can be investigated. Achieving lossless propagation of HPWG by use of gain medium can also be explored.

More analysis can also be carried out about HPWG sensors. For example, enhancement of efficiency of Raman scattering by placing metal nano particle in the nano fluidic channel of HPWG can be a promising idea. Another interesting idea is to use the coaxial hybrid guide [Zhao 2010] for biosensing. New types of biosensors may be designed which will detect presence of biomolecules by detecting the change of light transmission through such hole arrays.

One limitation of the HPWG is the extra fabrications steps required to implement it compared to dielectric waveguides. Although several HPWG designs have already been proposed for which only standard planar fabrication steps are required, a simplified fabrication process will make applications of HPWG more attractive. As illustrated by the recent works on HPWG by Flammer and coworkers [Flammer 2010], there are still a lot of opportunities to simplify HPWG fabrication even further.

References

[Almedia 2004]Almeida, V. R., Xu,Q., Barrios, C. A., and Lipson, M., "Guiding and confining light in void nanostructure," Opt. Lett. 29: 1209-1211 (2004).

[Anderson 2002] Anderson N. L, Anderson N. G., “The human plasma proteome: history, character, and diagnostic prospects,” Mol. Cell. Proteomics, 1: 845-867 (2002).

[Atwater 2007] Atwater, H., “The promise of plasmonics,”Scientific American, 56-63, (2007)

[Avrustsky 2010] Avrutsky, I., Soref, R.¸ Buchwald, W., “Sub-wavelength plasmonic modes in a conductor-gap-dielectric system with nanoscale gap,” Opt. Exp., 18: 348-363 (2010).

[Avrutsky 2008] Avrutsky, I., “Integrated optical polarizer for silicon-on-insulator waveguides using evanescent wave coupling to gap plasmon-polaritons,” IEEE J. of Selected Topics in Quantum Electronics, 14: 1509-1514, 2008.

[Barnes 2003] Barnes, W. L., Dereux, A., Ebbesen, T. W."Surface plasnon subwavlength optics,” Nature 424 : 824-830 (2003).

[Barnes 2006] Barnes, W. L., “Surface plasmon–polariton length scales: a route to sub-wavelength optics,” J. Opt. A: Pure Appl. Opt. 8: S87 (2006).

[Bardhan 2011] Bardhan, R, Lal, S., Joshi, A., Halas., N. J., “Theranostic Nanoshells: From Probe Design to Imaging and Treatment of Cancer,” Acc. Chem. Res. 44: 936- 946 (2011).

[Bashevoy 2006] Bashevoy, M. V., Jonsson, F., Krasavin, A. V., Zheludev, N. I., Chen, Y., and Stockman, M. I., “Generation of traveling surface plasmon waves by free-electron impact,” Nano Letters 6: 1113-1115 (2006).

[Berini 2008] Berini, P., “Bulk and surface sensitivities of surface plasmon waveguides,” New J. of Phys., 10: 105010 (2008).

[Berini 2009] Berini, P., “Long-range surface plasmon-polaritons,” (OSA) Advances in Optics and Photonics, 1:484-588 (2009).

[Berini 2010]Leon I. D., and Berini, P., “ Amplification of long-range surface plasmons by a dipolar gain medium,” Nature Photonics 4: 382 - 387 (2010).

[Berkovich 2008] N. Berkovich, M. Orenstein, S. G. Lipson, “Novel complex modes in asymmertical nanoscale plasmonic waveguides,” Opt. Exp., 16: 17842-17847 (2008).

[Bhatt 2012] Bhatt, G. R., Das, B. K., “Improvment of polarization extinction in silicon waveguide devices,” Opt. Comm. 285: 2067-2070 (2012).

[Bian 2011] Bian,Y., Zheng, Z., Liu, Y., Liu, J., Zhu, J., and Zhou, T., "Hybrid wedge plasmon polariton waveguide with good fabrication-error-tolerance for ultra-deep-subwavelength mode confinement," Opt. Express 19: 22417-22422 (2011).

[Bloemer 1996] Bloemer, M. J., and Haus, W.J., "Broadband waveguide polarizers based on anisotropic optical constants of nanocomposite films," J. Light. Tech. 14: 1534-1540 (1995).

[Breukelaar 2004] I. G. Breukelaar, "Surface plasmon-polaritons in thin metal strips and slabs: waveguiding and mode cutoff," Master Thesis, University of Ottawa (2004).

[Brongersma 2000] Brongersma, M. L., Hartman, J. W., and Atwater, H. A.," Electromagnetic energy transfer and switching in nanoparticle chain arrays below the diffraction limit," Phys. Rev. B, 62: R16356-R16359 (2000).

[Breukellar 2004] Breukellar, I. G., Surface plasmon-polaritons in thin metal strips and slabs: Waveguiding and mode cutoff, M. A. Sc. Thesis, (University of Ottawa, 2004).

[Boltaseva 2005] Boltasseva, A., Nikolajsen, T., Leosson, K., Kjaer, K., Larsen, M. S. , Bozhevolnyi, S. I., "Integrated optical components utilizing long-range surface plasmon polaritons," J. Lightwave Tech., 23: 413-422, (2005).

[Bozhevolnyi 2006] Bozhevolnyi, S. I., Volkov, V. S., Devaux, E., Laluet, J-Y., Ebbesen, T. W. "Channel Plasmon subwavelength waveguide components including interferometers and ring resonators," Nature 440: 508-511 (2006).

[Buckley 2007] Buckley, R., and Berini, P., "Figures of merit for 2D surface plasmon waveguides and application to metal stripes," Opt. Express 15: 12174-12182 (2007).

[Buckley 2009] Buckley, R. , Berini, P., "Long-range substantially nonradiative metallo-dielectric waveguide," Opt. Lett. 34: 223-225 (2009).

[Chen 2005] Chen, C., Pang, L., Tsai, C., Levy, U., and Fainman, Y., "Compact and integrated TM-pass waveguide polarizer," Opt. Express 13: 5347–5352 (2005)

[Cheng 2011] Cheng, J., Zhang, W., Zhou, Q., Wang, Y., Huang, Y., and Peng, J.,"Single polarization transmission in pedestal-supported silicon waveguides," Opt. Lett. 36: 1797-1799 (2011).

[Chu 2011] Chu, H-S., Akimov, Y.A., Bai, P., Li, E-P., "Hybrid dielectric-loaded plasmonic waveguide and wavelength selective components for efficiently controlling light at subwavelength scale," J. Opt. Soc. Am. B, 12: 2895-2901 (2011).

[Cooper 2009] M. L. Cooper and S. Mookherjea, "When and how coupled-mode theory fails in high-index contrast arrayed and multi-slot waveguides," CLEO/QELS, paper ID JThE94 (2009).

[Ctyroky 1997] Ctyroky, J. Homola, J. Skalsky, M.,"Tuning of spectral operation range of a waveguide surface plasmon resonance sensor," Electron. Lett., 33: 1246 – 1248 (1997).

[Cui 2008] Cui, Y., Wu, Q., Schonbrun, E., Tinker, M., Lee, J-B., and Park, W., "Silicon-based 2-D slab photonic crystal TM polarizer at telecommunication wavelength," IEEE Photon.

Tech. Lett. 20: 641 – 643 (2008).

[Daghestani 2010] Daghestani, H. N., Day, B. W., "Theory and applications of surface plasmon resonance, resonant mirror, resonant waveguide grating, and dual polarization interferometry biosensors," Sensors, 10: 9630-9646 (2010).

[Dai 2009] Dai, D., He, S., "A silicon-based hybrid plasmonic waveguide with a metal cap for a nano-scale light confinement," Opt. Exp., 17: 16646-1665, (2009).

[Dai 2010] Dai, D., Wang, Z., Julian, N. and Bowers, J. E., "Compact broadband polarizer based on shallowly-etched silicon-on-insulator ridge optical waveguides" Opt. Expr., 18: 27404- 27415, 2010.

[Dejardin 2006] P. Dejardin, Chapter 4, "Proteins at Solid-Liquid Interfaces- Principles and Practice, Part II, 75-104 (2006).

[Dionne 2006] Dionne, J. A., Sweatlock, L. A., Atwater, H. A., and Polman, A., "Plasmon slot waveguides: Towards chip-scale propagation with subwavelength-scale localization," Physical Review B, 73 (3): 035407 (2006).

[Dionne 2010] Dionne, J. A., Sweatlock, L. A., Sheldon, M. T., Alivisatos, A. P., and Atwater, H. A., "Silicon-Based Plasmonics for On-Chip Photonics," IEEE J. of Quantum Electronics., 16(1): 295-306 (2010).

[Ditlbacher 2002] Ditlbacher, H., Krenn, J. R., Felidj, N. , Lamprecht, B., Schider, G., Salerno, M., Leitner, A., Aussenegg, F. R., "Fluorescence imaging of surface plasmon fields," Applied Physics Letters 80(3): 404-406 (2002).

[Dokania 2009] Dokania, R. K., "Analysis of challenges for on-chip optical interconnects," Proceedings of the 19th ACM Great Lakes Symposium on VLSI, pp. 275-280, 2009.

[Fan 2008] Fan, X, White, I.M., Shopova, S. I, Zhu, H., Suter, J. D., Sun, Y., "Sensitive optical biosensors for unlabeled targets: A review," Analytica Chimica Acta, 620: 8-26 (2008).

[Feigenbaum 2007] Feigenbaum, E., and Orenstein, M., "Modeling of complementary (void) plasmon wave guiding," J. of Lightwave Technology, 25(9): 2547-2562 (2007).

[Feijter 1978] Feijter, J. A. D., Benjamins, J., Veer, F. A., "Ellipsometry as a tool to study the adsorption behavior of synthetic and biopolymers at the air–water interface," Biopolymers 17: 1759-1772 (1978).

[Flammer 2010] Flammer, P. D., Banks, J. M., Furtak, T. E., Durfee, C. G. , Hollingsworth, R. E. and Collins, R. T., "Hybrid plasmon/dielectric waveguide for integrated silicon-on-insulator optical elements," Opt. Express 18: 21013-21023 (2010).

[Foster 2011] K-Y. Wang, Foster, A. C., "Optimization of CMOS-Compatible Hybrid Plasmonic Waveguides for Nonlinear Applications," OSA Meeting on Specilaty Optical Fibers, Paper ID JTuB15 (2011)

[Fujii 2009]M. Fujii, J. Leuthold, W. Freude, "Dispersion relation and loss of subwavelength confined mode of metal-dielectric-gap optical waveguides," IEEE Photon. Tech. Lett. 21: 362-364, (2009).

[Fujisawa] Fujisawa, T., Koshiab, M., "Polarization-independent optical directional coupler based on slot waveguides," Opt. Lett. 31: 56-58 (2006).

[Gather 2010] Gather, M. C., Meerholz, K., Danz, N., and Leosson, K., "Net optical gain in a plasmonic waveguide embedded in a fluorescent polymer," Nature Photonics 4: 457 - 461 (2010)

[Hardy 1985] A. Hardy, W. Streifer, "Coupled mode theory for parallel waveguides", J. Light. Tech., 3: 1135-1146 (1985).

[Haus 1991] H. A. Haus, W. Huang, "Coupled-mode theory," Proceedings of IEEE, 79: 1505-1518, 1991.

[Hempelmann 1995] Hempelmann, U., Herrmann, H., and Mrozynski, G.," Integrated optical proton exchanged TM-pass polarizers in LiNb03: Modelling and experimental performance," J. Light. Tech. 13: 1750-1759 (1995).

[Holmgaard 2010] Holmgaard, T., Gosciniak, J., and Bozhevolnyi, S. I.,"Long-range dielectric-loaded surface plasmon-polariton waveguides," Opt. Express 18: 23009-23015 (2010).

[Homola 2006] Homola, J., *Surface plasmon resonance based sensors*, Springer (2006).

[Homola 2003] Homola, J., "Present and future of surface plasmon resonance biosensors," Anal Bional Chem, 377: 528-539, (2003).

[Hopfield 1958] Hopfield, J. J. , "Theory of the contribution of excitons to the complex dielectric constant of crystals," Phys. Rev. 112, 1555–1567 (1958)

[Hsu 2010] Hsu, S-H., "Signal power tapped with low polarization dependence and insensitive wavelength on silicon-on-insulator platforms", J. Opt. Soc. B., 27: 941-947 (2010).

[Hunsperger 2002] R. G. Hunsperger, Integrated optics: Theory and technology, Springer (2002)

[ITRS 2009] ITRS Roadmap for optical interconnect, 2009.

[Johnson 1972] P. B. Johnson, R. W. Christy, "Optical constants of noble metals," Phys. Rev. B, 6:4370-4379, (1972).

[Kano 1998] Kano, H., Mizuguchi, S., and S. Kawata, "Excitation of surface-plasmon polaritons by a focused laser beam," JOSA B 15: 1381-1386 (1998).

[Kim 2007] Kim, J.¸ Song, K-B., “Recent progress of nano-technology with NSOM,” Micron, 38: 409-426 (2007).

[Koos 2007] Koos, C., Jacome, L., Poulton, C., Leuthold, J., Freude, W., “Nonlinear silicon-on-insulator waveguides for all-optical signal processing, “ Opt. Exp. 15: 5976-5990 (2007).

[Kou 2011] Kou, Y., Ye, F., and Chen, X., "Low-loss hybrid plasmonic waveguide for compact and high-efficient photonic integration," Opt. Express 19: 11746-11752 (2011).

[Kou 1993] Kou, L., Labrie, D. , Chylek, P., “Refractive indices of water and ice in the 0.65- to 2.5-μm spectral range,” Appl. Opt. 32: 3531-3540 (1993).

[Krasavin] Krasavin, A.V., and Zayats, A. V., “Electro-optic switching element for dielectric-loaded surface plasmon polariton waveguides,” Appl. Phys. Lett. 97: 041107 (2010).

[Kwon 2010] Kwon, M-S., “Theoretical investigation of an interferometer-type plasmonic biosensor using a metal-insulator-silicon waveguide,” Plasmoncs, 5:347-354 (2010).

[Lei 2010] Lei, D.Y., Li, J., Dominguez, A. I. F , Ong, H. C., and Maier, S. A., “Geometry dependence of surface plasmon polariton lifetimes in nanohole arrays,” *ACS Nano* 4: 432 – 438 (2010).

[Lavers 1994] Lavers, C.R., Wilkinson, J.S., “A waveguide-coupled surface-plasmon sensor for an aqueous environment,” Sensors and Actuators B, 22: 75-81 (1994). [Leon 2010] Leon, I. D.¸ and Berini, P., “Amplification of long-range surface plasmons by a dipolar gain medium,” Nature Photon. 4: 382 – 387 (2010).

[Li 2008] Li, G., Xu, A., “Analysis of the TE-pss or TM-pass metal-clad polarizer with a resonant buffer layer,” J. Light. Tech. 26: 1234-1241 (2008).

[Liang 2007] Liang, X., Morton, K. J., Austin, R. H., and Chou, S. Y., “Single Sub-20 nm wide, centimeter-long nanofluidic channel fabricated by novel nanoimprint mold fabrication and direct imprinting,” Nano Lett., 2007, 7 : 3774–3780 (2007).

[Lim 2007] Lim, S. T., Png, C. E., Ong, E. A., “Single mode polarization independent submicron silicon waveguide based on geometrical adjustments,” Opt. Exp. 15: 11061-11072 (2007).

[Lu 2011] Lu, F. F., Li, T., Hu, X. P., Cheng, Q. Q., Zhu, S. N., Zhu, Y. Y., “Efficient second-haromic generation in nonlinear plasmonic waveguides,” Opt. Lett., 36: 3371-3373 (2011).

[Lu 1990] Lu, J. Q. and Maraduddin, A. A. “Channel plasmons”, Phys. Rev. B, 42: 11159-11165 (1990).

[Lumerical] *FDTD Solutions Reference Guide,* (Lumerical Solutions, 2009).

[Ma 2010] Ma, Y-F., Sung, M-J., Huang, D-W., “Controlling the polarization dependence of dual-channel directional couplers formed by silicon-on-insulator slot waveguides”, Applied Optics, 49(36): 6979-6985 (2010).

[Maier 2007] Maier, S. A., "Plasmonics: Fundamentals and Applications" Springer 2007.

[Marks 2008] Marks, R. S., Lowe, C. R., Cullen, D. C., Weetall, H. H., Karube, I., *Handbook of Biosensors and Biochips*, John Wiley and Sons (2008).

[Mason 2010] Mason, D. R., Gramotnev, D. K., and Kim, K. S., "Wavelength-dependent transmission through sharp 90° bends in sub-wavelength metallic slot waveguides," Opt. Express 18: 16139-16145 (2010).

[Miller 2009] Miller, D. A. B., "Device requirements for optical interconnect on silicon chip," Proc. IEEE, 97: 1166-1185, 2009.

[Millette 2011] Millette, P. A., "The Heisenberg undertainty principle and the Nyquist-Shannon sampling theorem," arXic.1108.3135v1[quant-ph] 16 Aug 2011.

[Mills 1974] Mills, D. L. and Burstein, E. "Polaritons : the electromagnetic modes of media," Rep. Prog. Phys. 37: 817-926 (1974).

[Naimushin 2003] Naimushin, A. N., Soelberg, S. D., Batrholmew, D. W., Elkind, J. L., Furlong, C. E., "A portable surface plasmon resonance (SPR) sensor system with temperature regulation," Sens. Act. B 96, 253-260 (2003).

[Nam 2009] Nam, S. H., Taylor, A. J., and Efimov, A.¸"Subwavelength hybrid terahertz waveguides," Opt. Exp., 17: 22890-22897 (2009).

[Nezhad 2004] Nezhad, M., Tetz,K., and Fainman, Y., "Gain assisted propagation of surface plasmon polaritons on planar metallic waveguides," Opt. Express 12: 4072-4079 (2004).

[Nellen 1988] Nellen, P. M., Tiefenthaler, K., and Lukosz, W., "Integrated optical input grating couplers as biochemical sensors," Sens. Act. 15, 285-295 (1988).

[Nellen 1993] Nellen, P. M., Lukosz, W., "Integrated optical input grating couplers as direct affinity sensors," Biosens. & Bioelectron. 8: 129-147 (1993).

[Ng 2010] Ng, T. K., Khan, Z. M., Ooi, B. S., "Integrated Cu-based TM-pass polarizer using CMOS technology platform", Photonics Global Conference, 14: 1 - 3, (2010).

[Oulton 2008] Oulton, R. F., Sorger, V. J., Genov, D. A. , Pile, D. F. P., Zhang, X., "A hybrid plasmonic waveguide for subwavelength confinement and long range propagation," Nature Photonics, 2: 496-500, (2008).

[Oulton 2009] Oulton, R. F., Sorger, V. J., Zentgraf, T. , Ma, R-M., Gladden, C., Dai,L., Bartal, G. and Zhang, X., " Plasmon lasers at deep subwavelength scale" Nature 461: 629-632, 2009.

[Palik 1985] E. D. Palik, Handbook of optical constants of solids, (Academic Press, Inc. 1985).

[Pan 2012] Pan, Z., Guo, J., Soref, R., Buchwald, W., and Sun, G., "Mode properties of flat-top silver nano-ridge surface plasmon waveguides," arXiv:1112.0780v1 [physics.optics].

[Park 2007] Park, H., Fang, A. W., Cohen, O., Jones, R., Paniccia, M. J., Bowers, J. E.,“A hybrid AlGaInAs-Silicon evanescent amplifier,” IEEE Phot. Tech. Lett. 19: 230-232 (2007).

[Passaro 2008] Passaro, V.M.N., Dell’Olio, F., Timotijevic, B., Masahnovich, G. Z., Reed, G. T., “Polarization-insensitive directional couplers based on SOI wire waveguides”, Open Optics Journal, 2: 6-9 (2008).

[Pile 2005] Pile, D. F. P., Ogawa, T., Gramotnev, D. K., Okamoto, T., Haraguchi, M., Fukui, M. and Matsuo, S. “Theoretical and experimental investigation of strongly localized plasmons on triangular metal wedges for subwavelength wave guiding”, Appl. Phys. Lett., 87, 061106, (2005).

[Prasad 2003] Prasad, P. N., *Introduction to biophotonics*, John Wiley and Sons (2003).

[Raether 1986] Raether, H., “Surface plasmons on smooth and rough surfaces and on gratings,” Springer-Verlag (1986).

[Rashleigh 1976] Rashleigh, S. C. “Four-layer metal-clad thin film optical waveguides,” Optical and Quantum Electronics, 8: 49 – 60 (1976).

[Ritchie 1957] Ritchie, R. H., "Plasma Losses by Fast Electrons in Thin Films," Physical Review 106 (5): 874–881 (1957).

[Sambles 1991] Samlbles, J. R., Bradbery, G. W., Yang, F.,“Optical excitation of surface plasmons: an introduction,” Contemporary Physics, 32(3): 173-183 (1991).

[Sharma 2011] Sharma, V.K., Kumar, A., Kapoor, A., “High extinction ratio metal–insulator–semiconductor waveguide surface plasmon polariton polarizer,” Opt. Comm., 284: 1815-1821 (2011).

[Skorobogatiy 2006] Skorobogatiy, M. and Kabashin, A. V., “Photon crystal waveguide-based surface plasmon resonance biosensor,” Appl. Phys. Lett. 89: 143518 (2006).

[Snyder 1987] A. W. Snyder, A. Ankiewicz, A. Atlintas, “Fundamental error of recent coupled mode formulations,” Electron. Lett., 23: 1097-1098 (1987).

[Sonesson 2007] Sonesson, A.W., Callisen, T. H., Brismar, H, Elofsson, U. M., “A comparison between dual polarization interferometry (DPI) and surface plasmon resonance (SPR) for protein adsorption studies,” Colloids and Surfaces B, 54: 236-240 (2007)

[Song 2010] Song, U., Wang, J., Li, Q., Yan, M., Qiu, M., “Broadband coupler between silicon waveguide and hybrid plasmonic waveguide,” Optics Express, 18(12): 13173-13179 (2010).

[Stefanou 2004] Stefanou, S., Hamel, J. S., Baine, P., Bain, M., Armstrong, B. M., Gamble, H. S., Kraft, M., Kemhadijan, H. A., “Impact of buried oxide thickness and ground plane resistivity on substrate cross-talk in ground plane silicon-on-insulator (GPSOI) cross-talk suppression technology,” Proceedings of IEEE International SOI Conference, pp.84-85 (2004).

[Steinberger 2006] Steinberger, B., Hohenau, A., Ditlbacher, H., Stepanov, A. L., Dretz, A., “Dielectric stripe on gold as surface plasmon waveguides,” Appl. Phys. Lett., 88: 094104 (2006).

[Srituravanich 2004] Srituravanich, W., Fang, W., Sun. C., Luo, Q., Zhang, X., “Plasmonic nanolithography,” Nano Letters, 4: 1085-1088 (2004).

[Sun 2012] Sun, X., Alam, M. Z., Wagner, S. J., Aitchison, J. S., and Mojahedi, M., "Compact Hybrid Plasmonic TE-pass Polarizer on SOI," CLEO 2012, paper CTu1A.8.

[Takahara 1997] Takahara, J., Yamagishi, S., Taki, H., Morimoto, A., Kobayashi, T., “Guiding of a one-dimensional optical beam with nanometer diameter,” Opt. Lett., 22: 475-477 (1997).

[Takahara 2004] Takahara, J., Fukasawa, Y., Ohnishi, F., and Kobayashi, T., "Polarized light emission excited by surface plasmon polariton in nano metal-gap structures," in Conference on Lasers and Electro-Optics/International Quantum Electronics Conference and Photonic Applications Systems Technologies, Technical Digest (CD) (Optical Society of America, 2004), paper IWA33.

[Takahara 2005] Takahara, J., Kusunoki, F., Kobayashi, T., “Guiding of two-dimensional optical waves in a negative dielectric gap having a dielectric core,” Proceedings of SPIE., 5928: 59280D-1 (2005).

[Tejeira 2007] Tejeira, F. L., Rodrigo, S. G., Moreno, L. M, Vidal, F. J. G., Devaux, E., Ebbesen, T. W., Krenn, J. R. , Radko, I. P., Bozhevolnyi, S. I., González, M. U. , Weeber, J. C., and Dereux, A., “Efficient unidirectional nanoslit couplers for surface plasmons,” *Nature Physics 3*, 324 - 328 (2007).

[Thyagarajan 1991] Thyagarajan, K., Seshadri, S. D., Ghatak, A.K., “Waveguide polarizer based on resonant tunneling,” J. Light. Tech., 9: 315-317 (1991).

[Tiefenthaler 1989] Tiefenthaler, K., and Kukosz, W., “Sensitivity of grating couplers as integrated-optical chemical sensors,” JOSA.B 6: 209-220 (1989).

[Tsang 2002] Tsang, H. K., Wong, C. S>, Linag, T. K., Day, I. E., Roberts, S. W., Harpin, A., Drake, J., Ashgari, M., “Optical dispersion, two-photon absorption and self-phase modulation in silicon waveguides at 1.5 μm wavelength,” Appl. Phys. Lett., 80: 416- 418 (2002).

[Veronis 2005] Veronis, G., and Fan, S.,"Guided subwavelength plasmonic mode supported by a slot in a thin metal film," Optics Letters, 30: 3359-3361 (2005).

[Wang 2010] Wang, Q., and Ho, S-T., “Ultra compact TM-pass silicon nanophotonic waveguide polarizer and design,” IEEE J. Photon. 2: 49 – 56 (2010).

[Wang 2011] Wang,J., Guan, X., He,Y., Shi,Y., Wang,Z., He,S., Holmström,P., Wosinski,L., Thylen, L., and Dai, D., "Sub-μm^2 power splitters by using silicon hybrid plasmonic waveguides," Opt. Express 19: 838-847 (2011).

[Wu 2007] Wu, C., Jin, Z. , Wang, H., Ma, H., Wang, Y., “Design and fabrication of a nanofluidic channel by selective thermal oxidation and etching back of silicon dioxide made on a silicon substrate”, J. Micromech. Microeng. 17: 2393–2397 (2007).

[Xiao 2010] Xiao, X., Gao, Y., Xiang, J., Zhou, F., “laser-induced thermal effect in surface plasmon resonance,” Analytica Chimia Acta, 676: 75-80 (2010).

[Xiao 2011] Xiao, J., Liu, J., Zheng, Z., Bian, Y., and Wang, G., “Design and analysis of a nanostructure grating based on a hybrid plasmonic slot waveguide,” J. of Optics, 13:105001 (2011).

[Zia 2006] Zia, R., Schuller, J. A., Chandran, A., Brongersma, M. L.,“ Plasmonics: the next chip-scale technology,” Materials Today, 9: 20-27 (2006).

[Zhao 2002] Zhao, D., Shi, B., Jiang, Z., Fan, Y., and Wang, X, “Silicon-based optical waveguide polarizer using photonic bandgap,” Appl. Phys. Lett., 81: 409-411 (2002).

[Zhao 2010] Zhao, Y., and Zhu,L., "Coaxial hybrid plasmonic nanowire waveguides," J. Opt. Soc. Am. B 27: 1260-1265 (2010)

[Zhou 2010] Zhou, G., Wang,T., and Su, Y., “Broadband optical parametric amplifier in ultra-compact plasmonic waveguide,” Proc. SPIE 7987: 79870A (2010).

[Zhou 2011] Zhou, L, Sun, X., Li, X., Chen, J., “Miniature microring resonator based on a hybrid plasmon waveguide,” Sensors, 11: 6856-6867 (2011).

[Zourob 2008] Zourob, M., Elwary, S., Turner, A., *Principles of bacterial detection: Biosensors, Recognition receptors and Microsystems*, Springer (2008).

Appendix A

Uncertainty Relation in Fourier Transform

Heisenberg uncertainly principle can be derived from the Uncertainty Theorem of Fourier transform [Millette 2011] which relates the effective width of a function $W(f)$ with the effective width of its Fourier transform ($W(\tilde{f})$) by the following relation

$$W(f)W(\tilde{f}) \geq 1/2$$

Here f and $\tilde{f}$ are a function and its Fourier transform respectively and their width $W(f)$ and $W(\tilde{f})$ are defined as

$$|W(f)|^2 = \frac{\int_{-\infty}^{\infty} |f(u)|^2 [u - M(f)]^2 du}{\int_{-\infty}^{\infty} |f(u)|^2 du}$$

Where $M(f)$ is defined as

$$M(f) = \frac{\int_{-\infty}^{\infty} |f(u)|^2 u du}{\int_{-\infty}^{\infty} |f(u)|^2 du}$$

There are two common ways of defining Fourier transform and the final form of the uncertatinty relation depends on the specific form of Fourier transform used. For a time function f and its Fourier transform ν the Fourier transform can be defined as

$$f(t) = \int_{-\infty}^{\infty} \tilde{f}(\nu) \exp(2\pi i \nu t) d\nu$$

$$\tilde{f}(t) = \int_{-\infty}^{\infty} f(t) \exp(-2\pi i \nu t) dt$$

If the width of the function *f* in time is *Δt* and the corresponding spread of the Fourier transform is $\Delta\nu$ in frequency domain, they are related by the uncertainty relation

$$\Delta t \Delta \nu \geq 1/2$$

Another way of writing Fourier transform is to use circular frequency $\omega=2\pi\nu$.

$$f(t) = \frac{1}{2\pi}\int_{-\infty}^{\infty} \tilde{f}(\omega)\exp(2\omega t)d\omega$$

$$\tilde{f}(\omega) = \frac{1}{2\pi}\int_{-\infty}^{\infty} f(t)\exp(-\omega t)dt$$

Uncertainty relation in this case takes the form

$$\Delta t \Delta \omega \geq \pi$$

The Fourier transform of a position function *f*(x) produces a corresponding function $\tilde{f}(k)$ in the wave number space. The spread of the function in spatial domain (Δx) and the corresponding s spread in wave number domain (Δ*k*) are related by

$$\Delta x \Delta k \geq \pi$$

Appendix B

Review of Accuracy of Numerical Methods Used

Finite difference time domain (FDTD) and finite element method (FEM) are two most widely used numerical methods for plasmonic simulations. We have used commercial FDTD code Lumerical FDTD Solution from Lumerical and FEM code Femlab (now known as Comsol Multiphysics) from Comsol for the designs and analyses presented in this work. The accuracy of both methods for plasmonic simulations is well documented in. To ensure the methods give reliable results for simulating HPWG devices, we simulated one dimensional and two dimensional HPWG devices. Some of the results are presented below.

A.1. One dimensional HPWG

We have computed the effective mode index of the one dimensional HPWG shown in Fig. A.1 using Femlab and compared those with the results obtained from transfer matrix method.

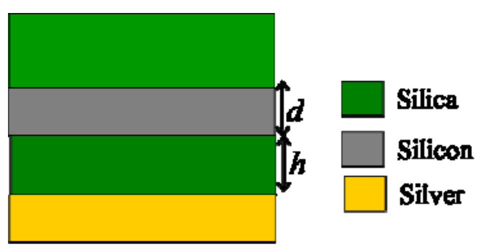

Fig. A.1. One dimensional HPWG

Table A.1. Comparison of effective mode index obtained from various methods

d (nm)	h (nm)	n_{eff} (transfer matrix method)	n_{eff} (FEM)	Δn_{eff} (FEM)
100	100	1.679075	1.67965	0.034
100	150	1.861499	1.860908	0.0317
150	150	1.777072	1.777624	0.031
200	200	1.968261	1.967925	-0.017

A.2. Two dimensional HPWG

We have computed the effective mode index of the one dimensional HPWG shown in Fig. A.2 using both Lumerical FDTD Solutions and Femlab for various choice of waveguide dimensions and summarized the results in Table A.2.

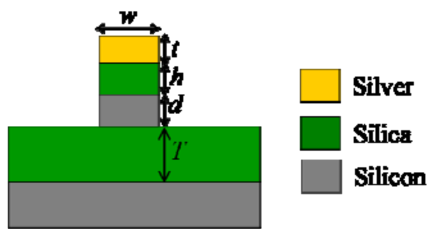

Fig. A.2. Two dimensional HPWG

Table A.2. Comparison of effective mode index obtained from various methods

w **(nm)**	**d (nm)**	**h (nm)**	**n_{eff} (FDTD)**	**n_{eff} (FEM)**	**Δn_{eff} (FDTD)**
340	340	45	2.497526	2.495399	0.085%
300	340	100	2.31161	2.309413	0.095%
400	240	100	2.02155	2.02	0.076%

The agreement observed in all these cases illustrates the reliability of Lumerical and Femlab in modeling HPWG devices.

Appendix C

Optimization of the HPWG Biosensor

We have optimized the structure shown in Fig. B.1. for both TE and TM modes and presented the summary of optimization results in chapter 6. Some more details about the results are presented in this appendix.

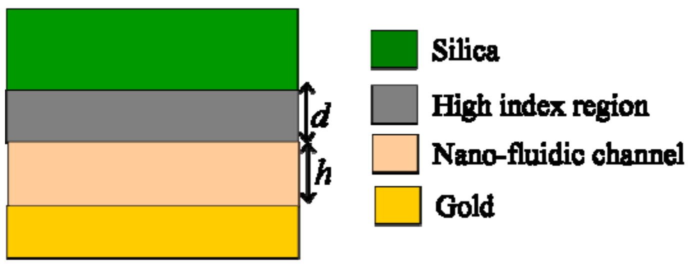

Fig. B.1. One dimensional HPWG sensor

Depending on the thickness of the high index medium and wavelength of operation, HPWG can support a number of TM and TE modes. We have carried out a detailed numerical analysis using transfer matrix method to examine all the modes and find the highest possible combined surface sensitivity factor (G as defined in Chapter 6) achievable. The following notations are used

n_{eff} = Effective index of a mode supported by the HPWG

G^{TM} = Maximum G achieved for a particular high index region thickness

λ_{TM} = Wavelength at which G equal G^{TM} for a particular design

S_{TM} = Surface sensitivity of the TM mode at wavelength λ_{TM}

L_{prop}^{TM} = Propagation distance of the TM mode at wavelength λ_{TM}

$\lambda_{Cut\ Off}$ = Cut off wavelength of a mode for a particular high index region thickness

G^{TE} = Maxium G achievable for the TE polarization for a specific hybrid waveguide design

S_{TE} = Surface sensitivity of the TM mode at wavelength λ_{TE}

L_{prop}^{TE} = Propagation distance of the TE mode at wavelength λ_{TE}

Table B.1 summarize the results for the TM mode for silicon slab.

Table. B.1. Variations of surface sensitivity parameters with silicon thickness for the TM mode

Silicon Thickness (nm)	$\mathbf{n_{eff}}$	$\mathbf{G^{TM}}$ **(nm^{-1})**	λ_{TM} **(μm)**	$\mathbf{S_{TM}}$	$\mathbf{L_{Prop\_Gmax}}$ **(μm)**
100	1.86	0.39	0.92	1.18e-3	27
150	2.2	0.549	1.05	1.11e-3	90
150	1.45	0.36	1.05	1.27e-3	210
200	2.7	0.763	1.1	8.64e-4	390
200	1.45	0.748	1.31	1.22e-3	290
250	2.8	0.924	1.15	4.45e-4	1200
250	1.65	0.364	0.95	1.09e-3	30
250	1.45	0.69	0.87	9.3e-4	500
300	3.3	1.006	1.2	2.03e-4	2800
300	2	0.443	1.0	1.02e-3	60
300	1.451	0.367	1.01	1.25e-3	225
350	3.15	1.027	1.2	1.03e-4	5800
350	2.1	0.562	1.1	9.8e-4	164
350	1.45	0.366	1.15	1.099e-3	300
350	1.4493	0.3	0.812	4.42e-4	103
400	3.25	1.029	1.15	5.9e-5	8950
400	2.3	0.683	1.15	1.8e-4	330
400	1.45	0.37	1.3	1.016e-3	600
400	1.45	0.338	0.92	1.22e-3	180

As an example the variations of surface sensitivity ($\partial n_{eff}/\partial a$), propagation distance and G for the fundamental TE mode for a 100 nm thick silicon nitride film is shown in Fig. B.1.

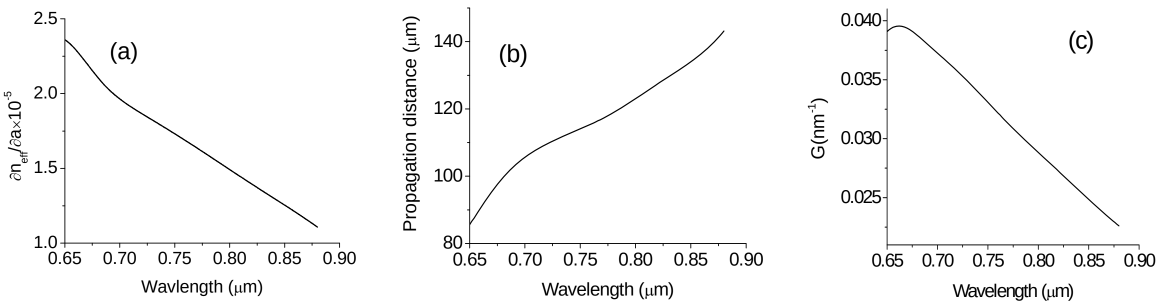

Fig. B.1. Variations of (a) surface sensitivity (b) propagation distance (c) G for a HPWG sensor. The thicknesses of both the nanofluidic channel and silicon nitride are 100 nm.

Plots similar to Fig. B.1 were produced for various silicon thickness and examined to get the values summarized in Table B.1.

Table B.2 summarize the results for the TE mode for silicon slab.

Table B.2. Variations of surface sensitivity parameters with silicon thickness for the TE mode

Silicon Thickness (nm)	**n_{eff}**	**G^{TE} (nm^{-1})**	**λ_{TE} (μm)**	**S_{TE}**	**L_{Prop_Gmax} (μm)**
150	2.85	0.012	1.1	3.5e-6	280
150	1.45	0.007	1.53	8e-6	60
200	3.05	0.0116	1.15	2e-6	500
200	1.45	0.0128	1.05	1.8e-5	70
250	3.2	0.01136	1.15	1.25e-6	800
250	2	0.01245	1.05	9e-6	100
300	3.26	0.01116	1.15	8e-7	1200
300	2.2	0.012	1.1	6e-6	170
300	1.45	0.00538	0.92	1.4e-5	28
350	3.35	0.0111	1.16	4.5e-7	1800
350	2.6	0.0117	1.15	4e-6	290
350	1.45	1.6	0.0125	4e-6	240
350	2.42	0.0089	1.25	5.5e-6	160

Table B.3 summarize the results for the TM mode when the high index slab is silicon nitride instead of silicon.

Table B.3. Variations of surface sensitivity parameters with nitride thickness for the TM mode

Nitride Thickness (nm)	**n_{eff}**	**G^{TM} (nm^{-1})**	**λ_{TM} (μm)**	**S_{TM}**	**L_{Prop_Gmax} (μm)**
150	1.618	0.353	0.85	9.4e-4	25
200	1.66	0.374	0.85	7.65e-4	32.5
250	1.72	0.396	0.85	5.5e-4	47
300	1.77	0.415	0.85	4e-4	66
300	1.449	0.48	0.87	1.4e-4	250
350	1.81	0.431	0.851	2.75e-4	100
350	1.498	0.575	1.0	8e-5	600
400	1.84	0.443	0.85	2e-4	155
400	1.45	0.38	1.11	1e-4	350
450	1.865	0.454	0.85	1.5e-4	220
450	1.45	0.393	1.25	5e-5	700
500	1.88	0.462	0.85	1e-4	300
500	1.45	0.434	1.4	5e-5	1200

Table B.4. Variations of surface sensitivity parameters with nitride thickness for the TE mode.

Nitride Thickness (nm)	**n_{eff}**	**G^{TE} (nm^{-1})**	**λ_{TE} (μm)**	**S_{TE}**	**L_{Prop_Gmax} (μm)**
150	1.693	0.0402	0.66	1.4e-4	160
200	1.775	0.0408	0.66	8.5e-6	260
250	1.82	0.0411	0.65	5.5e-6	400
300	1.85	0.0413	0.65	3.65e-6	580
350	1.89	0.0415	0.65	2.58e-6	830
400	1.9	0.0416	0.65	1.86e-6	1160
400	1.62	0.0398	0.67	10.8e-6	200
450	1.92	0.042	0.65	1.4e-6	1550
450	1.67	0.0402	0.67	7.9e-6	280
500	1.93	0.0418	0.65	1.08e-6	2000
500	1.72	0.0405	0.67	5.9e-6	365

As another example, Fig. B.2. shows the variations of same quantities as a function of wavelength for the fundamental TM mode in case of a 100 nm thick silicon film.

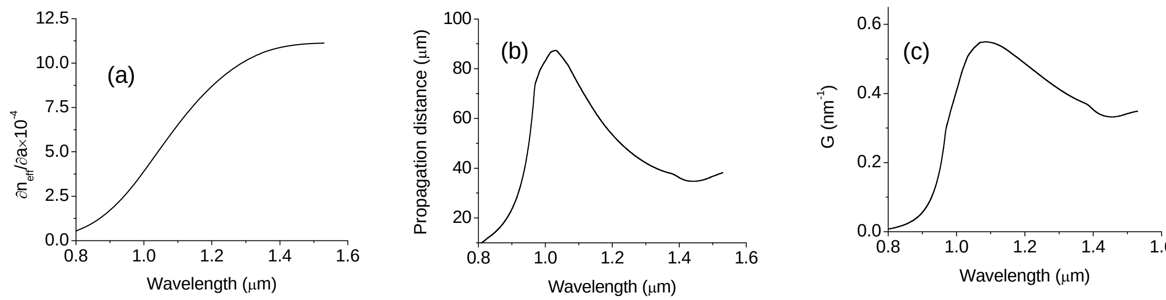

Fig. B.2. Variations of (a) surface sensitivity (b) propagation distance (c) G for a HPWG sensor. The thicknesses of the nanofluidic channel and the thickness of the silicon slab is 100 nm.

Several trends can be observed from the Tables.

a) The highest G and highest surface sensitivity do not always coincide. This confirms our notion (Chapter 6, section 6.4) that surface sensitivity is not a good measure of limit of detection.

b) The HPWG supports two kinds of TM mode: the hybrid TM mode which is concentrated mostly in the nanofluidic channel. In this case the surface sensitivity is relatively large and the propagation loss is moderate, for example the TM mode listed in Table B.1 is a hybrid TM mode. It also supports TM mode which is concentrated mostly in the high index layer and only a small fraction of it is in the nanofluidic channel. In this case the surface sensitivity is rather low but the propagation loss is also very low. As a result, large value of G can also be achieved for these modes. The device length for such case however will be very long. One example is the first TM mode for 250 nm thick silicon film in Table B.1. The device length in this case is more than one mm, as opposed to several tens of microns for the hybrid waveguide modes.

Publications

Journal Contributions

1. M. Z. Alam, F. Bahrami, J. S. Aitchison, and M. Mojahedi, “Hybrid plasmonic waveguide as a platform for biosensing,” Submitted to Optics Express.
2. M. Z. Alam, J. S. Aitchison, and M. Mojahedi, “Theoretical analysis of hybrid plasmonic waveguide,” Submitted to IEEE Journal of Selected Topics in Quantum Electronics.
3. X. Sun, M. Z. Alam, S. J. Wagner, J. S. Aitchison, and M. Mojahedi, “Experimental demonstration of a hybrid plasmonic TE-pass polarizer for silicon-on-insulator platform,” Submitted to Applied Physics Letters.
4. N. J. Casper, M. Z. Alam, and M. Mojahedi, “Compact hybrid plasmonic polarization rotator,” Optics Letters (accepted).
5. F. Bahrami, M. Z. Alam, J. S. Aitchison, and M. Mojahedi, “Dual polarization measurements in the hybrid plasmonic biosensors,” Journal of Plasmonics (accepted).
6. M. Z. Alam, J. S. Aitchison, and M. Mojahedi, “A polarization independent hybrid plasmonic coupler for silicon on insulator platform,” Optics Letters, 37, 3417-3419 (2012).
7. M. Z. Alam, J. S. Aitchison, and M. Mojahedi, "Compact and silicon-on-insulator-compatible hybrid plasmonic TE-pass polarizer," Optics Letters **37**, 55-57 (2012).
8. M. Z. Alam, J. S. Aitchsion, and M. Mojahedi, "Compact hybrid TM-pass polarizer for silicon-on-insulator platform," Applied Optics **50**, 2294-2298 (2011).

9. M. Z. Alam, J. Meier, J. S. Aitchisoon, and M. Mojahedi, "Propagation characteristics of hybrid modes supported by metal-low-high index waveguides and bends," Optics Express, **18**, 12971 – 12979 (2010).

10. M. Z. Alam, J. Meier, J. S. Aitchison, and M. Mojahedi, "Gain assisted surface plasmon polariton in quantum wells structures," Optics Express, **15**, 176-182, (2007).

Conference Contributions

1. J. S. Aitchison, M. Z. Alam, X. Sun, and M. Mojahedi, "Hybrid plasmonic waveguides for on-chip polarization control," Invited paper to be presented in Frontier of Optics (2012).

2. X. Sun, M. Z. Alam, J. S. Aitchison, and M. Mojahedi, "Comparison of confinement and loss of plasmonic waveguides," IEEE Photonics Conference (2012) (accepted).

3. J. N. Casper, M. Z. Alam, J. S. Aitchison, and M. Mojahedi, "Ultra-compact integrated hybrid plasmonic mode evolution polarization rotator," IEEE Photonics Conference (2012) (Accepted).

4. M. Z. Alam, J. S. Aitchison, and M. Mojahedi, "A hybrid plasmonic directional coupler for on-chip optical interconnect," pp. 96-97, IEEE Optical Interconnect Conference (2012).

5. X. Sun, M. Z. Alam, S. J. Wagner, J. S. Aitchison, and M. Mojahedi, "Compact hybrid plasmonic TE-pass Polarizer on SOI," CLEO Paper ID CTu1A.8 (2012).

6. F. Bahrami, M. Z. Alam, J. S. Aitchison, and M. Mojahedi, "A plasmonic affinity biosensor with dual polarization based on hybrid plasmonic platform," CLEO, Paper ID JTh2A.112 (2012).

7. M. Z. Alam, J. S. Aitchison, and M. Mojahedi, “Theoretical analysis of hybrid metal-low-high index waveguide,” IEEE Photonics Conference, pp. 135-136 (2011).

8. M. Z. Alam, J. S. Aitchison, and M. Mojahedi, "Hybrid plasmonic waveguide devices for silicon on insulator platform," in OSA Topical Meeting, Paper ID ITuB4 (2011).

10. M. Z. Alam, J. S. Aitchison, and M. Mojahedi, "Vertical wall affinity sensor with polarization diversity," OSA Topical Meeting, Paper SMB3 (2011).

10. M. Z. Alam, F. Bahrami, J. S. Aitchison, and M. Mojahedi, "A hybrid waveguide sensor for highly sensitive biosensing," CLEO, Paper ID JWA111 (2011).

11. M. Z. Alam, J. S. Aitchison, and M. Mojahedi, “Compact and SOI compatible hybrid TM polarizer,” Photonics North, page 225 (2010).

12. M. Z. Alam, J. S. Aitchison, and M. Mojahedi, “Compact and highly sensitive hybrid waveguide biosensor,” Pacifichem (2010).

13. M. Z. Alam, J. S. Aitchison, and M. Mojahedi, “A polarization independent hybrid coupler for silicon on insulator waveguides,” Frontier in Optics (2010).

14. M. Z. Alam, J. S. Aitchison, and M. Mojahedi, “Compact and SOI compatible hybrid polarizers,” Photon 10, page 108 (2010).

18. M. Z. Alam, J. Meier, J. S. Aitchison, and M. Mojahedi, “Super mode propagation in low index medium,” CLEO/QELS, Paper ID JThD112 (2007).

19. M. Z. Alam, J. Meier, J. S. Aitchison, and M. Mojahedi, “Surface plasmons on a lossy left-handed medium,” APS Proceedings, pp. 765-768 (2006).

20. M. Z. Alam, J. Meier, J. S. Aitchison, M. Mojahedi, “Gain assisted long range surface plasmon using multiple quantum wells,” CLEO/QELS, Paper ID QMI5 (2006).